EPFL

Thèse n° 9029

The architecture of benthic biofilms - Linking hydraulics to spatially structured processes

Présentée le 30 avril 2021

Faculté de l'environnement naturel, architectural et construit
Laboratoire de recherche en biofilms et écosystèmes fluviaux
Programme doctoral en génie civil et environnement

pour l'obtention du grade de Docteur ès Sciences

par

Anna DEPETRIS

Acceptée sur proposition du jury

Prof. A. Meibom, président du jury
Prof. T. I. Battin, Dr H. M. Peter, directeurs de thèse
Prof. H. Horn, rapporteur
Prof. E. Morgenroth, rapporteur
Prof. A.-F. Bitbol, rapporteuse

École polytechnique fédérale de Lausanne

2021

Propose theories which can be criticized. Think about possible decisive falsifying experiments—crucial experiments. But do not give up your theories too easily—not, at any rate, before you have critically examined your criticism.
— Karl Popper

To Kurt Hanselmann, Pietro De Anna and Markus Holzner,
for their inextinguishable patience in answering my questions.

Acknowledgements

The work presented in this dissertation is the product of the joint effort of many contributors. Foremost, I want to thank Tom J. Battin, the director of my PhD thesis, for offering me the opportunity to work in his research team. His supervision allowed me to sharpen my scientific background and expertise, and to gain confidence in my research interests. I am profoundly grateful to Hannes Peter, as this work would not have been possible without his constant guidance and support. I would also like to thank all the other members of my laboratory (past and present), for their unconditional help and for the beautiful social atmosphere they create. Among them, I am especially thankful to Paraskevi Pramateftaki, David Scheidweiler, Tyler Kohler, Nicola Deluigi, Nicolas Escoffier, Stelios Fodelianakis, Massimo Bourquin, and Amin Niayifar for their work and passion, which has been pivotal for the results exposed here. I would like to address my most sincere acknowledgments also to the members of the ENAC Technical Platform (EPFL), and especially to Michel Teuscher, Laurent Morier, and Pierre Loesch. Their commitment and competence permitted most of the work reported in this dissertation. From the same team, I would like to address a special note of thank to Antoine Wiedmer, for his competence and willingness to share it, his patience, and for his friendship. The publications reported in this dissertation are the product of the collaborations with many external experts, who greatly fostered my work and scientific approach. Therefore, I am very grateful to Pietro De Anna and Ankur Deep Bordoloi from University of Lausanne, to Giorgia Tagliavini and Markus Holzner from the ETH Zurich, and to Michael Kühl from the University of Copenhagen. Thanks to my thesis director, I had the privilege to participate in numerous international courses, that deeply marked my scientific enthusiasm and allowed me to meet very inspiring people. Among them, I would especially like to thank Kurt Hanselmann, George O'Toole and Rachel Whitaker. Lastly, I am grateful for the support of my parents and many friends, that accompanied me in the last few years.

Lausanne, February 4, 2021 A. D.

Preface

A preface is not mandatory. It would typically be written by some other person (eg your thesis director).

Lorem ipsum dolor sit amet, consectetuer adipiscing elit. Ut purus elit, vestibulum ut, placerat ac, adipiscing vitae, felis. Curabitur dictum gravida mauris. Nam arcu libero, nonummy eget, consectetuer id, vulputate a, magna. Donec vehicula augue eu neque. Pellentesque habitant morbi tristique senectus et netus et malesuada fames ac turpis egestas. Mauris ut leo. Cras viverra metus rhoncus sem. Nulla et lectus vestibulum urna fringilla ultrices. Phasellus eu tellus sit amet tortor gravida placerat. Integer sapien est, iaculis in, pretium quis, viverra ac, nunc. Praesent eget sem vel leo ultrices bibendum. Aenean faucibus. Morbi dolor nulla, malesuada eu, pulvinar at, mollis ac, nulla. Curabitur auctor semper nulla. Donec varius orci eget risus. Duis nibh mi, congue eu, accumsan eleifend, sagittis quis, diam. Duis eget orci sit amet orci dignissim rutrum.

Nam dui ligula, fringilla a, euismod sodales, sollicitudin vel, wisi. Morbi auctor lorem non justo. Nam lacus libero, pretium at, lobortis vitae, ultricies et, tellus. Donec aliquet, tortor sed accumsan bibendum, erat ligula aliquet magna, vitae ornare odio metus a mi. Morbi ac orci et nisl hendrerit mollis. Suspendisse ut massa. Cras nec ante. Pellentesque a nulla. Cum sociis natoque penatibus et magnis dis parturient montes, nascetur ridiculus mus. Aliquam tincidunt urna. Nulla ullamcorper vestibulum turpis. Pellentesque cursus luctus mauris.

Lausanne, 12 Mars 2011 T. D.

Abstract

Ecosystems often exhibit spatio-temporal patterns that affect their functioning. Biofilms, the most prominent microbial lifestyle, represent an example of the link between spatial structure and function in microbial ecosystems. Biofilms are aggregates of microorganisms embedded in an extracellular matrix, characterized by prominent architectures that link micro- to macro-scale processes. Biofilms composed of hetero- and photo-trophic microorganisms carpet the submerged surfaces of streams, where they regulate water chemistry and influence stream biomass productivity. Hydraulics represents a key abiotic cue in these ecosystems. Fluid motion interacts with biofilm structure to determine local physico-chemical conditions, solute uptake rates, and mechanical robustness. While the interplay between fluid motion and biofilm architectures has been studied under controlled laboratory settings, the applicability of this knowledge to natural benthic biofilms remains poorly explored. The objective of this dissertation is to investigate the meso-scale architectures of phototrophic biofilms grown from complex freshwater communities, under hydraulic conditions that resemble a natural stream. The functional consequences of biofilm architecture at an intermediate level between laboratory experiments and natural conditions are explored, by linking structural, physico-chemical, and biotic patterns. In the first part, I describe the construction of a large laboratory installation for the cultivation and characterization of phototrophic biofilms under a gradient of hydraulic conditions with variable bed shear stress, mean flow velocity, and turbulence intensity. In a second part, benthic phototrophic aggregates are characterized by combining optical coherence tomography, oxygen micro-profiling, amplicon sequencing, and fluid dynamic simulations. This work shows that while several previously characterized patterns emerge also in this *quasi*-natural system, the hydraulic conditions in streams may produce peculiarities that distinguish benthic biofilms from other biofilm settings. More specifically, the chemical conditions within phototrophic biofilms closely follow their structural features. However, high flow velocities and turbulence can influence mass transfer in benthic biofilms to an unprecedented degree. Overall, benthic biofilms architectures and their interactions with local hydraulics produce physico-chemical heterogeneities that affect the large-scale functioning of the community, potentially influencing the ecological role of these aggregates in streams. These complex interactions should be taken into account when scaling up local biofilm processes to their global effects on the stream ecosystem.

Riassunto

Gli ecosistemi mostrano pattern spazio-temporali che condizionano il loro funzionamento. I biofilm, lo stile di vita più importante tra i microorganismi, rappresentano un esempio del legame tra struttura spaziale e funzione negli ecosistemi microbici. I biofilm sono aggregati di microrganismi incorporati in una matrice extracellulare, caratterizzati da architetture che collegano micro- e macro-processi. Biofilm composti da microrganismi etero- e fototrofici tappezzano le superfici bentoniche di torrenti e fiumi, dove regolano la chimica dell'acqua e influenzano la produttività di biomassa del torrente. L'idrodinamica rappresenta una pressione abiotica chiave in questi ecosistemi. Il movimento dei fluidi interagisce con le strutture del biofilm per determinare le condizioni fisico-chimiche locali, il tasso di assorbimento dei soluti e la solidità meccanica. Sebbene l'interazione tra il movimento dei fluidi e le architetture dei biofilm sia stata studiata in ambienti di laboratorio altamente controllati, l'applicabilità di questa conoscenza ai biofilm naturali rimane poco esplorata. L'obiettivo di questa dissertazione è studiare le architetture in mesoscala di biofilm fototrofici cresciuti da comunità di acqua dolce, in condizioni idrodinamiche che assomigliano a un fiume naturale. La tesi esplora le conseguenze funzionali dell'architettura dei biofilm a un livello intermedio tra esperimenti di laboratorio e condizioni naturali, collegando strutture spaziali, condizioni fisico-chimiche e processi biotici. In una prima parte, questo lavoro descrive la costruzione di un'installazione di laboratorio per la coltivazione di biofilm fototrofici in un gradiente idrodinamico, con sforzo di taglio, velocità media del flusso e intensità di turbolenza variabili. In una seconda parte, gli aggregati fototrofici vengono caratterizzati combinando tomografia ottica a coerenza di fase, micro-profilazione dell'ossigeno, sequenziamento e simulazioni fluidodinamiche. Questo lavoro mostra che, mentre vari pattern precedentemente descritti emergono in un sistema quasi naturale, le condizioni idrodinamiche dei fiumi possono produrre peculiarità che distinguono i biofilm bentonici da altri tipi di biofilm. Più specificamente, le condizioni chimiche all'interno dei biofilm fototrofici seguono strettamente le loro caratteristiche strutturali. Tuttavia, velocità di flusso e turbolenze elevate possono influenzare lo scambio di soluti nei biofilm bentonici a un livello non descritto in precedenza. Nel complesso, le architetture bentoniche dei biofilm e le loro interazioni con l'idrodinamica locale producono eterogeneità fisico-chimiche che determinano il funzionamento su larga scala della comunità, potenzialmente influenzando il ruolo ecologico di questi aggregati nei corsi d'acqua. Tuttavia, quando si estendono i processi locali dei biofilm ad i loro effetti globali sui corsi d'acqua, è necessario prendere in considerazione una complessità di interazioni.

Contents

Introduction

The physico-chemical conditions of a habitat are derived foremost from abiotic factors, such as diel cycles, geomorphology, and average temperature. These large-scale influences drive the evolutionary and ecological adaptations of the inhabiting biosphere, shaping patterns in biodiversity, ecosystem productivity, resources acquisition, and ecological interactions. However, this imposed template can be modified to various degrees by its interactions with living organisms. Imposed abiotic variations and biotic effects intertwine in a fine network of reciprocal interactions, resulting in a landscape of heterogeneous physico-chemical conditions, often crossing multiple organizational levels and characterized by conspicuous spatio-temporal patterns [12;237]. The spatio-temporal components of a habitat can have a dramatic influence on the large-scale functioning of the inhabiting biosphere. For instance, spatial segregation can determine the connectivity of a metapopulation, potentially shifting the outcome of epidemics [190]. In another example, the tridimensional architecture of a coral reef determines its properties and effectiveness as a wave-breaker [81], as well as its suitability as a refuge for marine biodiversity [88].

Streams and rivers are not just important links between soils, inland waters, and the oceans, but they are also pivotal players in many global geochemical cycles and reservoirs of tremendous biodiversity [9;43;187;228]. River ecosystems can convert enormous amounts of organic matter into inorganic compounds, thereby contributing to the global dynamics of atmospheric CO_2, while they efficiently transform and transport nutrients, pollutants, and particles suspended in the water column [6;11;15;43;180;194]. Nutrient cycling, organic matter degradation, and particle retention within rivers are mostly attributed to the microbial assemblages that adhere to the streambed, termed benthic biofilms [7;253]. Benthic biofilms are dense and cohesive aggregates composed mostly of unicellular and colonial algae and bacteria that attach to the surface of stones and sediments. Figure 1 reports some examples of benthic communities inhabiting mountain streams and their habitat.

The interplay of biotic and abiotic processes in benthic biofilms generates a conspicuous spatial organization. This modulates the ecological interactions of the microorganisms therein, and drives the emergence of their large-scale impact on the river ecosystem [7;13;127;253].

In streams, a dominant abiotic force is represented by fluid motion [24;152;172]. Hydrodynamics influence all aspects of stream ecology, from channel morphology to disturbance regimes, biodiversity, rates of energy and mass transfer, and patterns in **solute** concentrations [38;69;102;199;253]. The flow regime of a river is largely determined by the catchment geomor-

phology and meteorological conditions [258]. However, at a smaller spatial scale, cobbles and sediments modify the local patterns in flow velocity and flow-induced friction [92;152;247;259]. At an even finer scale, the biofilms that colonize the submerged surfaces further modulate the fine hydraulic conditions of their own habitat [152]. The interplay with the local fluid motion influences many aspects of the biofilm ecosystem, and it is largely attributable to the biofilm tridimensional arrangement. Therefore, the biofilm architecture represents an important link between the hydrological regime and its ecosystem functions.

A large body of knowledge on biofilm functioning is derived from studies in the medical and engineering fields. Indeed, microbial aggregates analogous to stream benthic biofilms develop in many other settings, adhering to surfaces ranging from the human gut to ship culls, and they have major ecological, medical, and technological implications. As a consequence, they have been the subject of extensive research, which often addressed their spatial structure and interactions with fluid flow. In this context, important advances in biofilm research have been possible thanks to the introduction of optical coherence tomography (OCT) as a technique to image the biofilm tri-dimensional structure at a mesoscopic scale [242]. This technology, together with extensive mathematical modeling and fluid dynamics simulations, has been instrumental in characterizing the structure-flow interactions in many biofilm systems [80;238;206;243]. However, these experiments and models typically addressed hydraulic regimes that may poorly reflect conditions in a natural stream. Furthermore, OCT has been seldom applied to investigate the structure-flow interactions in phototrophic biofilms, in which the dynamic light environment can strongly influence the internal spatial organization.

This dissertation aims to expand current knowledge linking fluid flow, biofilm mesoscale structure, and chemical heterogeneity to phototrophic benthic biofilms under conditions relevant for a natural stream. Such information may contribute to establishing a link between micro- and macro-scopic dynamics in streams and rivers. I start by introducing stream ecological processes associated with benthic biofilms, as well as the current knowledge regarding the interplay between mesoscale structure and fluid flow in a variety of biofilm systems and theoretical and experimental settings. An overview of two relevant technologies that were used in this work concludes the introduction. Chapter 1 describes the construction of a laboratory installation for the cultivation of phototrophic benthic biofilms, which permits *in situ* investigation of the architecture of complex microbial communities under hydrodynamic conditions relevant for a small stream. In chapter 2, we used the described laboratory installation to study the morphogenesis of phototrophic biofilms under a gradient of hydraulic conditions, examining some of the links between biofilm structure and function. In chapter 3, we characterized the fine-scale chemical heterogeneity associated with different biofilm structures, flow velocities, light conditions and community types. In this study we highlighted the distinctive patchiness in physico-chemical conditions and biodiversity distribution in a natural phototrophic biofilm, alongside its relevance for the macroscopic metabolic properties of the benthic community. The dissertation closes with a critical summary of the main findings of this Ph.D work.

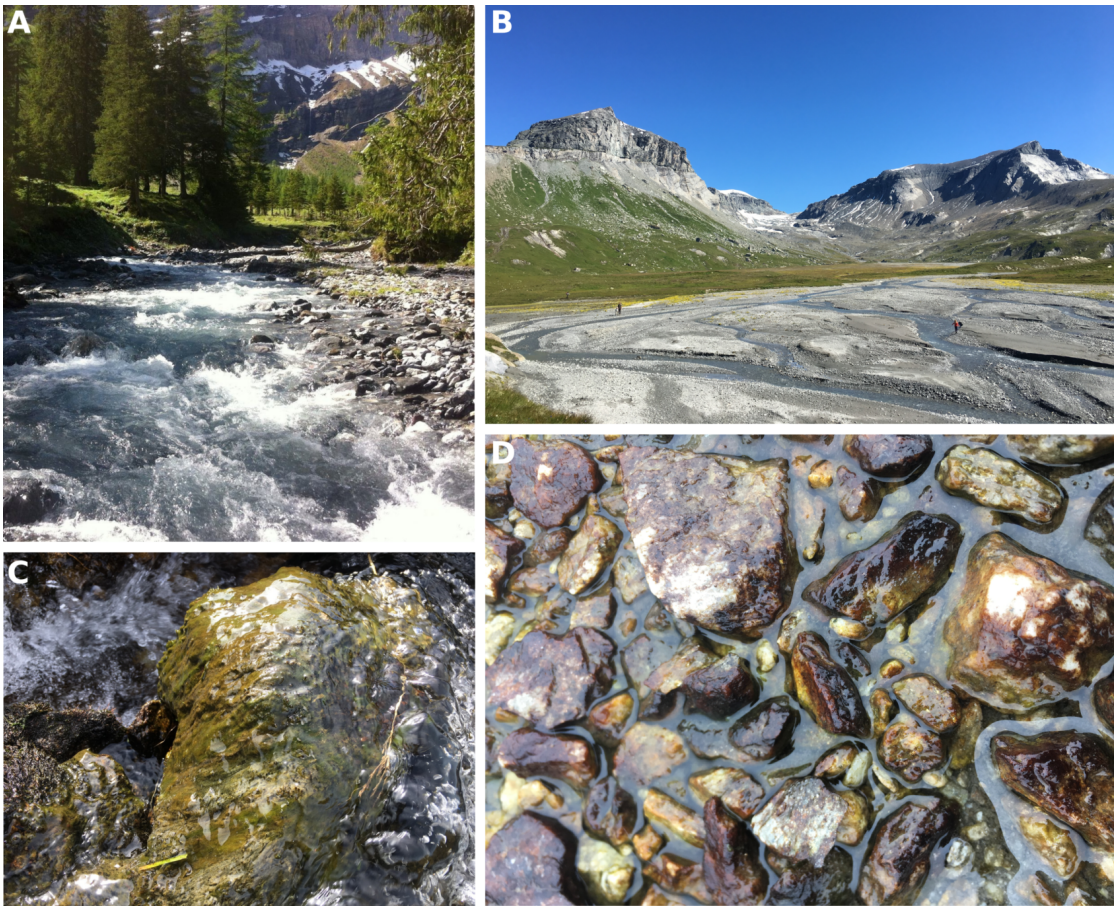

Figure 1 – **Streams and their benthic microorganisms.** Streams and rivers are characterized by a strong environmental pressure given by their hydrological conditions, which present conspicuous spatial and temporal variations. A and B show two mountain streams in the swiss Alps with contrasting hydrological regimes, in Vallon de Nant and Segnas Sut, respectively. The submerged surfaces of streams are colonized by dense microbial communities, termed benthic biofilms, that attach to sediments and stones, and perform fundamental ecological functions. C and D show examples of stream biofilms in the areas of the Aletsch Glacier and Jöriseen, respecitvely.

Benthic biofilms and their role in stream ecosystems

In 1987, Costerton et al. defined biofilms as "matrix-enclosed bacterial populations adherent to each other and/or to surfaces or interfaces. This definition embraces microbial aggregates and floccules and also adherent populations within the pore spaces of porous media" [45]. Since this seminal paper, biofilms have been recognized as a ubiquitous and predominant form of bacterial life, accounting for ~80% of bacterial and archaeal cells on Earth [77]. Cells within a biofilm adhere to each other and to the colonized interface thanks to the secretion of an extracellular matrix (EM), composed of polysaccharides, lipids, proteins and extracellular DNA, which can contribute 50% to 90% of the total biofilm dry mass [75]. Alongside its cohesive role, the EM protects cells from chemical stresses, desiccation and UV radiation, it retains **extracellular enzymes** and absorbs nutrients, metal ions and particles form the surroundings [75;52].

In streams, biofilms carpet submerged surfaces, such as stones and sediments, and perform pivotal ecological functions [7]. They process most of the organic matter, thereby contributing to the high amounts of carbon dioxide emitted by **lotic ecosystems**, and modulating the downstream availability of carbon compounds [11;117;180;197;210]. Further, dissolved and particulate matter is absorbed into the EM or deposited on the biofilm structure, driving changes in the retention of nutrients, pollutants, metal ions and particles along the river network [8;16;194;6;121;2;108;177]. Benthic algae, for instance, were linked to the dampening of a sudden increase in the nitrate dissolved in the water column resulting from a major disturbance event [16]. Further, benthic biofilms are a fundamental food source for higher trophic levels in the stream food-web [84;248]. Benthic **photosynthesis** fixes inorganic carbon dissolved in the water into reduced carbon compounds (such as sugars), providing an important source of **autochthonous** carbon [83;96;191] and imposing characteristic **diel** fluctuations in water chemistry and nutrients availability [239].

Stream biofilms are composed mostly of **photoautotrophic** and **heterotrophic** microorganisms, and usually display a **successional** pattern [7;17;173;204;253]. Bacteria, especially from the Betaproteobacteria clade, are often the initial colonizers [173]. In mature stages, Alphaproteobacteria and Cytophaga-Flavobacteria frequently dominate the prokaryotic community, while other bacterial families found in stream biofilms at lower abundances include Gamma- and Delta-proteobacteria, Actinobacteria, Firmicutes, Gemmatimonadetes, Verrucomicrobia, Planctomycetes and Deinococcus–Thermus [120;140;173]. Filamentous cyanobacteria, diatoms and green algae dominate the phototrophic community [7;10;161;193], while red algae and chrysophytes are common in minor abundance [7;103]. Small green algae are often early members of the developing biofilm, followed by diatoms and colonial algae, whereas filamentous green algae that oscillate in the water flow can be predominant in mature biofilms [10;173;205]. Fungi can degrade large amounts of complex organic matter within benthic biofilms, while archaea are usually found to have minor importance [85;7]. Benthic biofilms are also inhabited by a variety of micro-grazers, such as amoebas, flagellates, ciliates, nematodes, rotifers and dinoflagellates (Figure 3), that can significantly affect biofilm architecture and community composition [29;59;158]. Lastly, viruses are increasingly recognized as important but elusive

components of these ecosystems [111]. The described biodiversity of benthic microorganisms in largely affected by the complex interactions of several environmental factors, such as light availability, pH and temperature of the water, flow conditions, seasonality and nutrient concentrations [73;127;130;196].

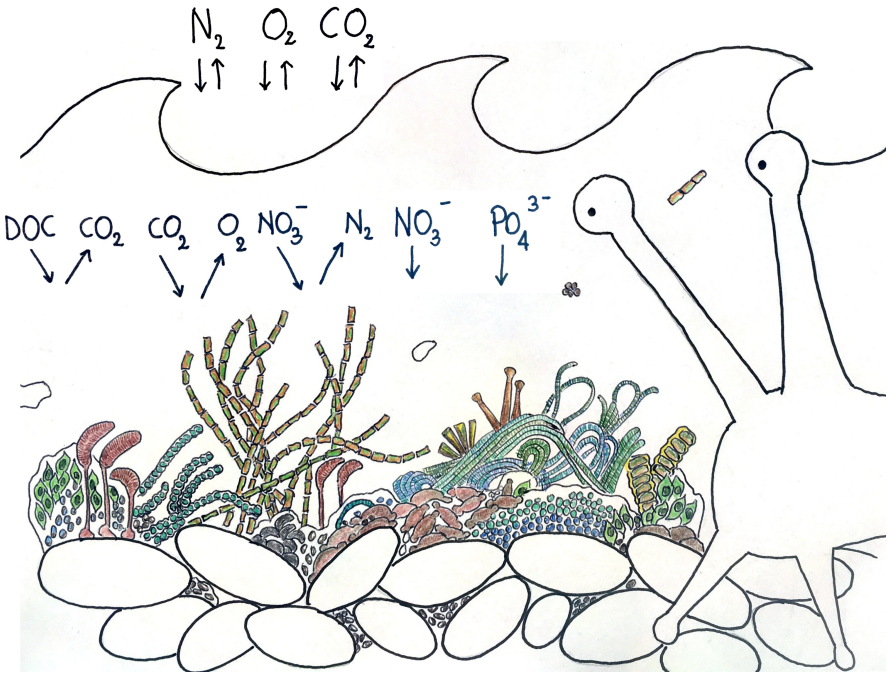

Figure 2 – **Nutrient cycling within stream benthic biofilms.** Dense microbial communities carpet the bed of streams and rivers, adhering on cobbles and sediments. They harbor a dramatic biodiversity of phototrophic and heterotrophic microorganisms, as well as eukaryotic grazers and viruses. They degrade large amounts of dissolved organic carbon (DOC), contributing to CO_2 outgassing from streams and rivers. They also fix CO_2 dissolved in the water by photosynthesis, producing autochthonous carbon and O_2, and they take up nutrients from the water column, such as nitrogen and phosphorus.

Spatial heterogeneity within benthic biofilms and its ecological relevance

Biofilms are distinguished by their prominent chemical heterogeneity [216]. The dense packing of cells and EM components within a biofilm limits the diffusion of solutes that are consumed or produced by the cells. This invariably results in the formation of stable spatial gradients in growth substrates, waste products, and signaling molecules [58;214;216]. Oxygen represents a well-characterized example of this phenomenon, both because of its key role as an **electron acceptor** in **aerobic respiration**, as well as because of the availability of accurate tools for the measurement of its concentration within biofilms [186]. In aerobic microbial aggregates, the oxygen penetrating from the biofilm surface is often consumed within the top layers, and becomes depleted deeper in the biofilm (Figure 4) [76]. Oxygen-depleted zones can limit the growth of obligate aerobes, while they can favor the **anaerobic** consumption of nitrate or the

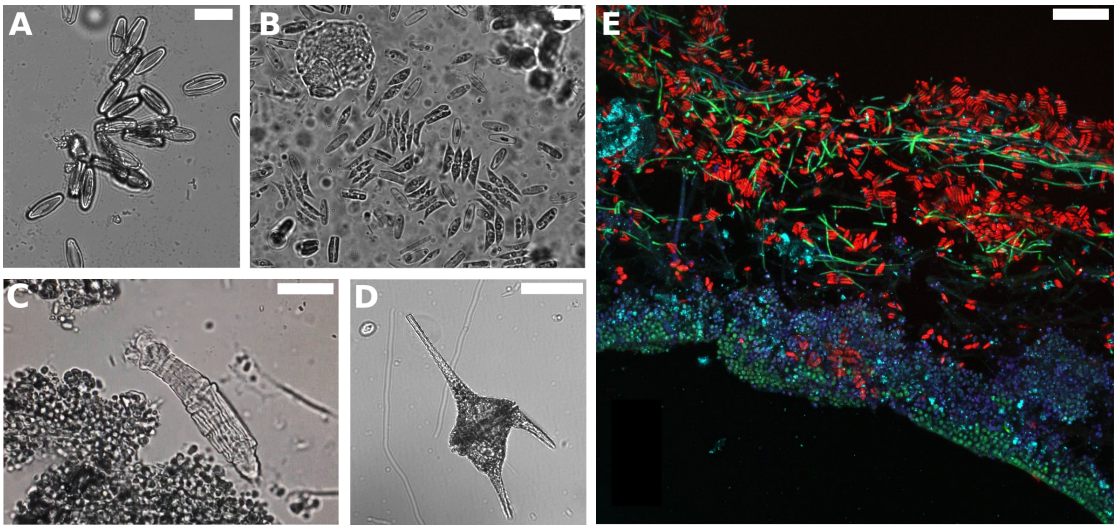

Figure 3 – **Diversity of stream benthic microorganisms.** A small selection of freshwater benthic microorganisms is reported. A shows a group of pennate diatoms, B a micrograph of an environmental sample with abundant pennate diatoms mixed with a green algae of the genus *Scenedesmus*, known for forming groups of four cells when under stress. Scale-bars: 10 μm. C shows a rotifer grazing on a green algae aggregate, while D shows a freshwater dinoflagellate from the genus *Ceratium*. E reports a **confocal laser scanning micrograph** of a thin section of a freshwater benthic biofilm (~50 μm thick). Different combinations of excitation and emission wavelengths were used to distinguish contrasting fluorescent pigments that characterize different microbial groups. In red is chlorophyll a fluorescence (excitation wavelength 665 nm, emission between 670 nm - 720 nm), in green is phycocyanin, a typical pigment expressed by cyanobacteria (ex: 621 nm, em: 626 nm - 645 nm), in blue is possibly phycoerithrin, another common microbial photosynthetic pigment, mixed with chlorophyll a autofluorescence (ex: 565 nm, em: 571 nm - 704 nm), in cyan is the reflected light (at 405 nm). The red microorganisms are a mixture of small pennate diatoms and a green algae of the genus *Scenedesmus*. The green filaments and the cocci forming the base of the biofilm are probably cyanobacteria. Scale bars in C, D, E : 50 μm.

survival of obligate anaerobes [2;137;163]. Other solutes often follow similar spatial patterns, and can, for instance, induce starvation and dormancy in cells within nutrients-depleted zones [44]. Light availability represents another crucial example of the spatial, and temporal, heterogeneity in benthic aggregates. Irradiance attenuates as it penetrates within the biofilm, generating vertical gradients in light availability and quality that vary with biofilm optical properties (Figure 4) [123]. The abundance of phototrophs, their photosynthetic rate and the production of photosynthetic pigments closely follow these gradients [123;124;179]. Hence, the interaction between cell metabolism and physical processes generates a highly heterogeneous chemical environment, characterized by multiple juxtaposed micro-niches.

The composition and physiology of the inhabiting microorganisms often closely follow the described physico-chemical patterns, resulting in tight ecological interactions [12;202;241]. For instance, the close spatial proximity of photo- and hetero-trophs within benthic biofilms allows for numerous metabolic interactions that can contribute to the overall metabolic fingerprint of a river [15;138;211]. Phototrophs inhabiting the photic layers of biofilms secrete organic carbon and oxygen that sustain a flourishing community of associated heterotrophs [96;113;124]. Het-

erotrophic respiration, in turn, releases CO_2 that can fulfill the inorganic carbon requirement of the phototrophs, producing a tight coupling between photosynthesis and respiration [124]. During the night, in contrast, both phototrophs and heterotrophs respire oxygen, which in turn can become strongly depleted (Figure 4) [70]. The metabolism of phototrophic microorganisms also drives local cycling of phosphate [71], modulates pH and redox conditions, favoring the activity of bacterial extracellular enzymes and indirectly enhancing numerous heterotrophic pathways [71;188]. The EM matrix components secreted by benthic algae can also be utilized as a carbon source by heterotrophic bacteria, which have been observed to stimulate EPS production, algae biomass production and aggregation in a benthic community composed of diatoms and bacteria [34]. To conclude, the fine-scale physico-chemical heterogeneity in benthic biofilms supports a network of tight ecological interactions that drives important ecological process, such as their nutrients uptake rate and productivity.

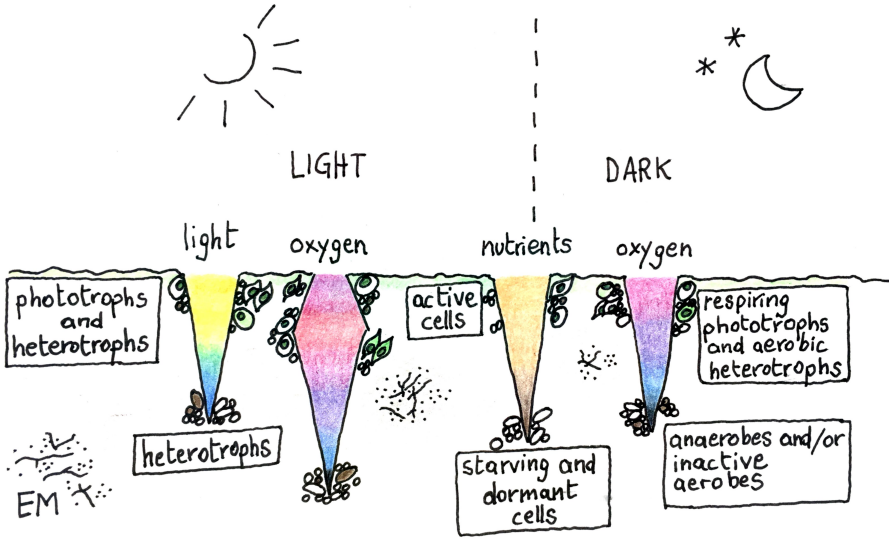

Figure 4 – **The physico-chemical gradients within biofilms.** The dense packing of cells and extracellular matrix (EM) components limits the penetration of light and solutes below the surface of phototrophic biofilms. As a consequence, as the microorganisms that live therein consume or produce oxygen and nutrients by photosynthesis and respiration, the biofilm becomes a highly heterogeneous habitat, characterized by complex physico-chemical gradients that can alter the biodiversity and physiological state of their inhabitants. Figure adapted from [76].

Hydraulic conditions and the biofilm mesoscale architecture

The **hydrological regime** determines stream-bed stability, near-bed **hydraulics**, water residence time, nutrient dynamics, and solute retention within a river network [24;174;212;69;127;152]. Strong flow can displace sediments and cobbles, damaging benthic phototrophic communities, and shifting river metabolism towards heterotrophy [4]. Bed **shear stress** imposes a strong selective pressure on benthic biodiversity and influences succession dynamics [20;19;90;160;171]. Further, flow velocity influences the patchiness and diversity of benthic communities at the

meter scale, perhaps by modulating their dispersal [23;159]. Hydraulic conditions determine the distribution of grazers and their efficiency in algae removal, as well as the rate of propagule attachment and colonization of bare surfaces [104;118;20]. Once the biofilm has established, it can be scoured and eroded by hydraulic drag, decreasing its biomass and triggering the release of propagules into the water column [23;127]. On the other hand, flow can affect the growth and metabolism of benthic biofilms by enhancing solute transfer [23;24;105;128]. For instance, flow increases the penetration of oxygen within benthic biofilms, thereby inhibiting **denitrification** and influencing bulk nitrate removal [2]. Biomass, photosynthesis, respiration, and the uptake rate of dissolved organic matter can increase in biofilms cultivated at higher flow velocities [105;10]. Under strong shear, biofilms may modulate the amount and composition of the EM, which can affect their mechanical robustness, but also their growth rate [10;90;244]. Accordingly, it has often been observed that biofilms developing under harsh hydraulic conditions adhere more strongly to the colonized surface [218]. Hence, while current velocity tends to erode biofilms, it also enhances their growth and attachment. This results in the often complex and non-linear correlation between benthic biomass and hydraulic cues [24;105;107].
The effect of hydraulic conditions on biofilms is mediated by the continuous feedback between the local flow patterns and the biofilm's tridimensional architecture. This has been a prominent research topic in environmental, engineering and medical biofilms in a variety of experimental settings. Biofilms are distinguished by wide range of spatial features: mushroom-like caps [62], ripples [225], clumps separated by voids [50;221], cones [164],and wrinkles [58]have all been described in different types of biofilms (Figure 5). Further, they can present an intricate internal structure with voids and channels, as well as different degrees in porosity (Figure 5) [80;243;251]. Biofilm porosity is the ratio between void volume and the total biofilm volume, and it can be calculated with two different approaches [242]. The "global" porosity of the biofilm takes into account the voids above the biofilm-liquid interface, as used for instance in [167;243]. The "internal" biofilm porosity takes into account only the voids present below the biofilm-liquid interface [57]. The "global" definition of porosity was used in the chapter 2 of this dissertation, while "internal" porosity was calculated in chapter 3. The biofilm architecture emerges from the interplay between endogenous and exogenous processes. Growth, EM production, localized cell-death, competition and redox state [58;3;75;76], but also substrate supply, grazing pressure and hydrodynamic conditions [29;80;222] can play a role in biofilm morphogenesis.
Among benthic communities, a fast and turbulent flow regime triggers the development of long structures that flap and oscillate into the flow efficiently taking up solutes and propagules, known as streamers [20;230]. Under slow flow velocities, benthic biofilm can shape into a thicker, rougher and more porous structure when compared to the fast-flow counterpart. This architectural response affects the rate of particle filtration and accumulation on the biofilm, as well as the transient storage of solutes [10]. In micro-fluidic chambers, hydraulic drag can induce the formation of ripples that migrate downstream [42;225]. An increased flow velocity can induce compaction of the internal biofilm structure developing on a filtration membrane [61]. In both microfluidic devices and tube bioreactors, shear stress can induce the dynamic detachment and deformation of biofilm clusters [27;60;65;224], while a more homogeneous structure can

account for self-shielding against hydraulic drag and sloughing [168;206;245]. These examples demonstrate how hydraulic pressure can directly and indirectly alter biofilm architecture. Reciprocally, the structural features of submerged biofilms can modify local flow patterns, with consequences for mass transport, mechanical robustness, biodiversity, productivity and dispersal [50;18;27;68;139;221;244]. In this context, the tridimensional architecture represents a collective property of the aggregate that allows the biogenic construction of the local habitat, linking micro- and macro-scale biofilm processes [8;12;9;145]. Experiments conducted under highly controlled hydraulic conditions and extensive mathematical modeling have greatly contributed to our understanding of the interplay between flow and biofilm structure. Flow-cells (with a height up to 2 mm) allow precise control of flow conditions, while numerical simulations effectively demonstrate small-scale flow patterns, and electrochemical microsensors characterize local solute transfer. More recently, these results have been expanded to characterize biofilms in broader experimental settings, such as filtration membranes [80]. The following paragraphs report some relevant literature about the physical transfer of momentum and solutes between water and biofilms, as well as a brief theoretical background. Despite the variety of biofilm communities, experimental procedures and theorized conditions, these results refer to widespread dynamics in submerged biofilms, therefore relevant for understanding benthic microorganisms and their relationship with the abiotic environment.

Momentum and mass transport, and the biofilm architecture

Momentum transport

Fluid flow is an influential and exquisitely scale-dependent cue for biofilms and microorganisms in general. At the scale of a single cell (*e.g.*, scale of a few micrometers), **viscous forces** dominate fluid motion. At the reach of streams or ocean waves, viscosity is mostly irrelevant and fluid dynamics is dictated by **inertia** [152;162;176;24]. The Reynolds number represents a broad characterization of fluid motion, and is defined as the ratio between inertial and viscous forces.

$$Re = \frac{\rho\,[g\,m^{-3}] \times v\,[m\,s^{-1}] \times L\,[m]}{\mu\,[g\,m^{-1}s^{-1}]}$$

where ρ is the fluid density, v is the flow velocity, L the characteristic length scale and μ the dynamic viscosity of the fluid. At low Reynolds number, *i.e.*, at small flow velocities and spatial scales, fluids behave as parallel layers slipping smoothly on each other, a phenominon referred to as "laminar" flow. At higher flow velocities and larger scales, the shear stress between adjacent layers increases, causing turbulent eddies and spatio-temporal irregularity. Such a flow regime is referred to as "turbulent", while conditions with intermediate Reynolds number are indicated as "transitional". In contrast with a laminar regime, turbulent flow is characterized by a fast dissipation of the internal fluid energy, high diffusivity and tridimensional vorticity, enhancing solute mixing, momentum, and heat transfer [232]. Another defining characteristic of turbulence is the nestedness of spatial scales, a concept know as energy/eddies cascade [114;122]. According to this concept, turbulence is generated at large spatial scales as a

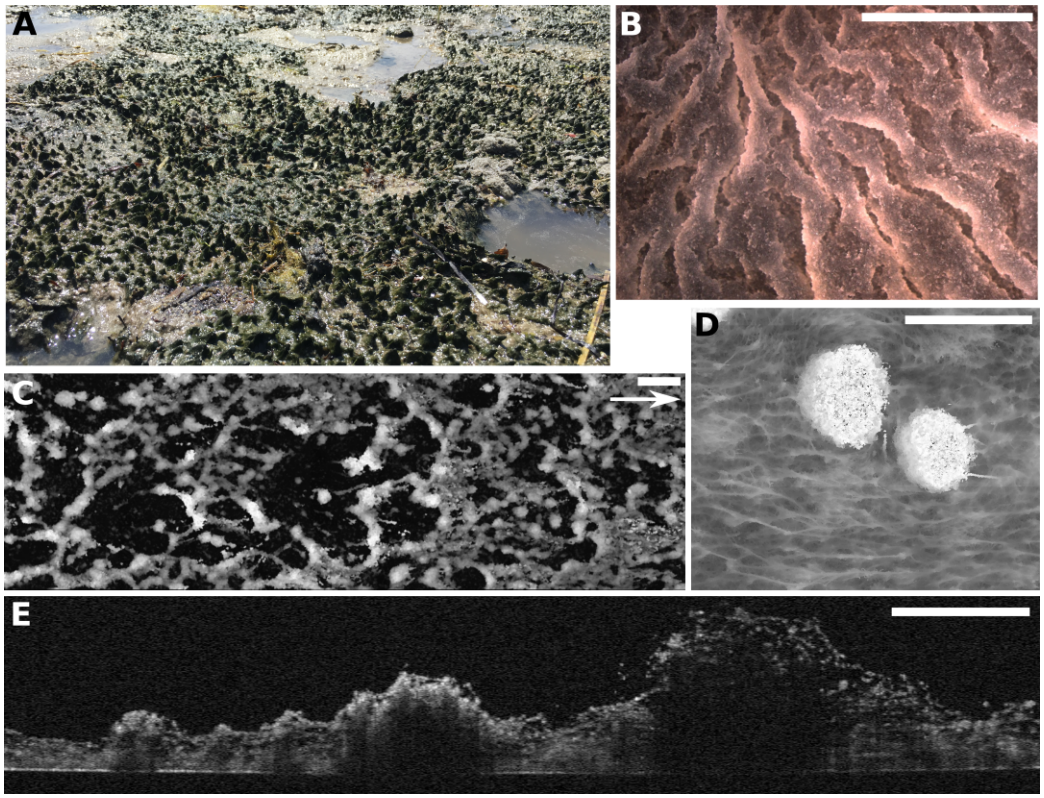

Figure 5 – **Biofilm mesoscale architectures.** A shows a photograph of the cones formed by a cyanobacteria mat in the intertidal area of Little Sippewisset Marsh (MA, USA). Cones have a typical height of ~10 mm. B is a stereophotograph of the rippled morphology of a *Bacillus subtilis* floating biofilm (or pellicle). C shows the ripples, probably formed as a consequence of hydraulic drag force, in a phototrophic biofilm imaged in this dissertation by OCT. The arrow indicates the direction of the flow. D presents the ripples and tufts formed by cyanobacteria and green filamentous algae, respectively, imaged by OCT in this dissertation. Scale bars in B; C; D: 5 mm. E is an OCT scan that highlight differences in internal porosity in a phototrophic biofilm community investigated in this dissertation. On the left of the scan, a compact cyanobacteria mat. On the right is a loose and porous aggregate of green filamentous algae. Scale bar : 1 mm.

consequence of the energy transfer from the mean flow to eddies of size comparable to the external scale (*e.g.*, the depth of the stream). These largest eddies are unstable and transfer their energy to progressively smaller eddies, up to the so-called dissipative scale. This is the dimension of the smallest eddies, which then dissipate into heat. A rigorous mathematical description of turbulence is often impractical, hence turbulent flows are treated by focusing on their statistical properties. For instance, the transfer of momentum and mass in turbulent flows are often modeled by introducing the eddy diffusivity of momentum (and of a scalar) that allows the study of energy transfer and mass fluxes without considering the fine structure of the turbulent eddies.
Biofilms occupy an intermediate position between spatial scales, and they are distinguished by complex interactions between viscosity and inertia [162]. Above the surface of many biofilms immersed in a liquid, turbulence dominates fluid motion [224]. When approaching the biofilm, however, the interaction between the solid surface and the fluid causes a decrease in flow velocity, the dissipation of turbulence and an increased influence of viscosity. The layer of fluid above the biofilm in which liquid motion is affected by the presence of the solid surface is termed the momentum boundary layer (BL). When approximating the biofilm as a solid surface with a **no-slip boundary**, the velocity of the flow becomes zero at the biofilm liquid interphase. The shape of the BL depends on the viscosity of the fluid as well as the characteristics of the surrounding flow. In laminar conditions, the velocity changes smoothly with the distance from the solid and can be predicted using the simplified Navier-Stokes equation. Turbulent boundary layers present a more complex shape, typically subdivided into two zones (Figure 6) [126]:

- a viscous or laminar sublayer, a thin layer closest to the solid surface where flow velocity is very low and the flow is laminar
- a logarithmic layer, farther away from the surface, in which flow velocity changes logarithmically with depth, forming a steep gradient that sustains turbulence.

The spatial variation in flow velocity within a boundary layer imposes a shear stress on the biofilm surface, which can be estimated as

$$\tau\,[Pa] = \frac{dv}{dz}\,[s^{-1}] \times \mu\,[g\,m^{-1}s^{-1}]$$

where dv/dz is the local gradient in velocity and μ is the water dynamic viscosity. The momentum that a biofilm structure has to resist in order to remain attached is termed "drag force", and depends on the biofilm shape as well as the bed shear stress. When the drag force exceed the adhesive strength, particles with a wide size range can detach from the biofilm thereby shaping its architecture [226;221]. While partial erosion of the protruding structures can lead to a smooth biofilm architecture [41], isolated clumps are more susceptible to major sloughing events of the entire biofilm structure [1;64;65;206]. Reciprocally, irregularities of the biofilm surface shape the momentum BL and local flow patterns (Figure 6). Roughness elements and troughs in the biofilm topology can induce the formation of vortices, wakes and stagnant zones, that

affect the fluid energy dissipation and local shear stress and drag [1;80;168;206]. Thereby, isolated clusters are more susceptible to flow-induced detachment compared to smoother and self-shielding architectures [229;245]. In addition, the biofilm rheological properties, such as viscoelasticity can strongly influence the biofilm mechanical robustness [1;27].
In comparison to the fluid motion surrounding biofilm structures, fluid within them remains more elusive. De Beer and colleagues [49] observed that plumes of fluorescein injected within a biofilm were not affected by the surrounding flow, concluding that fluid flow within the biofilm was negligible. This notion is supported by experimental studies showing that biofilm can be almost impermeable to fluid flow (with permeabilities ranging from 10^{-17} m^2 to 10^{-15} m^2) [141;215]. However, the effect of internal flow may be relevant under certain conditions [53;80;95;48]. An example of global relevance is the flow across biofilms that foul filtration membranes, increasing the hydraulic resistance of the device and causing major economical costs world-wide [56;80]. Biofilm permeability is influenced by the internal structure, the presence of pores and the material properties of the EPS fraction [25;56;61]. To model fluid flow inside microbial aggregates, the biofilm is commonly considered as a porous medium in which flow is laminar and confined within the limited pore space between cells and EM components [53;116] (Figure 6). Hence, flow within biofilms can be described according to Darcy's law:

$$q\,[m\,s^{-1}] = -\frac{k\,[m^2]}{\mu\,[Pa\,s]} \times \nabla P\,[Pa\,m^{-1}]$$

where q is the instantaneous flux (or discharge per unit area), k denotes hydraulic permeability, μ is fluid dynamic viscosity, and ∇P is the pressure drop.

External and internal mass transport

As mentioned earlier, chemical heterogeneity represents a distinctive characteristic of the biofilm lifestyle. It emerges from the interplay between cell metabolism and the physical process of solute transport. The transfer of solutes in space can occur via two mechanisms. Flow can transport solutes by advection, while isotropic Brownian motion transfers them by diffusion. Diffusion is much less efficient than advection and often represents the limiting step in the replenishment of solutes within biofilms [214]. The convection-diffusion equation for a steady state describes the local concentration of a solute, as:

$$\nabla^2 c\,[mol\,m^{-3}] \times D\,[m^2\,s^{-1}] - \nabla c\,[mol\,m^{-3}] \times v\,[m\,s^{-1}] + R\,[mol\,m^{-3}\,s^{-1}] = 0$$

this indicates that the local solute concentration depends on

- a diffusive term, expressed by the local curvature of the concentration gradient times the diffusion coefficient D, which depends on the solute, fluid and temperature.
- an advective term, expressed as the concentration gradient times the flow velocity v
- a reaction term R that expresses the rate of solute consumption or production in a

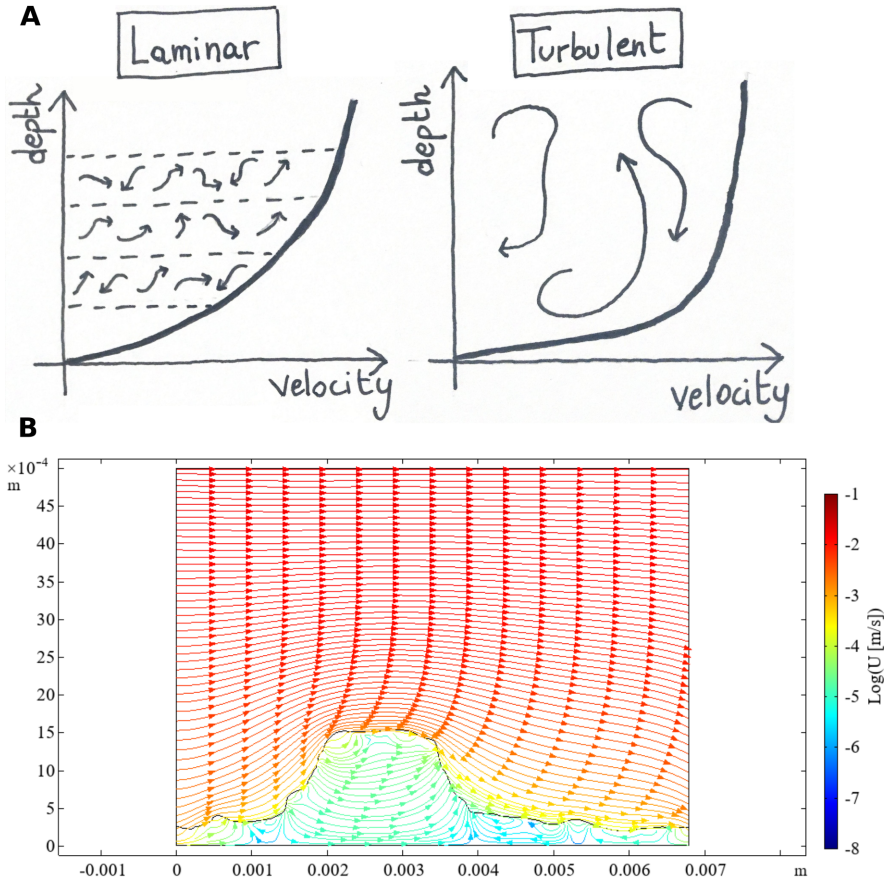

Figure 6 – **Momentum transport around and within biofilms.** A depicts typical profiles of flow velocity in the laminar and turbulent boundary layers, with arrows showing representative flow lines. B shows a numerical simulation of the flow stream-lines surrounding a porous biofilm cluster. The presence of the biofilm bends the stream-lines in the water domain, while a weaker flow velocity traverses the biofilm.This simulation was used in this dissertation to study the interaction between structure and flow in phototrophic biofilms.

volume unit.

In the presence of fluid flow, mass transfer is typically governed by advection. As inertial forces decrease, for instance when approaching the biofilm surface or within the biofilm itself, diffusion becomes more important. Within the momentum BL surrounding the biofilm surface, a thinner layer is defined as diffusion boundary layer (DBL), in which solutes transport is governed mostly by molecular diffusion. The upper boundary of the DBL corresponds to a transition point between the bulk liquid, in which solute concentration is uniform, to a layer of the fluid in which the concentration of solutes that are produced or consumed by the biofilm vary with the distance from its surface (Figure 7). The thickness of the DBL is the distance that solutes travel by diffusion, and hence it represents a measure of the external mass transfer resistance imposed by the fluid on the exchange of solutes across the biofilm surface [214]. The DBL directly depends on the shape of the momentum boundary. When flow velocity is low, a thick and flat DBL surrounds the biofilm surface, increasing the mass transfer limitation within biofilm depressions compared to protruding peaks and mounds (Figure 7) [50]. Under these conditions, protruding structures have better access to nutrients compared to the biofilm troughs. Consequently, initial random heterogeneities in the biofilm surface can be progressively amplified, leading to a rough and finger-like biofilm architecture [167]. If the mean flow velocity is sufficient, fluid flows within the biofilm troughs and shrinks the DBL therein. This allows for the formation of horizontal chemical gradients that can supply nutrients to the biofilm base and the sides of the clusters (Figure 7), effectively increasing the total surface area available for solute exchange [50]. In addition, a further increase in flow velocity can cause the formation of vortices in the troughs of the biofilm surface, which can strongly enhance solute transport therein [80;168].

Inside biofilms, advective terms are often negligible and solute transfer is limited by diffusion [128;214]. The rate at which solutes diffuse within a biofilm is expressed by their effective diffusion coefficient (D_{eff}), which represents a measure of the internal mass transfer resistance [214]. D_{eff} is usually expressed as a function of the diffusion coefficient of the same chemical species in water (D_{aq}), and it was experimentally estimated for some important solutes in selected biofilm systems. Within a photosynthetic biofilms, the effective diffusivity of oxygen decreased (respect to water) 0.51 or 0.7 fold [124;181], while this estimate ranged from 0.39 to 1 in heterotrophic biofilms [106;214]. D_{eff} depends on the biofilm porosity, density, and chemical properties, and it may vary spatially within the biofilm [95;106;214;22]. Further, within permeable biofilms characterized by voids and channels, advective terms may become relevant and increase the apparent D_{eff} [53;95;165;251].

Internal mass transfer resistance is a powerful driver of biofilms architecture. Porous and low-density biofilms often develop under slow flow velocities, which results in a higher diffusivity and enhanced mass transfer [22]. Nutrient limitation within biofilms can cause cell starvation and the degradation of the biofilm EM, which can lead to sloughing events and a clumped biofilm architecture [41;110].

To conclude, diffusion and advection determine the chemical landscape around and within biofilms, with important consequences for biofilms morphogenesis [41;168;214;215].

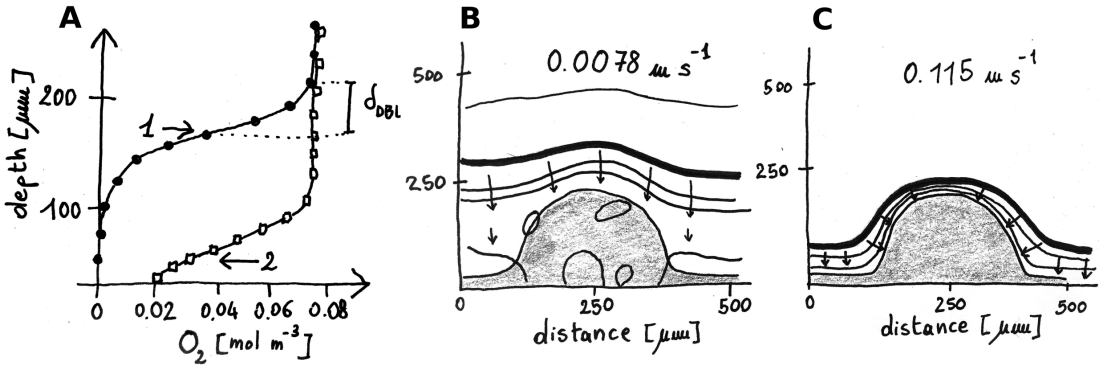

Figure 7 – **Effect of biofilm structure and flow velocity on the diffusive boundary layer (DBL).** In A are reproduced oxygen concentration profiles within a biofilm cluster (filled circles) and in a biofilm void (open squares) at mean flow velocity of 0.064 m s^{-1}. The surface of the cluster is indicated by the arrow (1), and the thickness of the DBL above the cluster is also depicted (δ_{DBL}). Arrow (2) indicates the thickness of the base film. In B and C are shown oxygen concentration contours around a biofilm cluster, measured at mean flow velocity of 0.0078 m s^{-1} and 0.115 m s^{-1}, respectively. The biofilm cluster and base film are shown in shading. The thin lines represent the oxygen contours, the thick solid line indicates the upper limit of the DBL. The arrows show the direction of the largest oxygen gradients. Figure reproduced from [50].

Relevant methods in biofilm research

Optical coherence tomography

Morgenroth and Milfersted [145] have highlighted the importance of mesoscale biofilm structures as a link between micro- and macro-scopic processes, such as nutrient removal. Optical coherence tomography (OCT) is an emerging technology in biofilm research to characterize the mesoscale architecture of biofilms [242]. It is an interferometric technique originally developed for medical imaging that provides a stack of cross sections of the sample reflective properties [109]. A low coherence light beam is split between a reference arm of known length and the imaging arm where the sample is placed. The light reflected from both arms is collected and their **interference** fringe is digitally recorded and processed. An axial profile of the intensity of the backscattered light is obtained, which is encoded in an image as pixel's gray-scale level (Figure 3.4). This profile, named an "A scan", shows the position the sample surface as well as structures below the surface in which a variation in density causes reflectance of the incident light. Several A scans are recorded along a cross-section, named a "B scan" (Figure 3.4), while multiple B scans along the third direction compose the final volumetric scan of the sample (Figure 3.4). To maximize imaging speed, the scanning occurs by changing the direction of the imaging beam rather than the position of its source. This result in longer light paths at the edges of the stack and a spherical aberration that is corrected after image acquisition.

The low-coherence light beam is centered around near-infrared wavelengths (900 nm or 930 nm), which allows for deeper penetration in the sample, while the beam's coherent length together with the medium's refractive index determines the axial imaging resolution (typical

axial resolution is 2.18 μm in water and 3 μm in air). OCT permits an imaging field of few squared centimeters, with a penetration depth of up to 3 mm, a lateral resolution between 1 μm and 15 μm. Furthermore, it does not require any sample treatment, and can be used to image a sample *in situ* and non-invasively [97;242]. Therefore, OCT is an attractive tool for biofilm research. It was deployed to observe biofilms within filtration systems (*e.g.*, [62])and glass capillaries [256] to characterize the fine scale topology of biofilm surfaces, and to estimate biofilm thickness, surface area, and roughness coefficient(s) (*e.g.*, [112;206;243]). OCT scans have been used to inform fluid dynamics simulations and analyse particle deposition and detachment around the biofilm asperities [134;166;206]. Especially attractive is the opportunity provided by OCT to image the biofilm internal structure and variations in porosity [243;80]. The fast imaging speed of OCT also permits the study of the dynamic biofilm deformation as a consequence of a changing hydrodynamic pressure. Biofilm compaction and de-compaction have been related to biofilm hydraulic resistance and performance loss in membrane filtration systems [56;62;112]. Further, "real-time" deformation recordings can be used to investigate biofilm rheological properties [27].
Overall, OCT provides a useful mesoscopic tool to study biofilm structure as an emerging property connecting local and global phenomena within biofilms, and holds great potential for both ecological and engineering advances [242]. The main limitations of this technique relate to *i*) the absence of information regarding the composition of the biofilm components, such as the extracellular matrix and cells , and ii) the limited penetration of the light beam into dense samples, iii) the drop-off in signal-to-noise ratio along an A scan. The effect of a decreased signal-to-noise ratio is visible, for instance, in Figure 3.4.

Electrochemical microsensors

Electrochemical microsensors are devices that allow for the characterization of the fine-scale chemical environment within microbial communities and sediments. Since their introduction in 1980 [184], they have been extensively used to study a variety of microbial mats and sediment types, from hypersaline mats [93] to hot springs [185], deep-sea sediments [153] and phototrophic biofilms [124]. Further, they have been utilized to measure chemical gradients within metazoans, such as corals and termites [125;201]. Microsensors are available for several ecologically relevant solutes, from H_2S to pH, N_2O, H_2 and O_2 [182]. The O_2 sensors have the overall best performance and are especially interesting for the analysis of aerobic respiration and photosynthetic activity [182]. The most common oxygen sensor is an amperometric sensor of the Clark-design [86], with a detection limit of < 1μM to 3 μM, and a 90% response time of down to 0.3 s. The measurement spatial resolution corresponds to the tip of the sensor, which is typically between 10 μm and 50 μm. The sensor is usually mounted on a motorized micro-manipulator that allows to obtain vertical profiles of oxygen concentration above and within the sample, in user-defined z-steps (usually between 50 μm and 500 μm). Clark-type microsensors (Figure 9) are fine glass needles containing an alkaline electrolyte solution of KCl. A gold-coated platinum cathode is placed in close proximity with the sensor tip, connected to a Ag/AgCl reference anode and polarized to ~-0.8 V. The oxygen diffuses rapidly through a

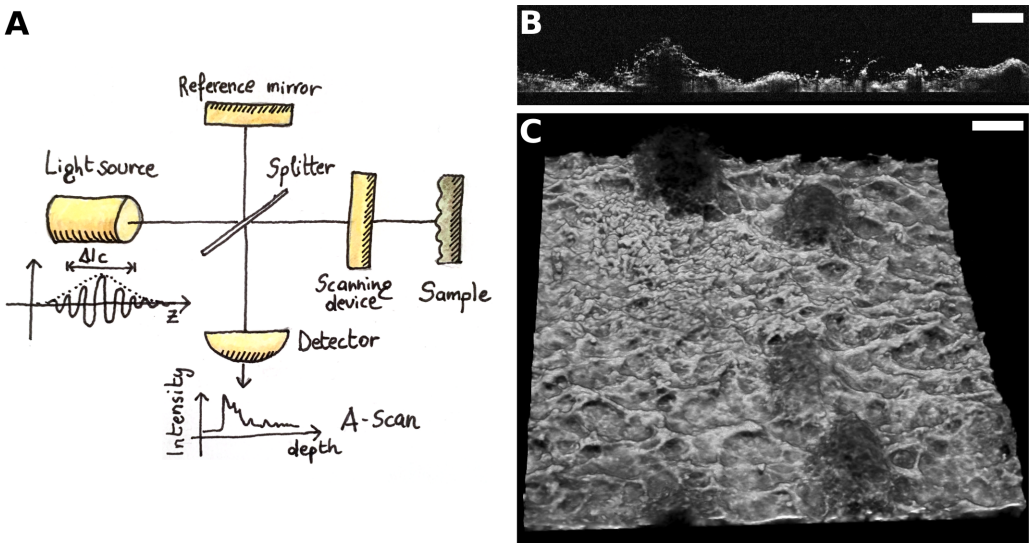

Figure 8 – **Optical coherence tomography (OCT)**. OCT is an interferometric technique to scan the tridimensional structure of a sample. A depicts the working principle of OCT. A low coherence light beam (coherence length of ΔIc) is split between a reference arm of known length and a sample arm. The interference pattern of the reflected light reflected from both arms is processed to obtain a depth profile of the sample reflectance (A scan). The sample is then scanned in the horizontal direction to obtain a cross-section composed of multiple A scans, termed a B scan (B). The sample is finally scanned in the third direction to obtain a tomography of the sample (C). Vertical and lateral resolutions vary with the lens and the reflective index of the imaging medium. The size of the field of view ranges from few millimeters up to 20 mm. The sample scans in B and C are images of a phototrophic biofilm studied in this dissertation (resolution of 11.1 μm x 11.1 μm x 2.18 μm in x, y, z direction respectively, covering a field of 10 mm x 10 mm x 2.2 mm). B also shows that the signal-to-noise ratio attenuates in tall biofilm portions. The internal structure of such structures results "shaded". Scale bars: 1 mm. A is reproduced from [82].

silicon rubber membrane that covers the tip of the capillary, and, in contact with the polarized cathode, it reduces to water, while the silver anode oxidizes to Ag^+. This produces an electrical current, measured with a pico-amperometer, that is directly proportional to the concentration of oxygen around the cathode [86;133]. A silver guard cathode prevents interferences from the oxygen dissolved in the electrolyte solution [86].

Micro-profiles of dissolved oxygen concentration have been extremely instrumental in characterizing the mass transfer patterns within and around biofilms. The thickness of the DBL and the effective diffusivity can be estimated from microsensors measurements around and within biofilm clusters [50;246;95;106]. Further, micro-profiles within microbial aggregates were used to characterize the ecological and metabolic interaction between neighboring subpopulations [124;179]. Although based on several assumptions, oxygen concentration micro-profiles can also be used to estimate metabolic rates [14], while Revsbech and colleagues introduced a method to estimate the gross photosynthetic production exploiting the fast response of oxygen microsensors [86;183]. Overall, the micro-scale characterization of the chemical environment permitted by microsensors has been pivotal for the understanding of diffusion-reaction dynamics in biofilms, and associated ecological interactions.

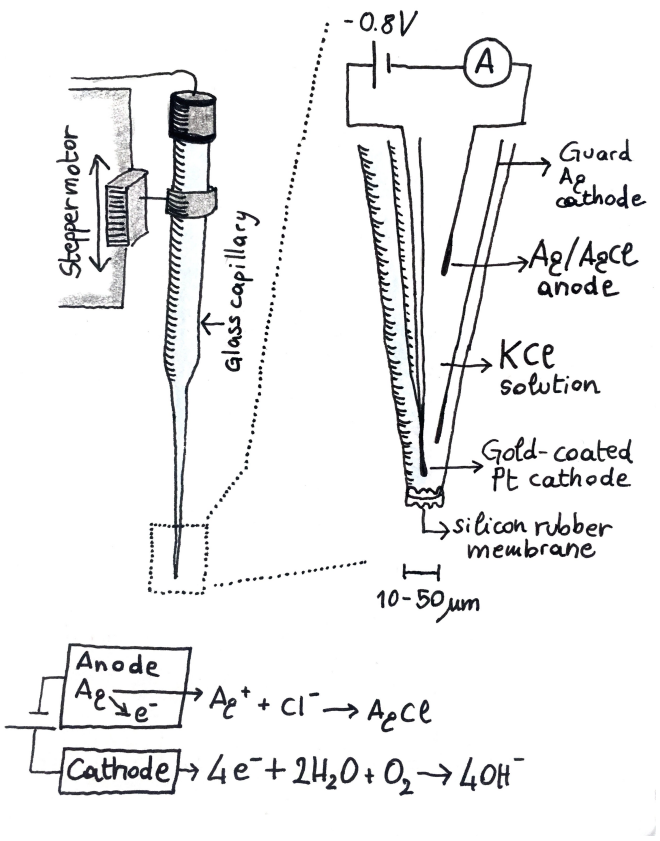

Figure 9 – **Clark-type oxygen microsensor.** This widely used sensor is made of a glass capillary mounted on a digitally controlled stepper motor for the collection of vertical profiles. Oxygen dissolves through a permeable silicon membrane on the tip of the capillary into an electrolyte solution. Positioned close to the sensor tip, a platinum cathode is electrically charged to reduce the dissolved oxygen to water, while the connected silver anode, oxydized to AgCl, is positioned further up from the sensor tip. The current between the two electrodes is proportional to the concentration of oxygen at the sensor tip, and it is measured with a picoamerometer (A).

Concluding remarks

Biofilms are matrix-embedded microbial communities that occupy most habitats on Earth, with enormous ecological, medical, and industrial relevance [77;89]. Despite their diversity, they are all characterized by conspicuous spatial organization. Spatial patterns emerge from local processes, but influence the biofilms overall functioning. Both active and passive processes contribute to the emergence of the biofilm chemical heterogeneity and tridimensional architecture, including nutrient uptake, mass transfer, growth, EPS production, detachment, and flow-induced compaction. Hydraulics represent a major abiotic cue in biofilm habitats, and its powerful ecological consequences are mostly mediated by the biofilm spatial features. Fluid flow modifies directly or indirectly the biofilm architecture which, reciprocally, modulates the local flow patterns. The interplay between the biofilm structure and the surrounding hydrodynamic elements, such as turbulent eddies, is driven by their relative spatial scale. While at the small spatial scale of a single cell, diffusion alone can regulate mass transfer, the topology of a biofilm can interact with larger flow patterns, thereby modulating the mass transfer regime [152].

Despite the many apparent advantages that the biofilm spatial organization confers to the community as a whole, it remains unclear whether it is indeed the product of a coordinated behavior or if it emerges from the uncoordinated response of single cells combined with passive physico-chemical interactions [147]. For instance, a smoother and more robust architecture developing under strong shear can emerge simply from the flow-induced scouring of the biofilm asperities without any requirement for community-level coordination [41]. A rougher and finger-like biofilm architecture can passively develop from vertical gradients in nutrient availability [167]. Analogously, the chemical heterogeneity within biofilms can emerge from the uncoordinated interaction between cell metabolic activity and mass transfer. Nonetheless, examples of costly coordinated behaviors within biofilms have been described. For instance, *Bacillus subtilis* cells within a biofilm engage in prominent division of labor mediated by the secretion of quorum-sensing molecules [31;119;240]. Heterotrophic cells in benthic biofilms can secrete signaling molecules and nutrients to nurture their autotrophic associates, inducing biofilm formation and the secretion of EPS [34]. Hence, the emergence of the biofilms architectural features and spatial organization remains an elusive eco-evolutionary process [147].

Despite this uncertainty, spatial features have important ecological consequences. As noted by Bernhardt et al. [15], ecosystems may be ultimately understood from their patterns in biomass production, respiration and photosynthesis, which are fundamentally linked to the abiotic drivers acting on the ecosystem. However, streams and rivers are characterized by a reduced coherence between environmental drivers and ecosystem processes as a consequences of their longitudinal gradients, the **allochthonous** influences of their catchment, and variability in hydrological regime [15]. Benthic biofilms are pivotal contributors to lotic metabolic regimes, and their spatial organization represents a fundamental link between their micro-scale processes and macroscopic functions. Therefore, understanding spatial features emerging in benthic biofilms holds the potential to shed some light on the currently elusive connection between environmental conditions and whole-ecosystem metabolism in streams and rivers.

1 Automated 3D Optical Coherence Tomography to Elucidate Biofilm Morphogenesis over Large Spatial Scales

Research articled published in the *Journal of Visualized Experiments (JoVE)*
Publishing date: 21st August 2019
URL: https://www.jove.com/video/59356
DOI:10.3791/59356

Authors: **Anna Depetris**[1], **Antoine Wiedmer**[2], **Michael Wagner**[3], **Sebastian Schäfer**[4], **Tom J. Battin**[1], **Hannes Peter**[1]

[1]Stream Biofilm and Ecosystem Research Laboratory, School of Architecture, Civil and Environmental Engineering, Ecole Polytechnique Fédérale de Lausanne
[2]Plateforme technique, School of Architecture, Civil and Environmental Engineering, Ecole Polytechnique Fédérale de Lausanne
[3]Water Chemistry and Water Technology, Engler-Bunte-Institut, Karlsruhe Institute of Technology
[4]Thorlabs GmbH

AW built the installation and the software packages with the support of AD; AD and AW prepared the software packages for image analysis; AD, HP, and TJB wrote the paper and conceived the setup and experiments; AD performed the experiment; MW and SS advised on the OCT setup and measurements. The Video and Supplementary Files are available in the online version of this paper.

Summary

Microbial biofilms form complex architectures at interphases and develop into highly scale-dependent spatial patterns. Here, we introduce an experimental system (hard- and software) for the automated acquisition of 3D optical coherence tomography (OCT) datasets. This toolset allows the non-invasive and multi-scale characterization of biofilm morphogenesis in space and time.

Abstract

Biofilms are a most successful microbial lifestyle and prevail in a multitude of environmental and engineered settings. Understanding biofilm morphogenesis, that is the structural diversification of biofilms during community assembly, represents a remarkable challenge across spatial and temporal scales. Here, we present an automated biofilm imaging system based on optical coherence tomography (OCT). OCT is an emerging imaging technique in biofilm research. However, the amount of data that currently can be acquired and processed hampers the statistical inference of large scale patterns in biofilm research. The automated OCT imaging system allows covering large spatial and extended temporal scales of biofilm growth. It combines a commercially available OCT system with a robotic positioning platform and a suite of software solutions to control the positioning of the OCT scanning probe, as well as the acquisition and processing of 3D biofilm imaging datasets. This setup allows the in situ and non-invasive autonomous monitoring of biofilm development and may be further developed to couple OCT imaging with macrophotography and microsensor profiling.

Introduction

Biofilms are a highly successful microbial lifestyle adaptation and these interphase-associated and matrix-enclosed communities of microorganisms dominate microbial life in natural and industrial settings [75;76]. There, biofilms form complex architectures, such as elongated streamers [223], ripples [225] or mushroom-like caps [5] with important consequences for biofilm growth, structural stability and resistance to stress [7]. While much about biofilm structural differentiation has been learned from work on mono-species cultures grown in miniature flow chambers, most biofilms are highly complex communities often including members of all domains of life [7]. Appreciating these complex biofilms as microbial landscapes [12] and understanding how biofilm structure and function interact in complex communities is thus at the forefront of biofilm research.

A mechanistic understanding of the morphogenesis of complex biofilms in response to environmental cues requires carefully designed experiments in conjunction with spatially and temporally resolved observations of biofilm physical structure across relevant scales [150]. However, the non-destructive observation of biofilm growth in experimental systems has been severely limited by logistic constraints such as the need to move samples (*e.g.*, to a microscope) often damaging the delicate biofilm structure.

The protocol presented here introduces a fully automated system based on optical coherence tomography (OCT), which allows the in situ, non-invasive monitoring of biofilm morphogenesis at the mesoscale (mm range). OCT is an emerging imaging technique in biofilm research with applications in water treatment and biofouling research, medicine [142] and stream ecology [242]. In OCT, a low coherence light source is split into a sample and reference arm; the interference of the light reflected and scattered by the biofilm (sample arm) and the light of the reference arm is analyzed. A series of axial intensity profiles (A-scans) which contains depth-resolved structural information is acquired and merged into a B-scan (a cross section). A series of adjacent B-scans composes the final 3D volume scan [242]. OCT provides a lateral optical resolution in the range of approximately 10 μm and is therefore well suited to study mesoscopic structural differentiation of biofilms [242;97]. For a more detailed description of OCT, refer to Drexler and Fujimoto [63] and Fercher and colleagues [72]. Although the field-of-view of a single OCT xy-scan reaches up to hundreds of square micrometers, larger-scale patterns cannot be quantified by means of OCT in a single scan. With respect to biofilms in natural habitats such as streams and rivers, this currently limits our ability to assess biofilm morphogenesis at

scales matching the physical and hydraulic template of the habitat.

In order to surpass these spatial limits and to acquire OCT scans automatically, a spectral-domain OCT imaging probe was mounted on a 3-axes positioning system. The installation permits the automated acquisition of several OCT scans in an overlapping mosaic pattern (tile scan), effectively achieving the tomographic imaging of surface areas up to 100 cm^2. Furthermore, the high positioning precision of this system enables to reliably monitor the growth and development of biofilm features in specific sites during long-term experiments. The system is modular and individual components (*i.e.*, positioning device and OCT) of the installation can be used as standalone solutions or flexibly combined. Figure 1.1 provides an overview of the hard- and software components of the installation.

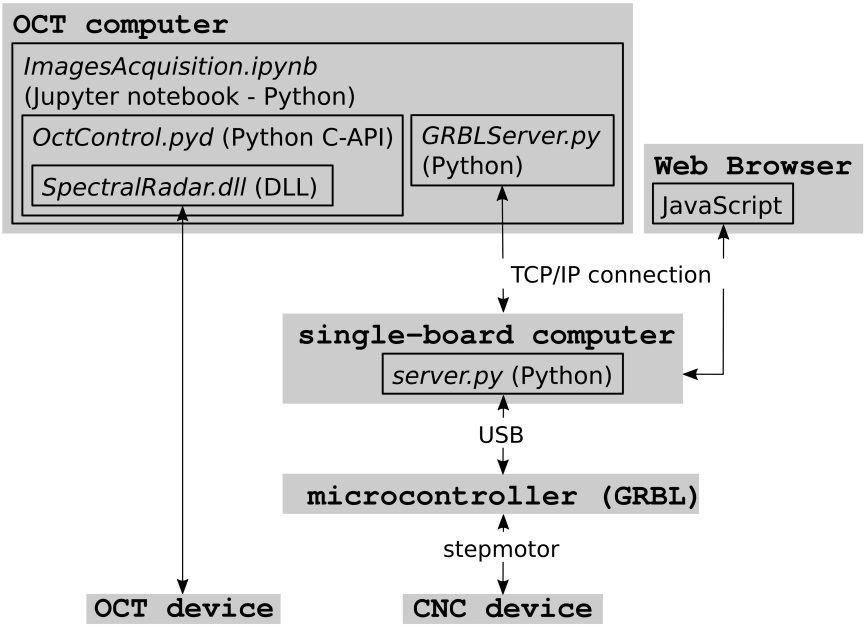

Figure 1.1 – **Overview of hard- and software components.** The stepmotors of a GRBL-controlled positioning device are wired to a microcontroller, connected via USB to a single-board computer. The GRBL server is installed on the latter, and motion of the positioning device can be controlled from any web browser via TCP/IP connection. Alternatively, navigation of the positioning device can be performed from a Python-encoded Jupyter notebook (`OctAcquisition.ipynb`, Supplementary File 2) using the `GRBLServer.py` library. The OCT system is connected to a separate computer from which automated OCT scan acquisition can be performed via a Python script.

The system was tested with a commercially available GRBL-controlled CNC positioning device (Table of Materials). The operating distances of this specific positioning platform are 600×840×140 mm, with a manufacturer-indicated accuracy of ± 0.05 mm and a programmable resolution of 0.005 mm. GRBL is an open-source (GPLv3 License), high-performance motion control for CNC devices. Therefore, every GRBL-based (version > 1.1) positioning device should be compatible with the guidelines and software packages presented here. Moreover, the software could be adapted to other stepmotor controllers with STEP-DIR input type with few modifications.

The OCT device used to assess the performance of the system (Table of Materials) features a low coherence light source with a center wavelength of 930 nm (bandwidth = 160 nm) and adjustable reference arm length and intensity. In the example presented here, an immersion adapter for dipping

the OCT probe into flowing water was also used (Table of Materials). The software package developed here for automated OCT scan acquisition critically depends on the SDK provided together with the specific OCT system, however, OCT systems from the same manufacturer with different scan lenses and central wavelengths should be readily compatible.

The GRBL device is controlled by a web server installed on a single-board computer (Figure 1.1). This grants remote control of the device from any computer with local network or internet access. The OCT device is controlled by a separate computer, allowing the operation of the OCT system aside the automated experimental setup. Finally, the software packages include libraries to synchronize OCT probe positioning and OCT scan acquisition (*i.e.*, to automatically acquire 3D imaging datasets in a mosaic pattern or in a set of defined positions). Defining the position of the OCT probe in 3D effectively allows to adjust the focal plane specifically for (regional) sets of scans. Specifically, on uneven surfaces, different focal planes (*i.e.*, different positions in z direction) can be specified for each OCT scan.

A set of software packages was developed to process raw OCT scans (Table 1.1). Navigation of the positioning device, OCT scan acquisition and dataset processing are performed with Python-coded Jupyter notebooks, which allow remarkable flexibility in the development and optimization of the software. Two worked and annotated examples of such notebooks (for image acquisition and processing, respectively) are available from link. They are intended as starting points for customization of the method. A Jupyter notebook is a web browser based application which contains cells with annotated Python code. Each step is contained in a cell of the notebook, which can be executed separately (*e.g.*, by pressing `Cell | Run`, or with the key sequence: `Ctrl + Enter or Shift + Enter`). Due to the different length of the light path through the scan lens (spherical aberration) [131], the raw OCT scans appear distorted (Figure 1.2A). We developed an algorithm to automatically correct for this distortion in acquired OCT scans (contained in `OctProcessing.ipynb`, Supplementary File 1). Furthermore, biofilm morphology can be visualized as a 2D elevation map, as was previously used in membrane systems [79], and we illustrate how elevation maps obtained from scans taken in a tiling array can be stitched.

Finally, the functionality of the described laboratory installation is illustrated using a flume experiment in which a phototrophic stream biofilm is exposed to a gradient of flow velocity.

Protocol

1. **Setup of the Positioning Device**

    1. Wire the positioning device to a microcontroller board, following the instruction in https://github.com/grbl/grbl/wiki/Connecting-Grbl.
    2. Connect the microcontroller to a single-board computer with internet connection via a USB cable and install the GRBL server as described in https://gitlab.com/FlumeAutomation/GRBL_Server.git. Now the positioning device should be navigable from a webpage hosted at http://IP:5020/. Alternatively, the positioning device can be navigated with a Python script, as demonstrated in the first part of the worked example `OctAcquisition.ipynb` (Supplementary File 2).

2. **OCT Setup**

    1. Mount the OCT probe to the positioning device using a compatible dove-tail holder. If required, install an immersion adapter on the objective lens.

Table 1.1 – **Software components.**

Software	Description
`stepcraft.py`	A Python library to control the positoning device. It contains definitions for navigating and homing the device.
`OctControl.cpp`	C++ code derived from the Software Development Kit (SDK) distributed with the OCT system. This has to be compiled using VisualStudio 2017, PythonC/API and the SDK.
`OctAcquisition.py`	A Python library containing the commands for taking OCT scans in selected positions and defining the scan tiling pattern.
`OctAcquisition.ipynb`	Jupyter notebook used to navigate the positioning device, acquire OCT scans and for automated scan acquisition.
`OctCorrection.py`	A Python library defining the functions used for the correction of the raw OCT scans and background subtraction.
`OctProcessing.py`	A Python library containing the functions to calculate and sticth elevation maps.
`OctProcessing.ipynb`	Jupyter notebook to visualize, correct and process OCT scans. This also contains an example of biovolume calculation.

2. Position the computer and OCT base unit on a bench next to the experiment (*e.g.*, microfluidic devices, flow chambers, flumes, filtration systems). Make sure that the optical cord (maximum length of approx. 1.8 m) is freely moving, long enough to reach all intended locations and not interfering with the experimental setup.
3. Install the OCT system together with the available software as described by the manufacturer.
4. Install the software packages for automated OCT scan acquisition as described in https://gitlab.com/FlumeAutomation/automated-oct-scans-acquisition.git.

3. **Image Acquisition**

1. Power on the OCT system and the positioning device. Make sure the device can move freely.
2. Open the file `config.json` in a text editor. Edit the config.json file to adjust image acquisition parameter (Table 1.2), such as the refractive index (1.33 for water at 20°C, 1.00 for air), scan speed, as well as the destination folder for acquired data and metadata.
3. Define the size of the field-of-view (FOV) and the number of A-scans per B-scan in `config.json`.

   NOTE: These two parameters determine the size of the voxels of the final dataset and the size of the output file and should match the optical resolution of the probe (x-y voxel size should not be smaller than half of the optical resolution). The number of A- and B-scans affects the spatial extent to be covered which trades-off against available disk space and processing power.
4. Define the signal boundaries of the output OCT scan in `config.json`. These depend on the type of sample. It is thus recommended to determine these parameters based on intensity histograms of a set of preliminary scans. Save the changes in `config.json`.

5. Navigate the OCT probe to a site of interest. Focus the sample and adjust the reference arm and light source intensity for optimal image quality. Repeat this procedure for a number of positions and note the coordinates.

   NOTE: This will allow the subsequent automatic OCT scan acquisition around these reference points. Note that the reference arm length and intensity cannot be changed during automated image acquisition.

6. Open the `OctAcquisition.ipynb` file (Supplementary File 2) in Juypter Notebook. Each cell contains code to perform specific tasks and can be run separately via pressing `Cell | Run`, or `Ctrl + Enter or Shift + Enter`.

   1. Set the path to the required library configuration parameter.
   2. Connect to the positioning device and initialize the OCT.
   3. Calibrate the positioning device (*i.e.*, perform a "homing").
   4. Acquire the datasets covering the positions of interests in single-scan or mosaic pattern, specifying the number and the overlap (e.g., 30%) of neighboring tiles.
      NOTE: The memory is allocated prior to the scan, which optimizes computer resource use. Data is saved in 8 bits *.raw format to save storage space, into the destination folder defined in config.json, using the time stamp and the position as naming convention (`i.e.,%Y%m%d_%H%M%S_<position>`). Metadata including the OCT settings and coordinates are saved in the same folder in a `*.json` file with the same naming convention. Depending on settings such as FOV and resolution, file size may reach up to 1.5 GB per OCT scan.

7. To avoid abortion of data acquisition, make sure that there is sufficient free disk space or continuously move OCT datasets to an external hard drive.

4. **Image Correction and Display**

   1. Open the Jupyter notebook `OctProcessing.ipynb` (Supplementary File 1) for a worked example of OCT image processing (correction of distortion, background subtraction, calculation of elevation maps, elevation map stitching).
   2. If required, crop OCT scans in order to exclude spurious signals and reoriented the dataset (biofilm should appear above the substratum).
   3. Correct for spherical aberration. This is accomplished by a correction algorithm that utilizes a highly reflective surface known to be flat (*e.g.*, bottom of the flume, substratum). First, the algorithm defines a grid of 20×20 vertical lines regularly spaced across the xy-plane of the OCT scan. Then, it selects a circular area around each point and averages signal intensities along the vertical profile (Figure 1.2B). The vertical profiles are processed with a modified Gaussian filter:
      $\omega(x) = e^{\frac{1}{2}(\frac{x}{\delta})^2} + C$
      where x is the input signal, and δ its standard deviation, while C is determined such as:
      $\int_{-a}^{a} \omega(x)\,dx = 1$
      The reference surface is localized as local maxima in each of these profiles. Misidentified points are filtered based on the positions of their neighbors in three dimensions (Figure 1.2C). Finally, a $2^n d$ order polynomial surface reflecting the distortion introduced by the scan lens is fitted across these points (Figure 1.2C). The fitted surface is then used to shift each pixel in z-direction, thus obtaining a flattened image. The parameters of this algorithm should be adjusted to the characteristics of the OCT scan.

4. Correct for background noise. Identify an empty area of the image (typically above the biofilm) and calculate the average background intensity, which is then subtracted from the intensity values of the image to produce a final corrected OCT image (Figure 1.2D).
5. Define a reference surface (*e.g.*, the substratum) and compute an elevation map from the 3D OCT dataset. In this step, the corrected images are thresholded and the thickness of the biofilm is calculated for each coordinate (x,y) of the binary mask (Figure 1.3A). Thickness values are then assigned to a 2D matrix of the size of the original image in x and y directions. An image is rendered in which the elevation of the surface is reported as grayscale value (Figure 1.3C).
6. In case several OCT scans are taken in a mosaic pattern, define the number of rows and columns and stitch the elevation maps. Figure 1.4 presents examples of stitched elevation maps, covering the broad range of spatial scales and resolutions achievable with the described setup.

Table 1.2 – **OCT parameter settings.**

Parameter	**Value**	**Description**
Ganymede	1, 2, 3	Choice of OCT system and version
Probe	1, 2	Choice of scan lens
nAscans	32-900	Number of A-scans per B-scan
nBscans	1-900	Number of B-scans
nCscans	128-1024	Number of depth pixels
X	0.1-10	Size of image in x-direction (mm)
Y	0.1-10	Size of image in y direction (mm)
refr	1-1.6	Refractive index (1 for air, 1.33 for water)
avg_Ascans	3	Number of A-scan averaging
scanspeed	1,2,3	A-scan Rate (5.5, 15 and 36 kHz)
Path	"../%Y_%m_%d_%H_%M_%S"	Destination folder for the acquired OCT scans, uses time stamp as naming convention
colorBoundaries	[0-256, 0-256]	Color boundaries of the acquired scans

Representative Results

We demonstrate the functionality of the automated OCT imaging system using a flume experiment designed to study the spatio-temporal morphogenesis of phototrophic stream biofilms. A gradually narrowing geometry of the flumes induced gradients in flow velocity along the center of the flume (see reference [151]). The temporal development and structural differentiation of biofilm was monitored over 10 days with the aim to better understand the effects of hydrodynamic conditions on biofilm morphogenesis. Surface morphology of the biofilm was quantified using the toolset described above (Figure 1.4A). Biovolume was calculated (see worked example `OctProcessing.ipynb`, Supplementary File 1) for a square moving window with 3.6 mm edge length (Figure 1.4B) for each position along the flow velocity gradient (Figure 1.4C). Biofilm accumulation significantly decreased with increasing

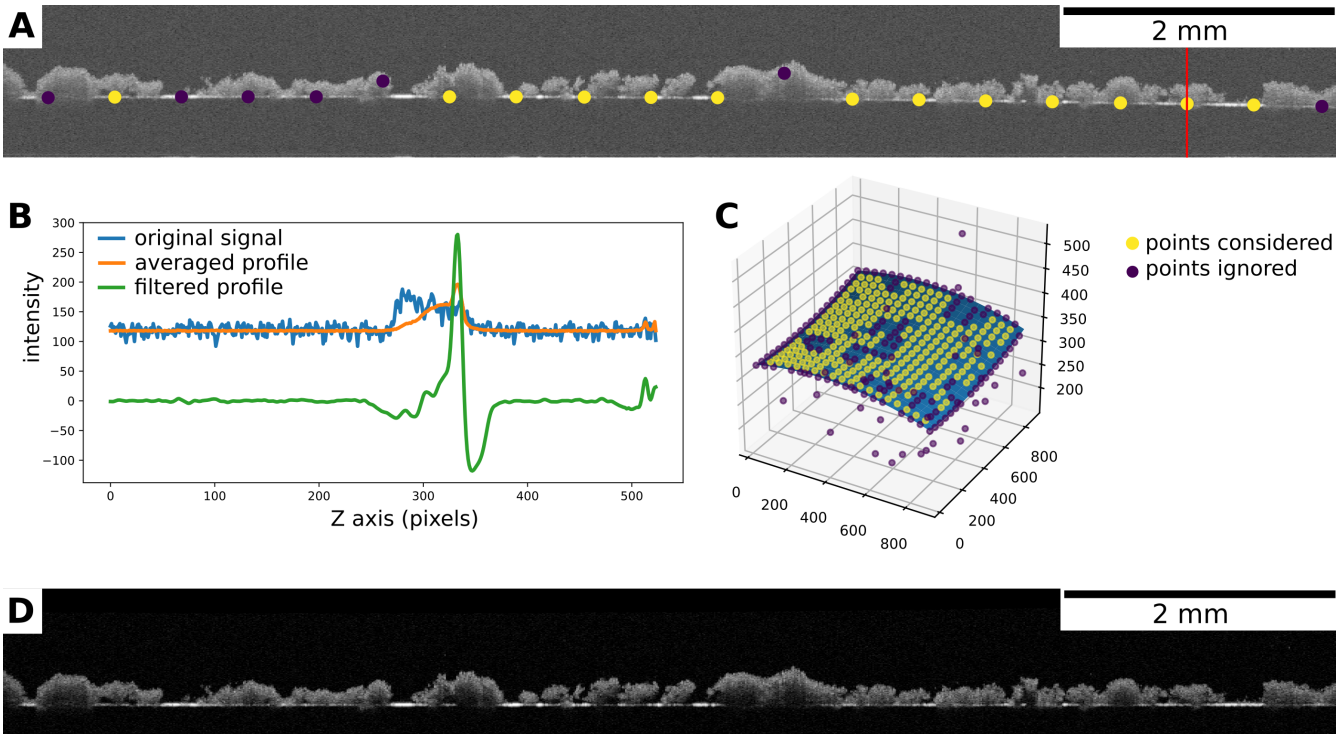

Figure 1.2 – **OCT scan correction workflow.** Panel A shows a non-processed B-scan of biofilm growing on a flat plexiglass surface. The image is distorted (bend) because of differences in path length of the low coherence light through the lens. OCT image distortion can be corrected by identifying a strongly reflecting, flat reference surface in the image. First, 20×20 reference points are evenly distributed across the entire stack of images. In each of these points, the image signal is averaged across a circular area (in x-y direction) for each depth (z plane), obtaining an averaged depth profile of signal intensity. Then, a modified Gaussian filter is applied to of each of the 400 reference profiles. Panel B provides an example of the original signal along the depth profile indicated by the vertical red line in Panel A, the averaged depth profile, and the same profile after the modified Gaussian filter has been applied. The modified Gaussian filter allows the identification of local maxima in signal intensity, thus identifying the location of the strongly reflecting reference surface. Correctly identified reference points are then selected based on the coordinates of their neighbors in three dimensions. In the example in panel C, the yellow points were kept for subsequent image correction whereas purple ones were discarded. A 2^{nd} order polynomial surface is then fit to the correctly placed reference points and used to correct the distortion in the original OCT image by shifting pixels in z direction. Average background intensity is estimated from an empty area of the image and subtracted from the corrected images. Panel D shows the same B-scan after correction and background subtraction.

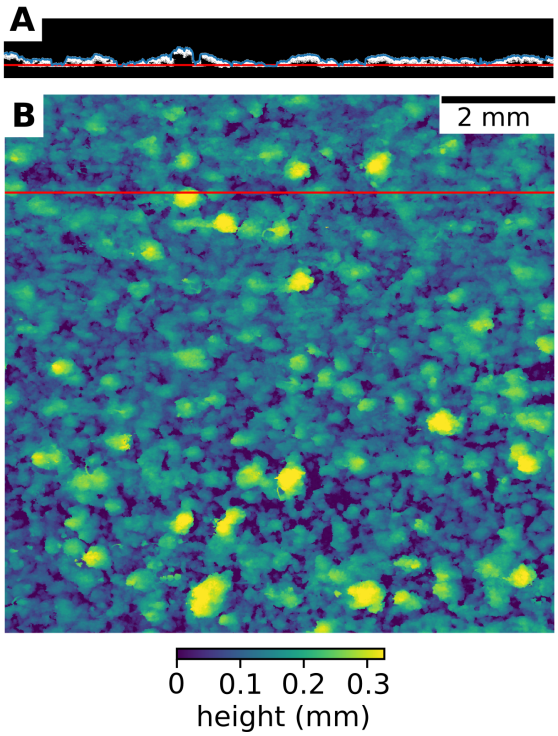

Figure 1.3 – **Elevation maps.** Biofilm topologies can be visualized as 2D elevation maps in which thickness of the biomass is color coded. For this, a 3D OCT image is thresholded and biofilm thickness calculated as the distance of the uppermost signal to the substrate. Panel A shows the binary mask of a B-scan obtained after thresholding. The blue line indicates the uppermost signal while the red line shows the reference surface. Panel B shows an example of the obtained elevation map, scaled according to the axial resolution of the OCT probe. The red line indicates the position of the B-scan in Panel A.

flow velocity (indicated as the distance from the widest part of the flume; Figure 1.4). Importantly, this experimental setup allows a continuous measurement of structural parameters (*e.g.*, biovolume, thickness, roughness) along large spatial gradients. Hence, this new tool provides the means to gain insights into relationships between biofilm structure and environmental cues.

Discussion

OCT imaging is well suited to resolve structures in the micrometer range with a FOV of several square millimeters. It is thus a powerful tool for biofilm research [242;194]. However, OCT is currently limited to a maximum scan area of 100 - 256 mm^2, while biofilm structural patterns often exceed this spatial scale [78], especially when morphological differentiation is driven by large scale environmental gradients [145]. The automated OCT imaging system described in this protocol extends the surface area characterized by OCT to several square centimeters, effectively enabling us to monitor biofilm morphological differentiation over a relevant range of spatial scales (from few millimeters to several centimeters). The high positioning accuracy (within 16 μm; Figure 1.5) allows to accurately monitor the structural development of biofilms over extended periods of time, effectively boosting the opportunities for obtaining a mechanistic understanding of the drivers of biofilms morphological differentiation. At the same time, this in situ biofilm characterization technique is non-invasive and minimizes the

interference with biofilm growth. The image processing solutions presented here build on previously employed analyses of biofilm OCT datasets [79], yet the automation provides tools for unprecedented time- and space resolved OCT dataset analyses.

This system was conceived and benchmarked with a specific OCT device, as described in the protocol. Critical steps in the protocol mainly concern the setting of OCT resolution and focusing, which are both critical for high image quality. A limitation of the correction of spherical aberrations routine is that it depends on the presence of a highly reflective flat surface. Alternatively, a standard correction surface could be measured, and then used to correct OCT scans. Furthermore, the stitching of OCT scans depends on sufficient structural features to align neighboring scans. In case of uniform biofilm distribution or low biofilm coverage, stitching may be achieved relying solely on the precision of the positioning device. Finally, as in any other image processing pipeline, when setting up these tools, it is critical to carefully assess the performance of the processing algorithm on a set of representative scans before handling batches of images. However, both hard- and software were designed to provide full modularity of the individual parts. More specifically, this system can be easily adapted to work with other tools for biofilms characterization such as macro-photography imaging using hyperspectral cameras or microsensor profiling. The coupling of structural information with localized gradients in resources around and within biofilms will provide novel and pivotal insights into the way how biofilms are adapted to optimize resource allocation. The flexibility is also implemented through the use of Jupyter notebooks, an open-access, fast and versatile software developing tool.

A critical limitation of OCT imaging in general remains the disability to resolve rapidly moving objects. For instance, streamers elongating into and moving with the flow are not accurately depicted. The applicability of this tool is thus limited to relatively fixed, non-moving biofilm structures. The system is optimized to work autonomously, however, initial settings and if necessary, the adjustment of focus and illumination, are still required. This represents a significant limitation if samples differ significantly in density and reflective properties. Full automation, including software-guided focusing and adjustment of illumination may however be achieved using similar principles (*e.g.*, stepper motors and software-hardware feedbacks) as described here.

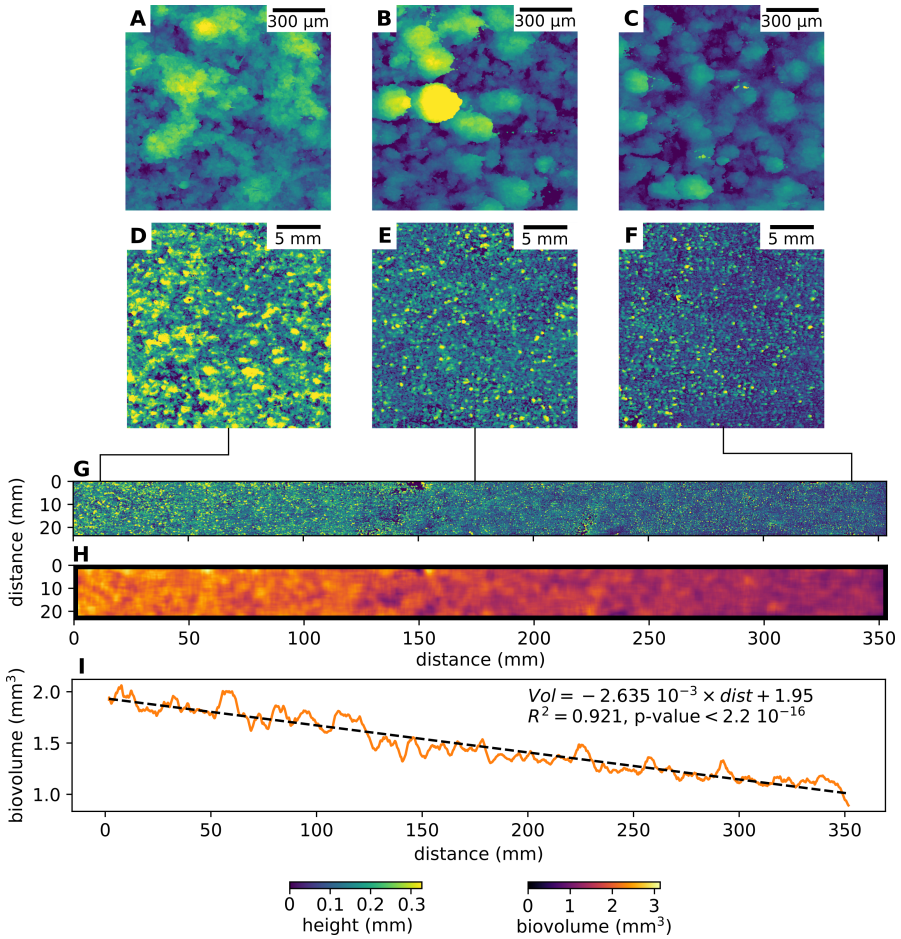

Figure 1.4 – **Representative results showing the effect of flow velocity on biofilm growth.** We studied phototrophic stream biofilm morphogenesis along a gradient in flow velocity using flume experiments. Flow velocity increased with distance from the inlet of the flume. After 10 days of growth, biofilm morphology was characterized by automated OCT at different resolution and covering different spatial scales. Elevation maps (A, B and C) demonstrate the morphology of biofilm grown under low, medium and high flow velocity, respectively. These elevation maps are calculated from OCT scans with voxels size in x, y direction of 4 μm. The scan surface area is a square of 3.6 mm edge length. Panels D, E and F show elevation maps (low, medium and high flow velocity, respectively) obtained by stitching 3×3 OCT scans with a voxel size in xy-direction of 11 μm, scan area of 10 mm^2 and an overlap between neighboring scans of 30%. Panel G shows an elevation map of biofilm growing along the entire velocity gradient achieved in this flume experiment. It was obtained by stitching 3×51 OCT scans with a voxel size in xy-direction of 40 μm, scan area of 10 mm^2 and an overlap between neighboring scans of 30%. The total scan area achieved is 24×353 mm. Panel H reports biovolume in a square moving window of 3.6 mm edge. Average biovolume significantly decreased as a function of distance from the inlet (I).

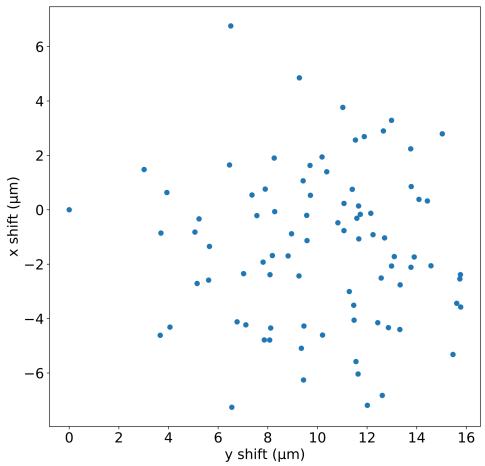

Figure 1.5 – **Precision test for the positioning device.** The precision of the positioning device was assessed by mounting a 20.2 Megapixels camera equipped with a 35 mm macro lens on the positioning device, focused on a colored mark. The positioning device was moved in a random direction away from the mark and then positioned back for a total of 80 cycles. The position of the mark was then compared. The figure shows the shift in x and y direction with respect to the first picture. Note that the maximum shift is approximately 0.0216 μm in yx-direction and even less in x-direction.

2 Morphogenesis and oxygen dynamics in phototrophic biofilms growing across a gradient of hydraulic conditions

Research article accepted in *iScience*

Authors: **Anna Depetris**[1], **Hannes Peter**[1], **Ankur Deep Bordoloi**[2], **Hippolyte Bernard**[1], **Amin Niayifar**[1], **Michael Kühl**[3], **Pietro de Anna**[2], **Tom J. Battin**[1]

[1]Stream Biofilm and Ecosystem Research Laboratory, School of Architecture, Civil and Environmental Engineering, Ecole Polytechnique Fédérale de Lausanne
[2]Institute of Earth Sciences, University of Lausanne
[3]Marine Biological Section, Department of Biology, University of Copenhagen

AD, TJB and HP designed the experiments, AD conducted the experiment and analyzed the data, MK advised on microsensor measurements and data analyses, PDA and AB performed the computational simulations of fluid dynamics around idealized biofilms clusters, HB and AN performed the computational simulations of fluid dynamics within the flumes, AD wrote the paper with support from all other authors.

Summary

Biofilms are microbial communities with an architecture that influences their emergent properties and ecological success. Using flume experiments and automated optical coherence tomography (OCT), we studied the morphogenesis of phototrophic biofilms along a gradient of hydraulic conditions characteristic for small streams. A compact and coalescent biofilm formed under elevated bed shear stress, whereas protruding clusters separated by troughs formed under reduced shear stress. This morphological differentiation did not linearly follow the experimentally imposed hydraulic conditions. Rather, a threshold effect emerged around the breakpoint shear stress of ~0.08 Pa. While amplicon sequencing did not reveal significant differences in biofilm community composition, morphogenesis was probably linked to local biomass displacement and reciprocal interactions between the biofilm structure and

hydraulics. Automated micro-profiling combined with OCT mapped oxygen concentration within and around the biofilm structures, providing evidence for biofilm-induced alterations of the mass transfer. Our findings reveal a coupling between architectural plasticity, efficient mass transfer and resistance to shear stress in a phototrophic biofilm.

Introduction

Microorganisms form surface-attached and matrix-enclosed biofilms in numerous ecosystems [77]. A conspicuous and ubiquitous feature of biofilms is the differentiation into physical structures (*i.e.*, architectures) and the formation of spatial patterns and stratifications at various scales. Despite the importance of spatial organisation for ecological systems in general [189], relatively little is known on the formation of the higher-order structures in complex biofilms. This is unexpected given that biofilm architecture seems to be related to critical processes in many benthic ecosystems [7;74]. The study of the diverse physical structures of biofilms has been a mainstay in biofilm research. Reported architectures include cell clusters separated by voids [51;50;226;218], mushroom-like caps, streamers extending into the bulk liquid [98;218], ripples [149;225] and honeycomb-like patterns [10;94;233]. Redox balancing, mechanical instabilities, reciprocal interactions between growth and competition for nutrients, localized cell death and grazing by protists have been invoked as endogenous drivers of biofilm morphogenesis [254;257;58;248]. The bed shear stress imposed by fluid flow is an important exogenous driver of biofilm structural differentiation. It can trigger sloughing and deformation of biofilms [60;215;226], or the formation of patterns such as migratory ripples [225]. While dense and compact biofilms are better protected from shear stress and related drag fluid [229;245], tall and exposed clusters are more susceptible to sloughing or displacement [65]. Furthermore, the production of extracellular polymeric substances (EPS) can be modulated in response to high shear, conferring enhanced mechanical stability [10;208;244]. Fluid flow also affects the thickness of the diffusive boundary layer, the establishment of chemical gradients and thereby resource replenishment and biofilm growth [10;105;157;169;215;216;222]. Thus, the link between fluid flow and both biofilm growth and structure is complex, influenced by the balance between shear-induced biomass loss and enhanced mass transfer and growth rate [157;208;235;105;244]. At the same time, biofilm architecture can also modify the local flow patterns. In fact, mathematical models and experiments have shown that troughs between adjacent clusters alter the flow fields around the latter, allowing for fluid flow around the basal layers of the biofilm, thereby enhancing mass transport to these otherwise nutrients-limited areas [49;168]. Therefore, like in macroscopic landscapes such as coral reefs or forests, the structure of biofilms mediates in the biogenic construction of its immediate environment [76]. Our current understanding of biofilm morphogenesis and patterning largely rests on mathematical modeling. For instance, external mass transfer resistance imposed by a thick diffusive boundary layer may be counteracted by the formation of finger-like and rough biofilm architectures (*e.g.*, [238;167]). Here, models have shown that tall and exposed clusters grow faster than smaller clusters because they access more of the limiting resource (*e.g.*, nutrients, oxygen) in the bulk fluid. Local detachment can also influence biofilm morphogenesis. The erosion of structures protruding into the fluid flow may result in biofilms with low roughness, while sloughing, as linked to nutrient limitation at the biofilm base or the erosion of cells from the biofilm surface, can lead to rough and clumped architectures [41;110]. Such modeling efforts have influenced experimental studies on biofilm formation and morphogenesis that, however, remain often limited to mono-species bacterial biofilms growing on agar plates or in flow cells (*e.g.*, [26;198]). While such experiments have greatly advanced our understanding on the small-scale architecture of biofilms and interactions within them, they may poorly reflect the impact of complex fluid flow on biofilm morphogenesis and its characteristic length

scale as often encountered in natural biofilm habitats, such as streams. In fact, complex biofilms, whether in stream ecosystems [7] or the intestine [47], are often characterized by spatial patterns that exceed the dimensions of a typical flow cell. Approaches that provide high spatial resolution beyond the multi-millimeter scale are thus required to appreciate the governing physical, biological and ecological processes from which architectures and higher-order patterns emerge [12;67;144;243;257]. Here we applied an experimental and multi-scale approach to relate the structure and function of phototrophic biofilms to their hydraulic environment. We used an automated optical coherence tomography (OCT) system [55] to quantify the topography of the biofilm as a digital elevation model (DEM) over a large rectangular surface (0.025 m x 0.4 m). This approach is analogous to the *in situ* 3D imaging of forests and coral reefs providing quantitative and detailed structural information to test hypotheses relating structure to function of these ecosystems [36]. Biofilms grew in experimental flumes along an increasing gradient of flow velocity and shear stress. Our general hypothesis was that differing space-occupancy strategies arise from trade-offs between flow-induced shear stress and nutrient replenishment, thereby resulting in a patterned microbial landscape. Guided by numerical simulations of flow across idealized biofilm structures and oxygen concentration microprofiles, we further show that biofilm structures are able to modify their local environment.

Results and Discussion

Hydraulics affects biofilm architecture and patterning. We cultivated phototrophic biofilms from raw water from Lake Geneva to mimic their growth in the lake outlet, the Rhone River. Biofilms grew over 15 days in duplicate open-channel flumes (I and II, 1.5 m long) with a geometry designed to produce a hydraulic gradient (Figure 2.1, Supplemental Figure 2.7). Along this gradient, mean flow velocity ranged from 0.06 m s^{-1} to 0.13 m s^{-1}, and Reynolds number for open channel flow (Methods) increased from 793 to 1407, indicative of laminar to transitional flow, respectively. Numerical simulations further showed that the bed shear stress increased from 0.04 Pa to 0.13 Pa (Figure 2.1B). We used an automated OCT system [55] to characterize the biofilm surface topology at high resolution (40 μm, 40 μm and 2.18 μm in x, y, z dimensions) across several spatial scales — ranging from patches formed by multicellular clusters (~100 μm) to the higher-order patterns emerging at the scale of the entire biofilm landscape (0.4 m in length) (Figure 2.1C-G). The OCT scans did not evidence the presence of voids below the biofilm surface and were processed to obtain digital elevation models (DEM) of the biofilm surface topology [55]. After 15 days, biofilms developed into a clearly patterned landscape that followed the hydraulic gradient. Tall (up to 1.5 mm) clusters separated by troughs often containing small colonies (< 100 μm in height) dominated the biofilm landscape exposed to low flow velocity and shear (Figure 2.1D;F). Biofilms growing under high flow velocity and shear stress developed into thin and coalescing patches densely carpeting the bottom of the flume (Figure 2.1E;G). The formation of these biofilm structures in complex phototrophic biofilms corroborates predictions from modelling and observed in other experimental systems (*e.g.*, [49;41;167;226;218]). The contrasting morphotypes found at both extremes of the hydraulic gradient are hereafter referred to as SFM (slow-flow morphotype) and FFM (fast-flow morphotype). To quantify the changes in landscape features of mature biofilms (day 15) along the hydraulic gradient, we derived a suite of structural parameters from the DEMs using a moving window (24 mm edge length) approach (Supplemental Table 2.1). While biofilm height gradually decreased with increasing shear stress, its volume, porosity, substrate coverage, and accrual rate exhibited significant breakpoints along the gradient in shear stress (Figure 2.2, Supplemental Table 2.2). Biofilm volume, accrual rate and substrate coverage presented a significant positive relationship with shear stress above the threshold of ~0.08 Pa, but not below. This resulted in a more than 2-fold increase in biofilm accrual rate in FFM as compared to SFM. Shear-induced erosion can

determine the height of biofilm structures [41], which would explain the observed gradual decrease in biofilm height with increasing shear stress. Given that biofilms developing under high shear are usually denser than those growing under low shear [22], our results suggest that biomass accrual was more efficient under high shear. This is in line with previous experimental findings [244] and could be explained by enhanced mass transfer (*e.g.*, [127;128;222]). Above the breakpoint shear stress of ~0.08 Pa, biofilm porosity (*sensu* [167]) and textural correlation, a measurement of biofilm aggregation [101] tended to decrease with increasing shear stress (Figure 2.2, Supplemental Table 2.2). Microorganisms compete, besides nutrients and substrates, also for space, which can become a limiting resource for growth [135]. Therefore, the presence of low coverage areas in SFM is remarkable and indicates the existence of processes limiting the full occupancy of the available space. Increased biofilm porosity and aggregation allowing for advection within biofilm troughs may be advantageous when mass transfer is limited under slow flow [49;168]. Hence, the observed morphological pattern could represent an adaptive response to mass transfer limitation. Alternatively, clusters separated by voids could form as a consequence of detachment induced by nutrient limitation at the biofilm base combined with erosion of the cells on the biofilm surface [41]. However, as noted by Stoodley et al. [218], architectural differences may also underly differences in the community or EPS composition of the biofilm. Overall, these results suggest that the interplay between fluid flow and both biofilm architecture and growth dynamics are characterized by threshold effects as evoked by previous studies [32;105;157;208;235;244], and further advocate contrasting mechanisms underlying biofilm morphogenesis.

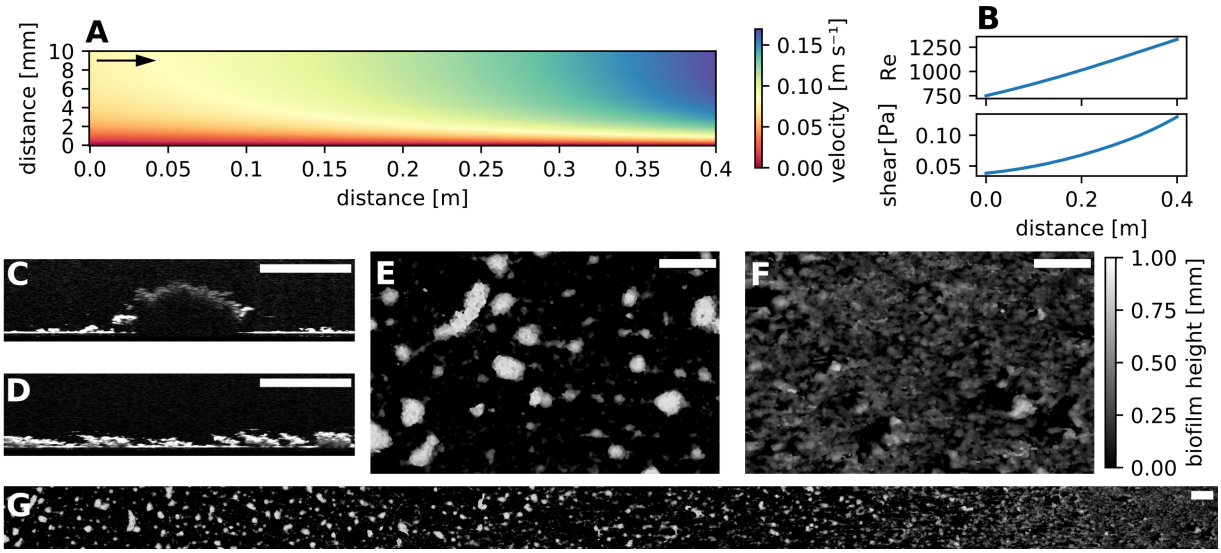

Figure 2.1 – **Architectural differentiation of phototrophic biofilms follows the hydraulic gradient.** The narrowing flume design from inlet to outlet (Supplemental Figure 2.7) resulted in a gradual increase in flow velocity and bed shear stress in flow direction. An axial cross-section of the simulated velocity field is shown (A), with distance in the flow direction and from the flume bed on the x and y axes, respectively. Reynolds numbers and bed shear stress also increased in the flow direction (B) Optical coherence tomography (OCT) produced stacks of cross-sections at high resolution. Representative scans are shown for low (C) and high shear regions (D). OCT scans were processed to quantify the biofilm surface topology as a digital elevation models (DEM), in which biofilm thickness is encoded as pixel grey-level. Shown is a DEM covering a rectangle of 0.025 x 0.4 m^2 along the hydraulic gradient (G), while enlarged details of the biofilm developed under low-shear (SFM) and high-shear (FFM) are also reported (E; F, respectively). Scale bars: 5 mm. Flow direction for all panels is indicated by the arrow in panel A.

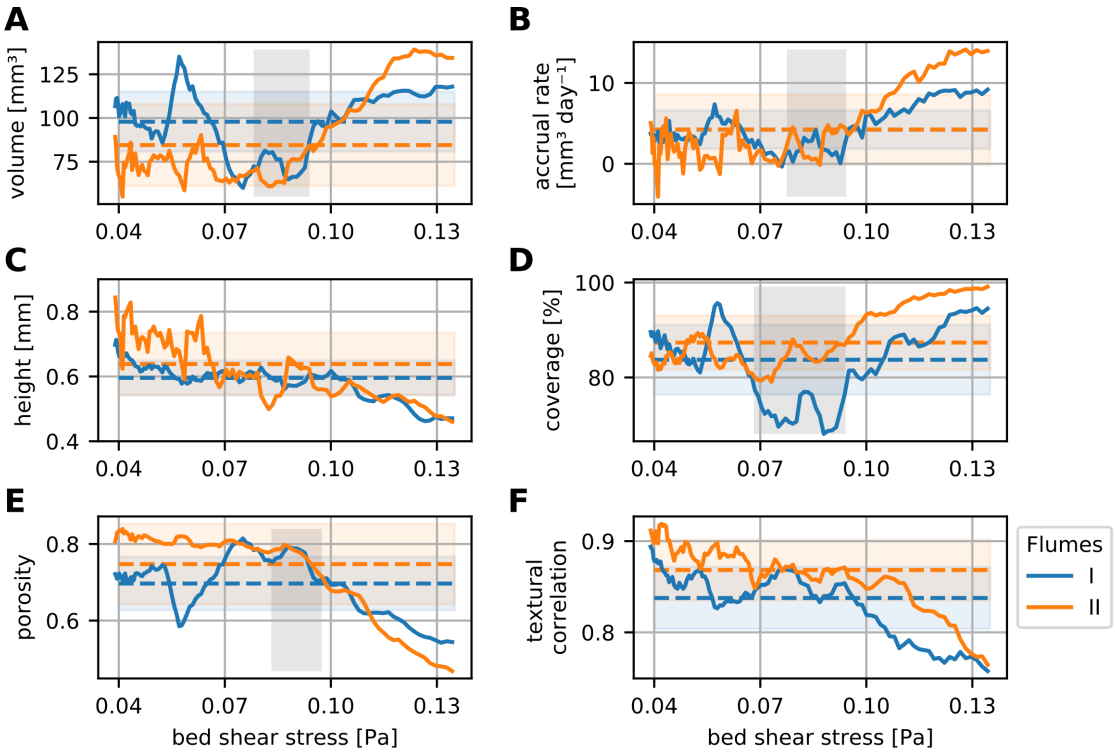

Figure 2.2 – **Key properties of phototrophic biofilms change along the hydraulic gradient.** Largescale OCT-derived DEMs were used to calculate moving window estimates (solid lines) of biofilm volume (A), accrual rate (B), height (or thickness) (C), coverage (D), porosity (E) and textural correlation (F) along the bed shear stress gradient (day 15; accrual rate was calculated between day 12 and day 15). Dashed lines and shaded areas depict overall averages and standard deviation, respectively. Grey bars indicate, when significant for both replicates, the range of changes in shear stress identified by breakpoint analysis (Supplemental Table 2.2).

Limited community turnover between the SFM and the FFM. To test the hypothesis that contrasting morphotypes emerged from differences in community compositions, we sequenced amplicons of the 18S and 16S rRNA genes from the SFM and FFM (day 15) to identify eukaryotic and prokaryotic community members, respectively (Supplemental Figure 2.9). Analysis of similarity (Anosim) based on Bray-Curtis similarities, showed no significant differences in community composition (16S rRNA: R = -0.15, p = 0.69; 18S rRNA: R = 0.11, p = 0.39) between the two morphotypes. The phototrophic community subset was dominated by Chlorophyceae, classified as *Scenedesmus* sp., contributing 36.6% to the reads in the 18S rRNA amplicon library, followed by *Mougeotia* sp. (Charophyta, 2.4 %) and *Achanthidium* sp. (Diatomea, 2.3%). The bacterial communities were dominated by *Luteolibacter* sp. (Verrucomicrobiae, 4.7%), *Flavobacterium* sp. (Bacteroidetes, 2.7%) and not-further classified Sphingomonadaceae (Alpha-Proteobacteria, 2.5%) and Rhodobacteraceae (Alpha-Proteobacteria, 2.5%). *Scenedesmus* sp. is a small (~10 μm in diameter) coenobial and biofilm-forming microalgae that form structurally homogenous biofilms under laminar flow [261]. However, in microbial communities developing under complex hydrodynamic conditions, microalgae may contribute to the formation of complex biofilm architectures [129]. Given its abundance, it is intuitive to assume that *Scenedesmus* sp. contributed to the here observed biofilm morphogenesis. Strikingly however, the same microalgal and bacterial communities were found in both SFM and FFM, reflecting their ability to form differing

biofilm morphologies. Our findings evoke architectural plasticity, rather than contrasting community composition, as the process underlying morphological differentiation in the phototrophic biofilms here under study. Architectural plasticity is understood as the remodelling of the biofilms tridimensional structure as an adaptive response to their environment [33]. It involves, for instance, ecological interactions, the generation of physiological heterogeneities and the differential expression of the extracellular matrix components [75;200].

Morphogenesis of the SFM and FFM.DEMs of the biofilm surface topology acquired at 3-day intervals (Figure 2.3) allowed us to address biofilm morphogenesis dynamics. Volume accumulation curves did not differ between SFM and FFM but accrual rates steadily increased over time in the FFM and reached higher values than in the SFM (Figure 2.4A). Terminal accrual rates (day 12 to day 15) reached 9 mm^3 day^{-1} and 14 mm^3 day^{-1} in the FFM and 3 mm^3 day^{-1} and 5 mm^3 day^{-1} in the SFM (see also Supplemental Table 2.1). The analysis of textural correlation showed that aggregation increased steeply at early time-points in the SFM, in contrast to the FFM, while biofilm maximum thickness was consistently higher in the SFM than the FFM at every time-point (Figure 2.4A). Hence, the divergence into morphotypes started early during biofilm growth (day 3) and the SFM, despite being consistently thicker than the FFM, had lower accrual rates in later time-points. In agreement with previous reports (*e.g.*, [105;157;235]), elevated flow velocities, in the range tested here, had a net positive effect on growth, outweighing the effect of shear-induced erosion and scouring. The presence of protruding biofilm clusters separated by empty areas can have important consequences for the local flow behavior, and related mass transport and drag force [49;168;229]. We compared the areal coverage of protruding clusters (*i.e.*, DEM areas at least two times larger than the local average) and the troughs (*i.e.*, DEM areas at least two times lower than the local average) between morphotypes (Figure 2.4B). The SFM was dominated by troughs (up to 73 %) and clusters (up to 11%), whereas the FFM was largely devoid of such cluster-trough sequences and characterized by a base biofilm (up to 74%). The SFM clusters increased in volume (up to 4 mm^3) but decreased in abundance over 15 days. They also exhibited an increasingly elongated aspect in the vertical direction, and a slight elongation in the flow direction (Figure 2.4C). As mentioned above, clusters-trough sequences can enhance the external mass transfer towards the biofilm base [49]. At the same time, exposed clusters are more susceptible to the drag forces [65;229]. Despite the limited temporal resolution of the acquired OCT time-series, we observed that the biofilm structures that were dynamic over time. The dynamic rearrangement of the biofilm structures was particularly evident from the subtraction of subsequent DEMs (Figure 2.4D, Supplemental Figure 2.10), in which the local biovolume accumulation and displacement appear as positive and negative pixel gray-level values, respectively. At later time points, entire SFM clusters occasionally sloughed off, while others were apparently pushed in the flow direction. Overall, the FFM appeared more stable in time despite the higher shear stress. Roughly around the shear stress breakpoint, we observed the formation of structures reminiscent of migratory ripples (Supplemental Figure 2.10; see also [225]). In the SFM, we found that up to 25 mm^3 of biovolume was displaced between day 12 and 15, accounting for 33% of the total biovolume (Figure 2.4D). Hence, although we cannot rigorously quantify biomass detachment and displacement, these qualitative observations support the notion that taller biofilm structures are more exposed to drag force than more homogeneous and self-sheltering structures (*e.g.*, [64;166;229;65;218]).

Figure 2.3 – **Biofilm morphogenesis over the course of the experiment.** The time-series of biofilm morphogenesis for the entire hydraulic gradient in flume II is displayed. Note the differences in scales. The arrow indicates flow direction. Scale-bars: 5 mm.

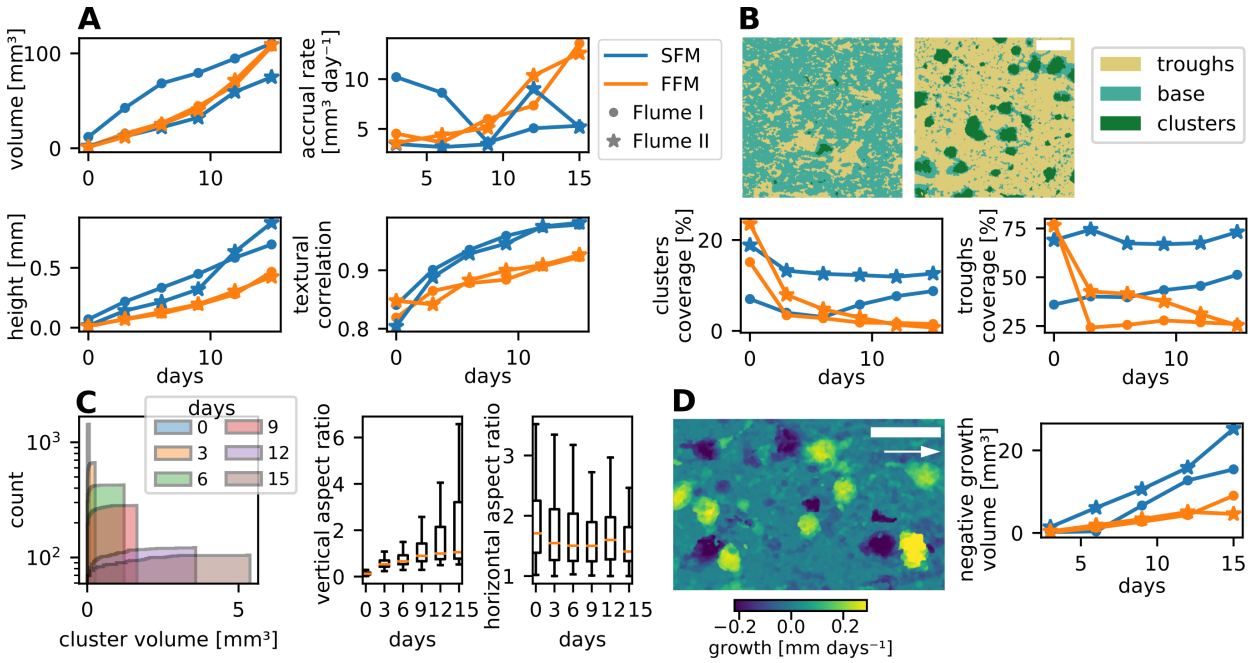

Figure 2.4 – **Biofilm morphogenesis differed across hydraulic conditions.** The temporal dynamics in biofilm volume, accrual rate, height and aggregation (textural correlation) for the SFM and FFM are shown in panel (A). A segmentation algorithm based on the difference from the local average thickness separated biofilm landscapes into base biofilm, protruding clusters and troughs (B). Shown are the temporal trends in the areal contribution of clusters and troughs. Cumulative histograms demonstrate the simultaneous increase in size and decrease in abundance of SFM clusters, while vertical and horizontal aspect ratios reveal their progressive elongation (C). Subtraction of subsequent DEMs (D, Supplemental Figure 2.10) can be interpreted as a spatially-explicit estimate of biofilm height variation. Areas with "negative growth" illustrated SFM clusters being detached from the substrate or displaced in flow direction (D). Total biofilm volume affected by "negative growth" increased over time and was higher in the SFM than in the FFM (D). The arrow indicates flow direction. Scale-bars: 5 mm.

Fluid flow within the SFM troughs provides solutes to the base of the biofilm. In order to assay the effects of surface topography on the local flow patterns, we used 3D numerical simulations to visualize the flow field around two idealized biofilm clusters with a width:height ratio similar to the SFM clusters. The simulated flow field revealed liquid flow into and within troughs between neighboring clusters and showed that fluid is advected into troughs predominantly via the vertical (u_z) and the lateral (u_y) components of velocity (Figure 2.5A). The simulated velocity field around two idealized biofilm clusters displayed downward and lateral fluid motions within the trough region between the clusters. Streamlines originating from upstream of the clusters entered the trough with velocities up to 10% of the mean flow velocity. Simulations further indicated that a fluid element entering the trough from the top recirculated in the trough region and reached the center of the region in approximately 1.5 minutes. Furthermore, we noted the formation of a vortex ring that could lead to enhanced fluid mixing in the trough region (Figure 2.5A). In line with previous models [168], these simulations suggest that advection within troughs is relevant for solute transport and replenishment, which may be further facilitated by the formation of vortices. Motivated by these simulations, we tested for the advective replenishment of oxygen within the biofilm troughs by measuring oxygen microprofiles across and around biofilm

clusters (in darkness). Microbial respiration is expected to reduce oxygen concentrations in stagnant zones where diffusion is the sole source of oxygen replenishment [49]. However, we found that dissolved oxygen concentration did not differ between the troughs and the bulk fluid (Figure 2.5B), supporting the notion of oxygen replenishment by multi-directional advective transport. We did not detect a diffusive boundary layer around the biofilm structures in both the SFM and the FFM (sensitivity ~50 μm; Figure 2.5B, Supplemental Figure 2.11). These results agree with other empirical observations and modeling predictions from earlier studies on heterogeneous biofilms [49;168;227]. However, the observation that the diffusive boundary layer around SFM clusters and troughs must be thin (< 50 μm) eliminates external mass transfer resistance as a driver of the formation of a rough, finger-like architecture [167]. In contrast, both the measured oxygen microprofiles and fluid dynamic simulation suggest that the transport of solutes from the troughs towards the clusters may sustain microbial activity and growth at the biofilm base.

Oxygen concentration profiles within biofilm architectures reveal chemical micro-niches. Chemical gradients figure among the emergent properties in biofilms that result from internal mass transfer resistance and potentially drive the small-scale diversification of biological processes with large-scale consequences [75;216]. For instance, limited mass transport within densely packed cells and their extracellular matrix can lead to nutrients deprivation in the deeper biofilm layers, potentially triggering sloughing [41;110;255]. To map the spatial distribution of oxygen inside the biofilm, we measured multiple oxygen profiles within the SFM (n = 35) and FFM (n = 27) structures (few representative profiles are reported in Figure 2.6A). Oxygen concentrations (in light, dark and the difference between light and dark) were more widely distributed in the SFM than in the FFM (robust Brown-Forsythe Levene-type test, p-value < 0.01) (Figure 2.6B, Supplemental Table 2.3). This corroborates the notion that structural heterogeneity, which is higher in SFM than FFM, leads to a heterogeneous distribution of chemical micro-niches in phototrophic biofilms. Under dark conditions, dissolved oxygen reached a lower concentration in the SFM (40 μmol l^{-1}) than in the FFM (178 μmol l^{-1}), while the opposite was the case under light (SFM: 353 μmol l^{-1}; FFM: 260 μmol l^{-1}). Also, when comparing measurements at the same biofilm depths, oxygen concentrations reached more extreme values in the SFM compared to the FFM (t-tests, p-values<0.01 for both light conditions and depths into the biofilm from 0.05 mm to 0.25 mm) (Figure 2.6C, Supplemental Table 2.4). These patterns are unlikely driven by differences in oxygen diffusivity, as biofilms grown under high shear are usually denser and less permeable to oxygen than their low-shear counterparts [22]. Hence, the gentler oxygen gradients within the FFM could be driven either by lower metabolic rates or advective oxygen transport inside the biofilm, but these processes cannot be disentangled in our experimental setup. Next, we mapped oxygen concentrations across individual SFM clusters in dark conditions (Supplemental Figure 2.12). We found that oxygen within SFM clusters was less depleted close to the cluster side walls compared to their inner cores (t-tests, p-values < 0.01 for depths ranging from 0.1 mm to 0.5 mm) (Figure 2.6D, Supplemental Table 2.5). This observation supports the notion that advective transport within troughs replenishes oxygen through SFM cluster walls. However, compared to the FFM, this effect only insufficiently supplies oxygen to the cores of SFM clusters, which were, compared to the FFM, more oxygen depleted in dark conditions (and more saturated when exposed to light). Given the low halfsaturation coefficient for dissolved oxygen for bacteria [100], it is unlikely that oxygen itself limited the metabolic activity of the biofilms under study. However, it is conceivable that other solutes, such as nutrients and metabolic waste products, will follow similar spatial dynamics and potentially induce stress responses in the cores and at the base of the SFM. Therefore, differential detachment induced by nutrients limitation remains a potential mechanism that could underly the formation of clusters separated by voids under low shear. We did not attempt to infer metabolic rates from the oxygen profiles because these could be compromised by advective transport

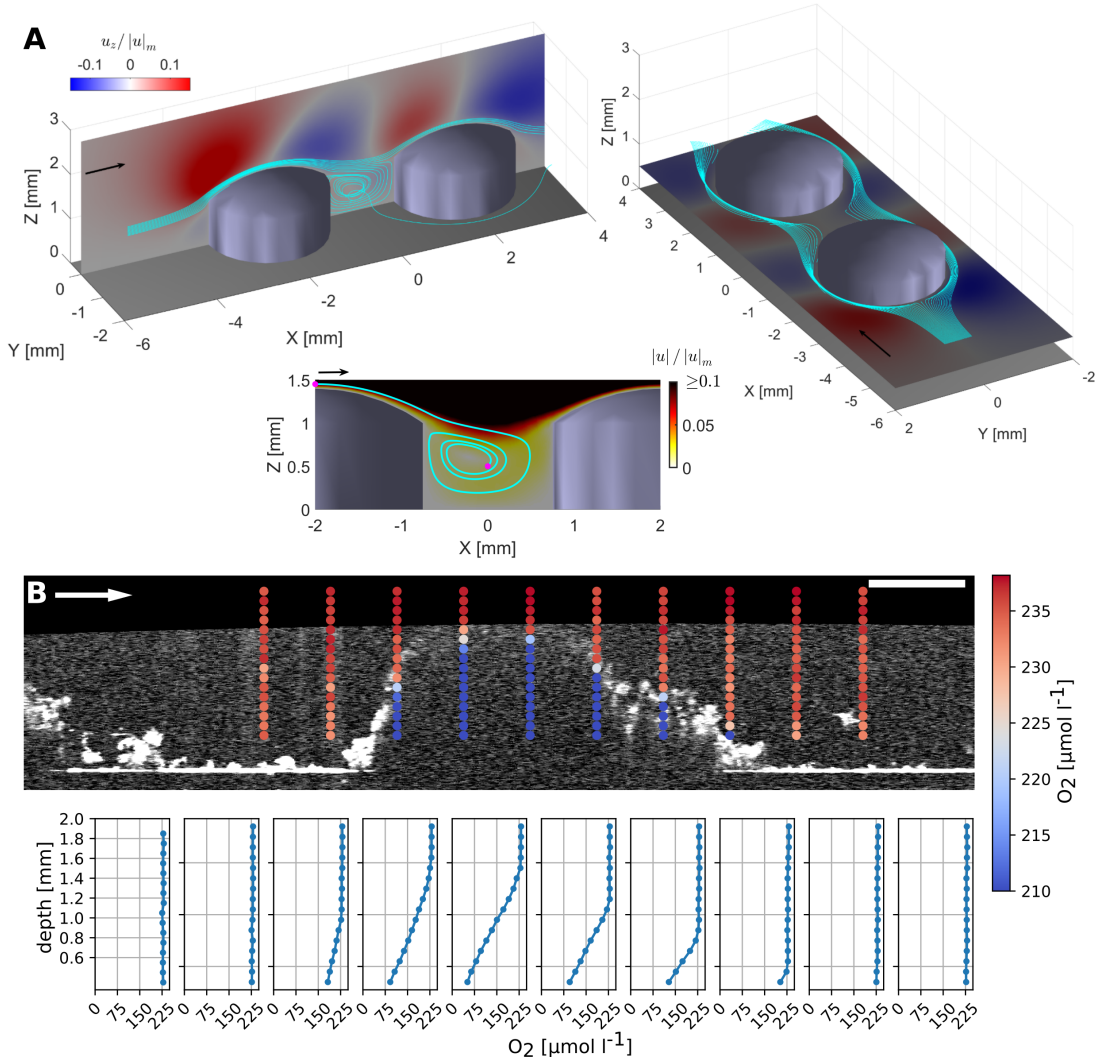

Figure 2.5 – **Numerical simulations and measured oxygen microprofiles suggest the presence of fluid flow around biofilm clusters.** Shown are the outcome of three-dimensional numerical simulations around two idealized biofilm clusters. Panel A provides the normalized vertical velocity and the lateral velocity components in the vertical symmetry plane (y = 0 mm) and a horizontal plane (z = 0.5 mm) superposed with selected streamlines. The lower subpanel shows the normalized velocity magnitude in the symmetry plane superposed with a streamline that demonstrates the fluid motion in the trough. Panel B shows representative oxygen measurements within and around a biofilm cluster (SFM) superimposed onto the respective OCT scan. Panel B illustrates oxygen microprofiles measured around and within biofilm clusters. Each point depicts the concentration of a single oxygen concentration measurement. Corresponding oxygen microprofiles are shown below. The arrow indicates the flow direction. Scale bar: 5 mm.

within the biofilm matrix. However, we calculated the ratio between the oxygen gradients (from 0.05 to 0.15 mm depth) in light and dark as a proxy for net autotrophic versus heterotrophic aerial oxygen fluxes. Light:dark ratios averaged around 1 and were not significantly different between the SFM and the FFM (Welch's test, p-value = 0.23, Supplemental Figure 2.13), which indicates a balance between net oxygen production and consumption in both morphotypes.

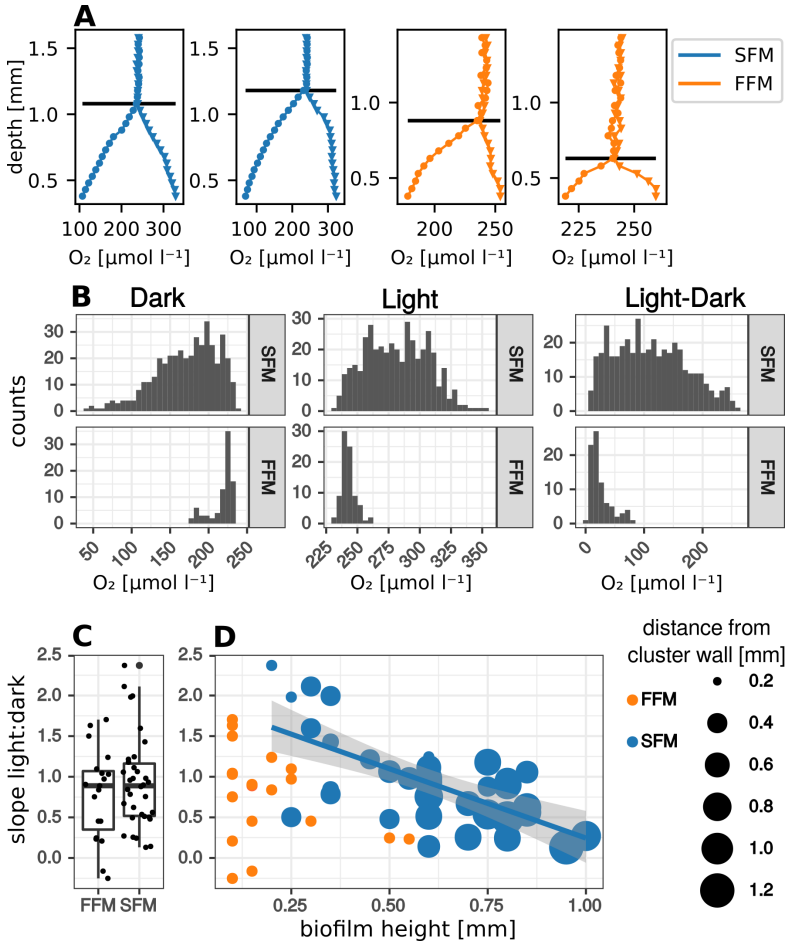

Figure 2.6 – **Oxygen microprofiling suggests a more heterogeneous distribution of chemical micro-niches in the SFM compared to the FFM.** Reported are representative oxygen microprofiles measured within SFM and FFM in light (triangles) and dark (circles) (A). Horizontal lines indicate the estimated position of the biofilm surface. Oxygen concentration and the difference in oxygen concentration between light and dark conditions were more heterogeneously distributed in the SFM than in the FFM (B). The distribution of oxygen concentration measured at the same biofilm depth (pooled in 100 μm steps) are compared between morphotypes (C) and at different distances from the SFM clusters walls (D, dark conditions).

Conclusions

Combining 3D imaging with sequencing, numerical simulations of fluid flow and oxygen microprofiling, we described architectural patterns in a complex phototrophic biofilm growing under a quasi-natural

flow conditions. Over a relatively short hydraulic gradient, we observed strikingly diverging biofilm architectures despite limited community turnover. Clusters separated by troughs developed under low shear stress, while a more homogeneous biofilm layer covered the substrate under high-shear. Streams are characterized by a remarkable heterogeneity in hydraulic conditions, both on short- and large-spatial range. Our results indicate that the architecture of benthic biofilms may plastically respond to the hydraulic conditions in their habitat, even in the absence of strong shifts in the community composition. Several experimental and modeling studies have previously investigated biofilms architectures under controlled laboratory conditions, providing numerous mechanistic hypotheses regarding their emergence. On one side, biofilm morphologies analogous to those observed here have been described across biofilm communities and spatial scales, and hence seem to be rather universal. On the other, our results confirm that the advective replenishment of oxygen within the biofilm troughs as well as the dynamic displacement and detachment of isolated clusters, may influence the morphogenesis of complex phototrophic biofilms in their natural environment. Our observations seem to exclude external mass transfer limitation as a driver of biofilm morphogenesis under the studied hydraulic conditions, whereas a combination of differential detachment induced by nutrients limitation and erosion of cells from the biofilm surface remains a viable explanation. We further observed an abrupt morphological transition around a threshold shear stress of ~0.08 Pa. Mechanical properties of the different architectures may lead to this threshold effect, however this remains to be addressed in future theoretical and empirical studies. Overall, our findings suggest that a tight coupling between architectural plasticity, chemical heterogeneity and mechanical resistance to shear affects the formation of the meso-scale patterns observed in biofilms that coat the benthic zones in streams and rivers.

Limitations of the Study

Following an approach often used in landscape ecology [36], we inferred the functional links between hydraulic conditions and biofilm morphogenesis from their spatial correlation. While this approach allowed us to study complex phototrophic communities at high resolution and under realistic hydraulic conditions, we cannot account for all potential effects. For instance, biomass may accumulate downstream, potentially oozing in the direction of the flow. This possibility seems unlikely, as shear and turbulence in the flume fast-flow region were strong enough to detach biomass that was just loosely adherent to the substrate, and did not permit the sedimentation of aggregates from the water column (visual observation). Furthermore, we started detecting a morphological shift between contrasting hydraulic conditions at early stages in biofilm development (3 days), when the accumulated biovolume was still remarkably low and no significant displacement of the biomass occurred yet. Nonetheless, the relationship between biofilm architecture and hydraulic conditions remains correlational and further experiments would be required to rigorously test any causal link. Working with complex communities and natural surface water as growth medium allows the formation of diverse biofilms relevant for stream ecosystems, but seasonal variation in inflow medium and seed community reduced the repeatability of the experiments. However, the communities that we sampled and the patterns that we observed are realistic and informative. The raw lake water used was filtered (nominal pore size 50 μm), but this removed just larger grazers and did not completely eliminate grazing pressure, which could have further modulated the morphology of the studied biofilms [29;248]. The flumes were constructed from plexiglass and this smooth substrate may have affected the observed dynamics to some extent. Nonetheless, the two biofilm morphotypes exhibited structural differences leading to diverging structural resistance, which are likely independent on the type of substrate colonized. OCT has a limited penetration depth within biofilms and imaging depth in water; as a consequence, structures taller than

~1.2 mm were not reliably imaged, which may have caused an underestimation of the total volume, accrual rate and biofilm thickness, particularly at later time-points and under slow flow.

Acknowledgements

We thank Antoine Wiedmer, Michel Teuscher, Laurent Morier and Pierre Loesch for constructing the experimental set-up, including the flumes and the OCT system. We acknowledge the precious contribution of Paraskevi Pramateftaki with DNA extraction and preparation of the sequencing samples. We thank Stelios Fodelianakis and Massimo Bourquin for the processing of the sequencing data. We thank Jan Wienold and Clotilde Pierson for the light intensity measurement. Comments by two anonymous reviewers greatly improved the manuscript. This work was funded by a grant (159958) from the Swiss National Science Foundation (SNSF) to TJB. ADB and PDA acknowledge the support of the FET-Open project NARCISO (ID: 828890).

Data and Code Availability

Raw OCT scans, processed DEMs and oxygen microprofile data have been deposited in Figshare. Raw sequences have been submitted to the European Nucleotide Archive (ENA) under accession number PRJEB39886. The code used for image acquisition, processing and analysis is available here.

Methods

Flume experiments. Water from Lake Geneva was continuously filtered (nominal pore size 50 μm, FA 10 SX 50 ATLAS FILTRI) into a 1 m^3 reservoir and from there pumped into open-channel flumes. A constant flow rate (2.22 10^{-4} m^3 s^{-1}) was supplied using valves equipped with flow meters. Water was recirculated in a large reservoir, in which the water level was kept constant with a continuous inflow from the lake (8.3 10^{-6} m^3 s^{-1}). The total water volume in the flume was 5.8 10-3 m^3, resulting in an average residence time of 26 s. Water temperature varied between 14.5°C and 15.5°C throughout the experiments, while pH oscillated between 7.16 and 7.55 (7.72 ± 0.30 [mean ± standard deviation]). Every 3 - 5 days, a water sample was filtered (0.22 μm polycarbonate filters, Isopore, Millipore) and analyzed by ion chromatography (Metrohm 930 Compact). Nitrate concentrations averaged 2.5 ± 0.4 mg l^{-1} and nitrite was below detection limit (< 0.05 mg l^{-1}). Further, total dissolved organic carbon (DOC) was quantified in filtered sample (pre-ashed GF/F, Whatman) using a TOC carbon analyzer (Sievers M9 TOC Analyser, GE). DOC varied between 872 and 3580 ppb, and averaged 1706 ± 731 ppb. Ammonia was quantified spectrophotometrically as described in [231], and averaged 4.7 ± 0.9 μg l^{-1}. Soluble reactive phosphorous was quantified using the methylene blue method and averaged 2.0 ± 1.3 μg l^{-1}. Light (13 W m^{-2}, JAZ spectrometer Ocean Optics) was provided for 12 hours per day using a combination of red and blue LEDs. The flumes were constructed from plexiglass with a funnel-like shape, imposing a gradient of flow velocity and bed shear stress on phototrophic biofilms. Flume width decreased gradually from 0.3 m to 0.05 m, with a slight curvature (Supplemental Figure 2.7). Average water depth was 0.022 m. The inflow was equipped with a round shaped adapter and a diffuser to minimize upstream turbulence. Prior to experiments, phototrophic biofilms growing continuously in the reservoir were harvested and disaggregated by shaking. The slurry was filtered using (41 μm nylon filter, Millipore) and diluted into 8 L of lake water. The biofilm slurry was then poured into the flumes and incubated for 12 hours without flow (under light). This seeding resulted in a thin layer of

base biofilm evenly covering the flume bottom. After seeding, the flow was started and biofilm was allowed to grow without disturbance for 15 days.

Hydraulic gradient characterization. Mean flow velocity (u) and Reynolds number (R) were estimated from the flume geometry, the water depth (0.022 m), and discharge (2.22 10^{-4} m^3 s^{-1}), as

$$u = \frac{Q}{h \times w}$$

$$R = \frac{Q}{v \times (2 \times h + w)}$$

where v is the kinematic viscosity of water, Q is the discharge, w is the flume's width and h is the water depth. The flow velocity within the open-channel flow chamber without biofilms was modeled using the geometrical design of the flume (Supplemental Figure 2.7). We used FLUENT (ANSYS R.19) to numerically solve a multiphase model (Volume of Fluid method), including 0.022 m water phase at the bottom of the flume, and a 0.018 m thick volume of air on top. We used the Reynolds-averaged Navier-Stokes approach, with a no slip-boundary condition on the plexiglass surface. An SST k-ω turbulence model [143], that is a two-equation eddy-viscosity model, was used to model turbulence. SST k-ω ensures simulation accuracy across the flow field by employing k-ω turbulence model in the regions near the wall and k-ϵ in other regions. The flow was generated by a pressure gradient between inlet and outlet. In order to resemble the flume flow field, boundary conditions were set similar to the flume operating conditions where the inlet discharge was 2.22 10^{-4} m^3 s^{-1}. The results of the simulation were used to estimate the velocity magnitude in every point, calculated as the sum of the x- y- and z- vector components of velocity. Bed shear stress was estimated as

$$\tau = \mu(\frac{\delta u}{\delta y})_{y=0}$$

where μ is the dynamic viscosity of water at 15°C.

OCT positioning and imaging. We used a spectral domain optical coherence tomograph (GANYMEDE, Thorlabs GmbH, Germany) centered at 930 nm and equipped with an immersion adapter. OCT datasets were acquired by averaging 3 A-scans and had a resolution of 40 μm in x and y and 2.18 μm in z direction, covering a volume of 10 mm × 10 mm × 2.23 mm. We mounted the OCT probe on a precision positioning device (STEPCRAFT, 30 μm precision in x,y), as described previously [55]. Automatic positioning and OCT scan acquisition allowed us to obtain 66 × 3 OCT scans in a mosaic pattern (overlap was set to 30% of the field of view). The final stitched OCT covered a total field of 0.040 × 0.0024 m. Further, higher resolution (11 μm x, y and 2.18 μm z) images in tiled patterns of 3 × 3 were taken at the two extremes of the velocity gradient. Biofilms were imaged every 3 days.

OCT scan processing and analysis. OCT scans were corrected for the lateral distortion using a custom made algorithm [55]. Then, OCT scans were binarized and the thickness of the biofilm at each position encoded in a digital elevation model (DEM). DEMs were cropped 50 μm above the plexiglass surface; this represents the minimum height of structures considered in this work. Shorter

structures were disregarded, in order to avoid fine irregularities of the plexiglass. Elevation maps were then stitched and denoised with a median filter. Biovolume was estimated as the volume beneath the biofilm surface, (*i.e.*, the sum of all pixels values in the DEM). This was supported by visual inspection of the OCT images, which did not reveal the presence of voids below the biofilm surface. Biofilm accrual rate over 3 days was calculated as the difference in biovolume between subsequent time-points, divided by the time lag (3 days). Biofilm maximum thickness was calculated as the 0.95 percentile of the height distribution; coverage was calculated as the percentage of the pixels within a DEM with values greater than zero. Biofilm solids hold-up was calculated as described by Picioreanu et al. [167], as the ratio between biofilm volume and the volume of a parallelepiped with a basal area equal to the substrate's surface area and height equal to the maximum biofilm height. Porosity was them calculated as 1 - biofilm solids hold-up. Textural correlation was calculated from the gray-level co-occurrence matrix [101] using the scikit-image package GLCM Texture Features, with distance = 200 μm and angle = 0°. Setting the distance parameter from 0 to 4000 μm and angles 0°, 90°, 180° did not qualitatively change the results. A square window of 0.024 m edge was moved along the stitched DEM in steps of 4 mm. For the fragmented regression analysis, we applied the Davies test to test for the presence of a breakpoint (function davies.test in R). Then, the position of the breakpoint and the slopes of the two contrasting trends were estimated using the 'segmented' R package using 0.11 Pa as a starting value [146]. The significance of the trend in biofilm architectural features with increasing shear was tested within the two fragments (or on the entire dataset when the Davies test did not evidence a significant breakpoint) using a modified version of the Mann Kendall test for autocorrelated data [99], using the R function mmkh (from the package 'modifiedmk'). Finally, in the absence of a significant breakpoint, the slope of the significant trends was estimated with a linear model. For these analyses, the dataset was reduced to include only non-overlapping windows and avoid excessive spatial autocorrelation. Linear regressions for the relationship between volume, height and coverage were also computed using R [178]. Image processing and analyses were done using Python, NumPy, scikit-image package when not stated otherwise. Jupyter notebook are available here. To analyze biofilm morphogenesis, we utilized higher resolution OCT scans (11.1 μm, 11.1 μm, 2.18 μm in x, y, z), which were processed analogously to the lower resolution counterparts. Volume, height, coverage and textural correlation were calculated as before. To segment troughs, clusters and valleys, we applied a gaussian filter with sigma 2.2 mm and selected areas that were 2 times taller than the filtered image as clusters, and 0.5 times lower as troughs. Segmentation parameters were chosen on the basis of a visual checks. The shape of individual clusters was analyzed using the regionprops function of the scikit-image package. Volume was calculated as the sum of pixels in the portion of the DEM containing the cluster of interest. The horizontal aspect ratio was calculated as the ratio between the major and minor axes of the ellipse that has the same normalized second central moment as the region basal area. Orientation represents the angle of the major axis with respect to the flow direction. The vertical aspect ratio was calculated as the ratio between cluster height and the square root of its basal area. Displaced volume and coverage were calculated by subtracting subsequent DEMs in the time series and selecting areas with negative values.

Fluid dynamics simulation around two idealized biofilm clusters. We simulate the tridimensional laminar stationary flow around two idealized biofilm clusters using Comsol Multiphysics 5.4. The computational domain represents a sub-region from our experiment, and it consists of a rectangular block with dimensions L_x = 16.5 mm, L_y = 7.5 mm and L_z = 4.5 mm. A right-handed co-ordinate system is centered at the center of the bottom surface. The idealized bio-film clusters are modeled as two impermeable rigid vertical structures each comprising of a circular cylinder (radius = 1.25 mm, height = 1 mm) capped with a truncated hemisphere of radius 2.15 mm. The two cylinders are symmetrically located on the bottom surface along the streamwise (x-axis) direction with center-center distance of 4

mm. We provide an inlet flow condition of uniform mass flux of 0.2 g s^{-1} chosen strategically based on experimental conditions. The boundary conditions are applied such that each boundary represents that of a sub-volume in the experimental field; no-slip on the bottom surface including the surface of each cluster, open-flow condition (with zero viscous stress) on the top surface, and periodic boundary conditions are applied on the two side surfaces. We use adaptive tetrahedral mesh with minimum element size of 8 microns near each rigid surface, such that the boundary layers are well resolved.

Microsensor measurements and microprofile analysis. Oxygen concentration microprofiles were measured with a fast-response Clark-type O_2 microsensor (tip diameter 10 μm, OX-10, Unisense A/S, Aarhus, Denmark), with steps of 50 μm. The microelectrode was calibrated in air-saturated water and anoxic sodium ascorbate solution. The microsensor was vertically mounted on a motorized micromanipulator (Unisense A/S) and connected to a microsensor multimeter (Unisense A/S). Data acquisition and micromanipulator positioning were controlled by a dedicated software (Sensor TracePro, Unisense A/S). The positioning the tip of the microsensor was monitored with an endoscope. Profiles were taken in light and dark, with a lag period of 1 hour after changing light condition, between 15 and 19 days of growth, only for flume II. Difference of oxygen concentration in the light and dark were calculated for each point and used as a measure of diel variability in oxygen micro-niches. The pooled oxygen concentration distributions (within the biofilm) under light, dark or their difference were significantly not normal (Shapiro test, p-value < 0.01 for each), and they differed significantly for the two morphotypes (Mann–Whitney test, p-value < 0.01 for each). We used the robust Brown-Forsythe Levene-type test from the lawstat R package, to test for differences in variance of FFM and SFM. We compared oxygen concentration distributions at comparable depth within the biofilm in the SFM and FFM, in both light conditions, using the unpaired samples t-test with uneven variances. For this analysis, measurement points were pooled in steps of 0.1 mm depth, to account for the uncertainty in the position of the biofilm surface. Distance from clump walls was calculated using the Euclidean distance transform function (from the scipy.ndimage package) applied to the binarized DEM. The ratio of the oxygen gradient below the biofilm surface (between 0.05 mm and 0.2 mm) in light and dark (for each profile) was used as an estimate of the relative contribution of photosynthesis and respiration to the net oxygen flux in that point. Also in this case, we used a Welch's two-samples t-test to test for differences between the SFM and FFM.

DNA extraction, sequencing and bioinformatics. We sampled biofilms at the two extremes of the morphological gradient using sterile swabs. Samples were flash frozen at - 80°C and subsequently DNA was isolated using the DNeasy Power Soil kit (QIAGEN). The 16S and 18S rRNA genes were amplified using PCR with the 341f (5'CCTACGGGNGGCWGCAG-3') and 785r (5'-GACTACHVGGGTATCTAAKCC-3'; Klindworth et al., 2012) and TAReuk454FWD1 (5'-TCGTCGGCAGCGTCAGATGTGTATAAGAGACAG-3') and TAReukREV3 (5'- GTCTCGTGGGCTCGGAGATGTGTATAAGAGACA-3';[217]) primer pairs, for prokaryotic and eukaryotic community members, respectively. Sequencing libraries were prepared using the Nextera XT kit (Illumina), equimolar pooled and sequenced on a 300 bp paired-end MiSeq (Illumina) run at the Lausanne Genomic Technology Facility (LGTF). Sequencing adapters were clipped from the raw reads which were subsequently denoised and clustered into Amplicon Sequence Variants (ASV) using dada2 (vers. 1.14) [37] as implemented in qiime2 [30]. After taxonomic assignment, autotrophic community members were extracted from the 18S dataset. Analysis of similarity (anosim) was performed on Bray-Curtis distance matrices using the R package vegan [154].

Supplemental Figures and Tables

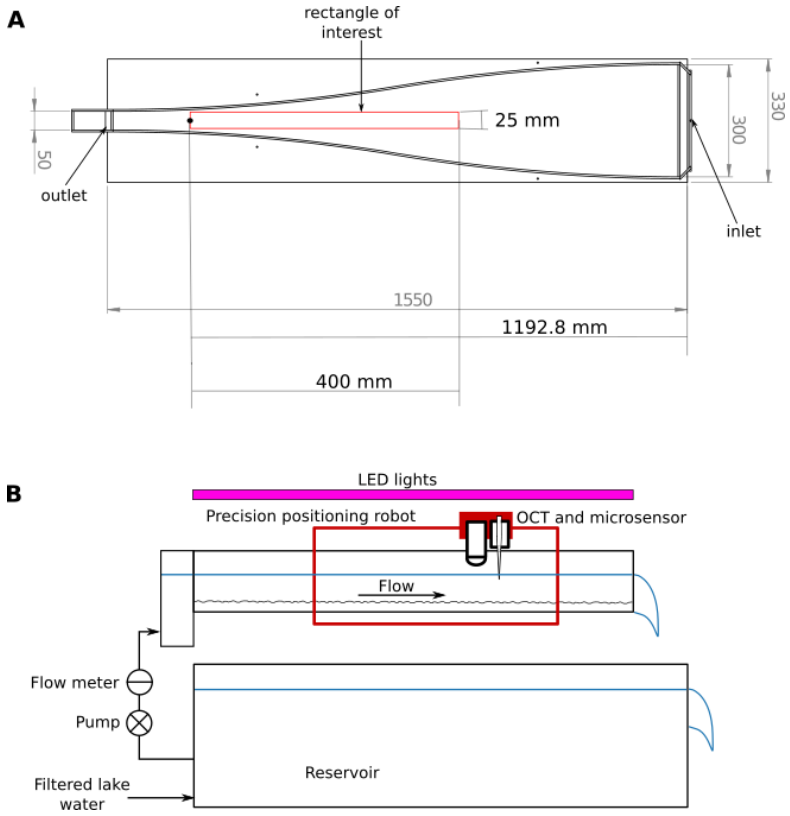

Figure 2.7 – Plexiglass flumes were designed with the represented geometry to obtain a flow velocity gradient, increasing in the direction of the flow. The "rectangle of interest" indicates the position of the biofilm characterized in this study. The flumes had a total depth of 50 mm, while the depth of the water was ~22 mm (A). Filtered lake water was continuously pumped into a large reservoir, from which it was pumped into the flume. The flow rate was controlled with a flow meter. The water was fully recirculated into the reservoir. Light was provided with LED lights, while the OCT probe and the microsensor were mounted on a robot that allowed to precisely control their positioning (B).

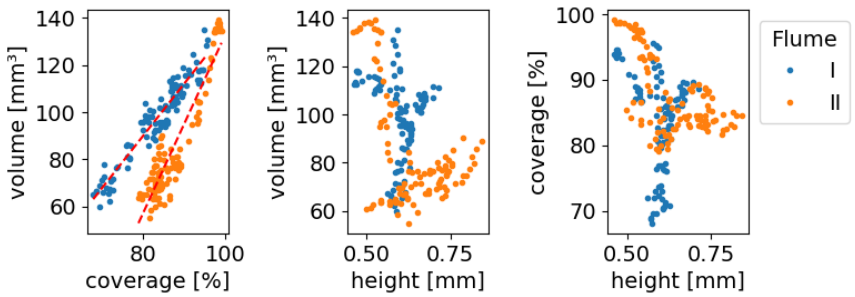

Figure 2.8 – Biovolume is correlated to surface coverage rather than to biofilm height. We found a significant positive correlation between the volume accumulated in a square moving window (24 mm edge length) along the hydraulic gradient (flume II is showed in Figure 2.1) and total coverage in the same window (lm, slope$_I$ = 2.23; slope$_{II}$ = 3.82; R^2_I = 0.96, R^2_{II} = 0.93; p-value < 0.01 for both). In contrast, maximum height of the biofilm, calculated as the 0.99 percentile of the height distribution, was found to have a negative and non-linear relationship with accumulated volume.

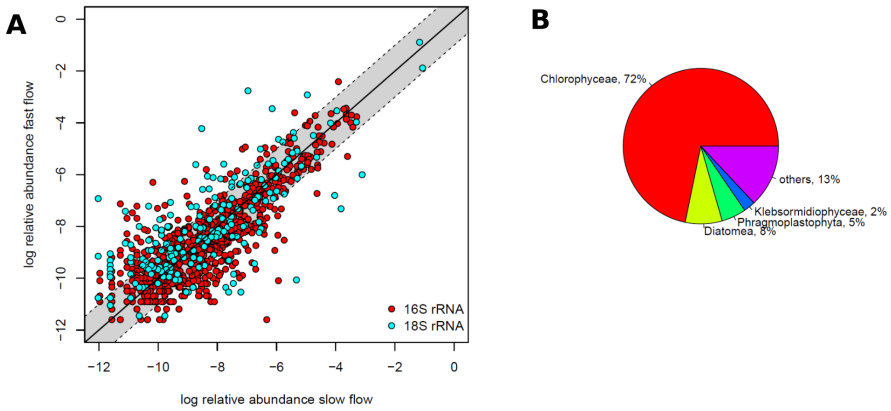

Figure 2.9 – Phototrophic community composition in experimental biofilms. (A) Community composition did not differ between SFM and FFM morphotypes. Shown are average relative abundance (log) for 16S rRNA and 18S rRNA sequence variants for biofilms sampled from slow and fast flow areas. Only sequence variants that occurred in both morphotypes are shown (n16S = 779, cumulative relative abundance: 96.9% of the entire 16S rRNA dataset; n18S = 390, cumulative relative abundance of the entire 18S rRNA dataset: 98.3%). The 1:1 line (solid line) and the grey shaded area denoting ± 1 log units from the 1:1 line are shown for guidance. (B) Visual and microscopic inspection showed that biofilm biomass was dominated by phototrophic microorganisms. Refining the 18S rRNA gene dataset to include taxonomically resolved Archaeplastida, Stramopiles, Alveolates and Rhizaria (the three latter being combined to the supergroup SAR), we retained 173 sequence variants. Together, they represented 53.3% of relative read counts for the 18S rRNA dataset, with Ophistokonta and Amoebozoa representing another 44.8%. The phototrophic communities included 18 taxonomically resolved classes, which were dominated by Chlorophyceae (71.7% relative read counts), Diatomea (7.7%), and Zygnematophyceae (5.1%). Chlorophyceae included 13 distinct 18S rRNA sequence variants, however, across all samples, they were dominated by a single ASV (contributing to 95% of reads classified as Chlorophyceae). A blast search of this sequence resulted in hits to *Scencedesmus* sp. (blastn against nr/nt database, max score 695, E-value < 1e-179). *Scenedesmus* is a common, colony-forming (4 - 30 elongated cells laterally joined), non-motile and high-ligth adapted freshwater green algae (Chlorococcales), often found in stream biofilms (*e.g.* [173;207], and can pioneer biofilm succession [195]. The phototrophic biofilms were further composed of diverse Diatomea predominantely classified as Bacillariophytina (with 12 sequence variants and 5.2 out of 7.7% overall contribution of Diatomea to phototrophic community read counts) and Fragilariales (6 sequence variants and 2.4% out of 7.7% contribution). Both Bacillariophytina and Fragilariales are common in stream and river biofilms, where they often dominate carbon fixation [35]. Commonly described as diatoms, these taxa often assume a benthic livestyle in flowing waters, facilitated by fibrillar attachment structures [244] and the production of extracellular polymeric substances (EPS) which are released from the apical field of pennate diatoms. *Mougeotia* sp. (Phragmoplastophyta, Zygnematophyceae) is a cosmopolitan mat-forming freshwater algae and may occur in later stages of biofilm formation [213]. Taken together, our experimental biofilms were composed of a diverse assemblage of common freshwater biofilm forming taxa, such as found in many streams and rivers.

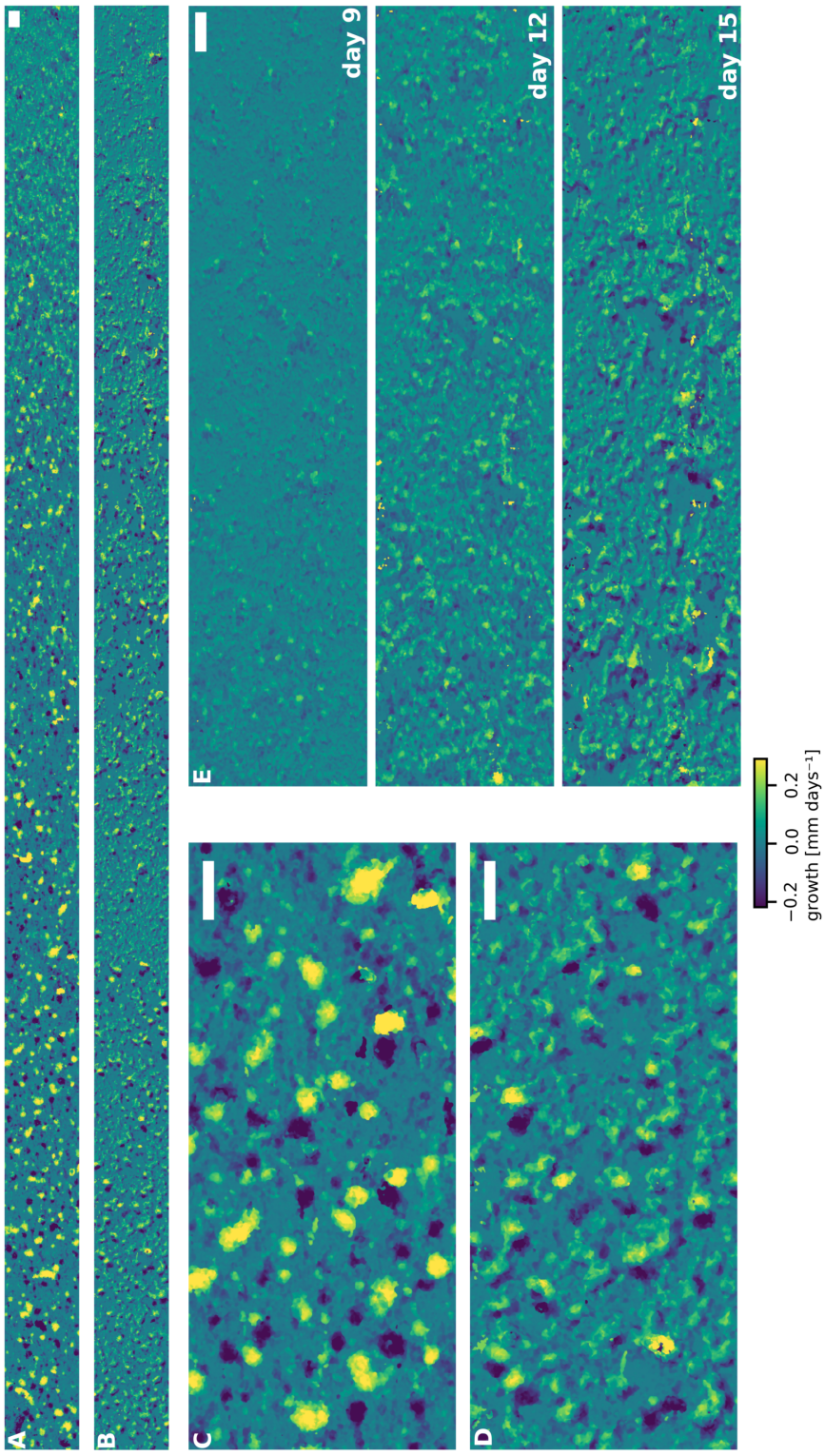

Figure 2.10 – The OCT derived DEMs obtained at subsequent time points were subtracted to obtain the rate of increase in biofilm height per day. Panels A and C refer to flume II between day 12 and 15, while B and D to flume I between the same time-points. We attribute areas with negative accrual rates to displacement of biofilm clusters. Panel E shows the progressive enlargement of empty areas in the flow direction and the formation of structures resembling migratory ripples at the transition between the two morphotypes (time points are indicated). Scale-bars: 5 mm.

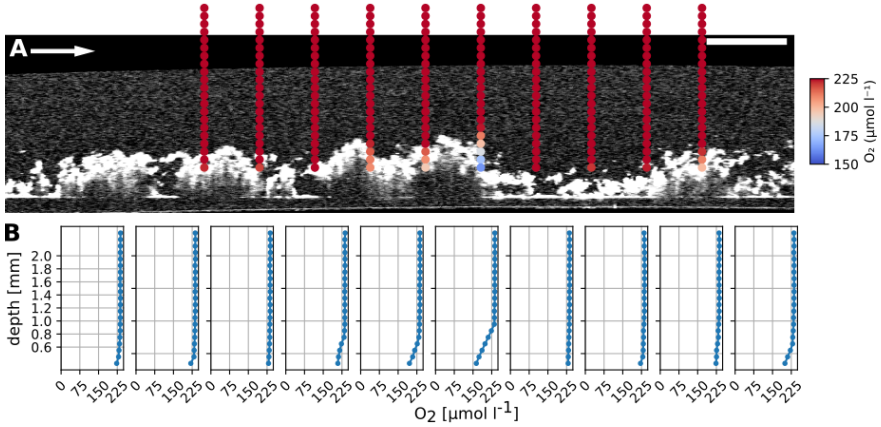

Figure 2.11 – Shown are representative oxygen measurements within and around a biofilm structure (FFM) superimposed onto the respective OCT scan. Each point depicts the concentration of a single oxygen measurement in darkness (scale bar: 5 mm, arrow indicates the flow direction). The corresponding oxygen microprofiles are shown below. Note the absence of a diffusive boundary layer.

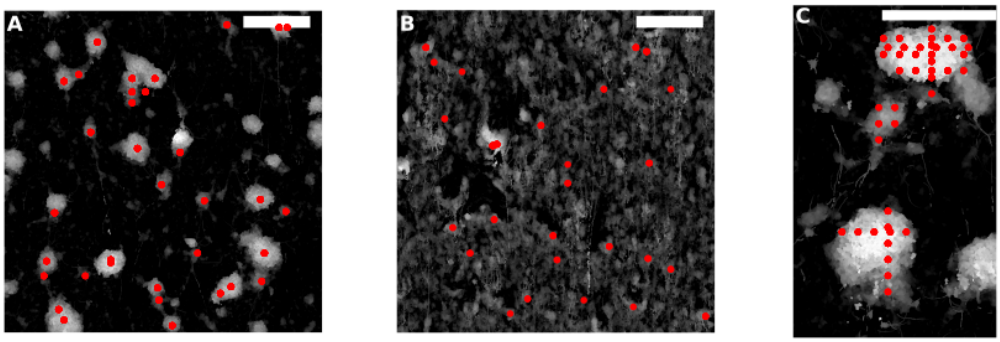

Figure 2.12 – Positions of the measured profiles. To assess the spatial heterogeneity of the concentration of oxygen, we measured 35 and 27 oxygen profiles in both light and dark, for the slow flow morphotype (SFM) (A) and fast-flow morphotype (FFM) respectively (B). The locations of these profiles are indicated by the red dots. Further, we obtained 24 oxygen profiles in different positions within two clumps of the SFM, in dark conditions (C). Scale-bars are 5 mm.

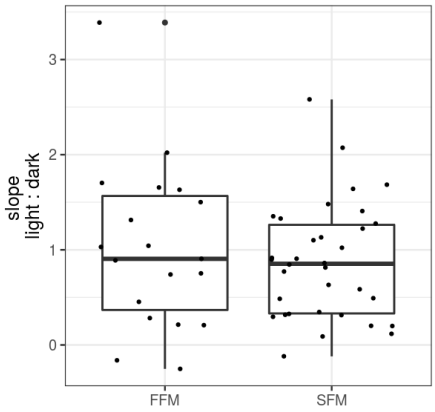

Figure 2.13 – The ratio of the slope of the oxygen gradient below the biofilm surface (between 0.05 and 0.15 mm within the biofilm, light:dark) indicated a balance between heterotrophic and autotrophic aerial oxygen flux in SFM and FFM.

Table 2.1 – Morphological features of SFM and FFM at the two extremes of the flow velocity gradient after 15 days of growth. The reported accrual rates refer to the time interval between day 12 and day 15.

	hydraulic conditions			**morphologicl features**					
	flume	**flow velocity [m s^{-1}]**	**bed shear stress [Pa]**	**volume [mm^3]**	**accrual rate [mm^3 day^{-1}]**	**height [mm]**	**coverage [%]**	**porosity**	**textural correlation**
SFM	I	0.059	0.04	107	3.73	0.7	90	0.72	0.89
	II	0.059	0.04	89	5.04	0.84	85	0.81	0.91
FFM	I	0.135	0.13	118	9.18	0.47	95	0.54	0.76
	II	0.135	0.13	134	13.96	0.46	99	0.47	0.76

Table 2.2 – Breakpoint analysis of the morphological gradient. We tested for the presence of a breakpoint, separating two regions of the morphological gradient with contrasting relationship with shear stress, using the Davies' test for a non-zero difference-in-slope parameter of the segmented regression. The bed-shear stress breakpoint, standard error (SE) estimates and p-values are reported as well as the adjusted R^2 of the segmented regression. When the Davies' test was not significant, the adjusted R^2 of a linear model is reported. The statistical significance of trends below and above the breakpoint shear stress (SFM and FFM shear respectively), was tested with the modified version of the Mann-Kendall test for autocorrelated series. Significant trends were evaluated with a linear model, whose slope are reported (units of the variable * Pa^{-1}). When no significant breakpoint was observed, the Mann-Kendall test was performed on the entire data set.

		Davies' test				**Mann-Kendall test**				**linear model**
						SFM		**FFM**		
	flume	breakpoint shear [Pa]	SE	p-value	adj. R^2	Z	corr. p-value	Z	corr. p-value	slope
volume [mm^3]	I	0.085	0.003	<0.05	0.5	-1.85	0.06	2.63	<0.01	1108
	II	0.084	0.002	<0.01	0.92	-0.62	0.53	3	<0.01	1661
accrual rate [mm^3 day^{-1}]	I	0.089	0.006	<0.01	0.78	-1.16	0.24	2.63	<0.01	190.5
	II	0.083	0.006	<0.05	0.89	-0.62	0.53	3	<0.01	281.9
height [mm]	I	-	-	0.19	0.78	-3.3	<0.01	-	-	-1.69
	II	-	-	0.26	0.76	-4.2	<0.01	-	-	-3.02
coverage [%]	I	0.087	0.002	<0.01	0.67	-2.26	0.02	2.63	<0.01	568
	II	0.073	0.002	<0.01	0.86	-0.72	0.47	3.34	<0.01	314
porosity	I	0.089	0.002	<0.01	0.68	1.44	0.15	-2.63	<0.01	-5.7
	II	0.089	0.001	<0.01	0.99	-2.81	<0.01	-2.63	<0.01	-7.5
textural correlation	I	-	-	0.1	0.75	-2.98	<0.01	-	-	-1.07
	II	0.111	0.002	<0.01	0.92	-12.83	<0.01	-1.04	0.3	-0.76

Table 2.3 – Statistics of the distribution of the dissolved oxygen concentration in the slow- and fast-flow morphotypes (SFM and FFM). We obtained several profiles of dissolved oxygen concentrations in different locations within the SFM and FFM, under light and dark conditions (flume II). The features of the distribution of oxygen concentrations (points from all profiles were pooled) are reported.

		FFM	**SFM**
	number of profiles	27	35
	number of points	84	406
dark [μmol O^2 l^{-1}]	0.1 quantile	189.9	115.9
	0.9 quantile	230.9	219.2
	maximum	235.1	238.1
	mean	218.1	170.8
	median	224.2	177.1
	minimum	177.9	40.2
light [μmol O^2 l^{-1}]	0.1 quantile	237	250.9
	0.9 quantile	250.7	313.6
	maximum	259.8	352.9
	mean	242.6	282.6
	median	241.8	282.8
	minimum	230.9	232.5

Table 2.4 – T-test for unpaired samples with uneven variances to test for differences in oxygen concentration at different depth within the biofilm among profiles taken within the SFM and FFM in light and darkness, respectively. Measurements were pooled in 0.1 mm steps.

depth within biofilm [mm]	**dark p-value**	**light p-value**	$\mathbf{n}_{SFM}$	$\mathbf{n}_{FFM}$
0.05	0.027	<0.01	24	24
0.05-0.15	<0.01	<0.01	58	24
0.15-0.25	<0.01	<0.01	86	23
0.25-0.35	0.047	<0.01	32	4
0.35-0.45	<0.01	<0.01	74	5
0.45-0.55	<0.01	<0.01	39	3

Table 2.5 – T-test for unpaired samples with uneven variances to test for differences in oxygen concentration at different depths within the biofilm among profiles taken within the SFM clusters in the dark. Measurements were pooled in 0.1 mm steps.

depth within biofilm [mm]	**p-value**	$\mathbf{n}_{dist[0.05-0.2]}$	$\mathbf{n}_{dist[0.2-1]}$
0.05	0.22	6	14
0.05-0.15	0.03	9	33
0.15-0.25	<0.01	9	33
0.25-0.35	<0.01	7	32
0.35-0.45	<0.01	6	30
0.45-0.55	<0.01	5	29

3 Biophysical properties at patch scale shape the metabolism of biofilm landscapes

Research article in preparation

Authors: **Anna Depetris**[1], **Giorgia Tagliavini**[2], **Hannes Peter**[1], **Michael Kühl**[3], **Markus Holzner**[2], **Tom Battin**[1]

[1]Stream Biofilm and Ecosystem Research Laboratory, School of Architecture, Civil and Environmental Engineering, Ecole Polytechnique Fédérale de Lausanne
[2]Environmental Fluid Mechanics Group, Institute of Environmental Engineering, ETH Zürich
[3]Marine Biological Section, Department of Biology, University of Copenhagen

AD, TJB and HP designed the experiments; AD conducted the experiment with the support of HP; AD and HP analyzed the data; GT performed the computational simulations of fluid dynamics and O_2 transport; MH advised on the fluid dynamics simulations and data analyses; MK advised on microsensor measurements and data analyses; all authors contributed to writing the paper.

Introduction

Biofilms are surface-attached and matrix-enclosed communities that dominate the microbial world in most natural ecosystems [77] and that are of utmost relevance to public health [98;46]. Biofilms are now increasingly recognized as microbial landscapes as an integrated part of the landscape that they inhabit. This notion has enabled aquatic microbial ecologists [12] and more recently also microbiologists studying the human microbiome [175] to apply theory of landscape ecology to the microbial realm. A basic tenet of landscape ecology is that the features and spatial arrangement of the landscape reciprocally interact with ecosystem functions [236;250]. A prominent feature of landscapes are patches, discrete physical and biological patterns that may interact to affect higher-order processes, such as mass flux, dispersal and diversity [170;250].
Streams are hierarchically organized ecosystems with nested levels of heterogeneity, ranging from

the networks that stream channels form at landscape level to the streambed landscape [156;252]. At the level of the phototrophic biofilms that coat the streambed, microbial landscapes emerge with complex topographies and communities [7;54]. These biofilms drive critical ecosystem processes, including primary production and respiration, and form the basis of the food chain [7]. The spatial heterogeneity of the streambed modulates processes driven by biofilms, including the removal of nutrients [40] and organic compounds [210] from the streamwater, biofilm growth [67] and both benthic primary production and respiration [39]. Despite the inherent links between patchiness and landscape functioning [170;250;236;136], the existence of patches and their functional relevance for biofilm landscapes remains elusive to date. This is certainly attributable to the length scales (multi-micrometre) typically used in biofilm research, which is below the length scale (multi-millimeter) at which patchiness emerges [243]. Establishing such links is critical to improve our understanding of the success of biofilms and their relevance for ecosystem functioning.

The structure-function coupling of biofilms is modulated by the fluid flow around them [216;215;10]. Related mass transfer can result in the establishment of chemical gradients and diversification of niches [76], which can be further increased by light gradients in phototrophic biofilms. Mass transfer can also control the differential uptake of organic compounds that vary in bioavailability (*e.g.*, [10;210;209]), even with consequences for community metabolism in streams [39]. Turbulent flow can induce local biofilm erosion and, at the same time, it can enhance solute transport to biofilms by eroding the diffusive boundary layer (*e.g.*, [49;215]). Fluid motion can replenish solutes in the channels surrounding biofilm clusters [49;219]. The common wisdom is that solute transport inside biofilm clusters is governed by diffusion owing to their overall low permeability [61;141;215]. However, within permeable biofilms under a sufficient pressure gradient, advection can foster transport locally [53;165]. Along this line, it was suggested that, despite their disparate scale, the coupling of structure and function in biofilms is analogous to that in the streambed that the biofilm inhabit [7]. Currently, we do not understand how mass transfer changes across possible patches within a biofilm and how this may affect its metabolism as a whole.

Benthic biofilms in streams are highly diverse and include representatives from all three domains of life [7]. At the sub-meter scale of streambed patches (*e.g.*, bedforms), community composition is partially driven by the local hydraulics [19;192].

We do not yet have an understanding of the organization of the microbial diversity beyond that scale — or of its organization into patches within the biofilm landscape. This is potentially relevant to infer ecological mechanisms underlying the massive biodiversity with hundreds if not thousands of microbial taxa colonizing the surface of a single pebble on the streambed. In this study, we sought to answer how patches in phototrophic biofilms translate into distinct physical structures, specific microbial assemblages and metabolism, and how the various patches contribute to the metabolism of the biofilm landscape. To address these questions, we studied phototrophic biofilms grown under two different hydraulic environments and combined amplicon sequencing with high spatial resolution O_2 micro-profiling guided by optical coherence tomography (OCT). We complemented this empirical approach with two-dimensional numerical simulations of flow velocity and O_2 concentration fields around and within biofilm patches to assess mass transfer within and compare the metabolic rates of the different patches. We found that, despite their close spatial proximity, the different patches were composed of distinct algal and bacterial assemblages, however, without major differences between the two hydraulic environments. Our results indicate that advective transport, around and within biofilms, was unexpectedly pronounced and influenced both O_2 concentration gradients and the metabolism of the individual patches. Furthermore, we observed upwelling and downwelling regions in various biofilm patches, reminiscent of hydrodynamic exchange through the streambed. Our results further indicate that the metabolism of the entire biofilm landscape is shaped by the relative contribution of

patches. We demonstrate how small-scale biodiversity patterns and structure-function coupling affect higher-order biofilm functioning, with possible impacts for stream ecosystem metabolism.

Results and Discussion

We grew phototrophic biofilms from raw surface water in a flume designed to reproduce a gradient of turbulent conditions relevant for streams (Methods). After one month, mature biofilms consisted of a base layer that continuously carpeted the flume bottom (Figure 3.1); this basis was dominated by cyanobacteria (henceforth referred to as cyanobacteria-dominated basis, CDB). Distinct patches abundantly emerged from the CSB. Conspicuous among them were fluffy tufts (up to 1.5 mm in height) dominated by green algae (Klebsormidiophyciae) and henceforth referred to as Klebsormidiophyciae-dominated patches (KDP). These latter consistenly emerged interspersed with diatom-dominated patches (DDP) with in the biofilm landscape (Figure 3.1, Figure 3.2). Given the pivotal role of hydraulics for biofilm structure and function [10;215;234], we here focused on biofilms growing under two contrasting hydraulic microenvironments within the flume. One was characterized by elevated bulk flow velocity (0.13 m s^{-1}) and turbulent kinetic energy (7 x 10^{-4} m^2 s^{-2}), the other by low flow velocity (0.06 m s^{-1}) and turbulent kinetic energy (2 x 10^{-4} m^2 s^{-2})(Methods, see also Figure 3.9).

Patches and community turnover in microbial landscapes. Community composition and diversity of biofilms have been studied across spatial scales, ranging from entire stream networks [21] to the patch of a streambed [19;192]. To study the biodiversity dynamics at the scale of biofilm landscapes, we sampled CDB, DDP and KDP from both hydraulic microenvironments. Using 16S rRNA and 18S rRNA sequencing (Methods), we found a consistent community turnover among the all three components (Figure 3.3A). The CDB communities were dominated by cyanobacteria, predominantly members of the Pseudanabaenales, Synechococcales and Stigonematales orders and a not further classified Chlorophyceae. The DDP community was dominated by *Achnanthidium saprophilum*, and the KDP community by a not further classified filamentous algae of the Klebsormidiophyceae clade. Besides these major phototrophs that did not differ between both flow environments, CDB, DDP and KPD were each associated with diverse eukaryotic and prokaryotic communities. For instance, between 36 and 46 distinct eukaryotic community members were detected in the CDB, KDP and DDP, respectively. Heterotrophic prokaryotic biofilm community members were more diverse, with between 140 and 281 amplicon sequence variants (ASVs) present in the different biofilm components. Generally, the prokaryotic assemblages were specific to CDB, DDP and KPD (Figure 3.3B), with Bray-Curtis similarities among replicates of the same patch type averaging 0.62 ± 0.10, while similarity across different patch types averaged 0.48 ± 0.11. Differences in abundance-based community similarity across samples can arise from the replacement of individuals of some taxa by individuals of other taxa (*i.e.*, balanced variation in abundance) or through abundance gradients, in which abundance changes between samples without taxa substitution. Partitioning Bray-Curtis similarities into these two components, we found that balanced variation in abundance dominated among replicate-dissimilarity, accounting on average for 59.3 ± 10.8 and 62.1 ± 9.1% of community turnover in CDB and DDP, whereas this process accounted on average for 91.4 ± 7.4% of the turnover observed among replicates in KDP. Differences in Bray-Curtis similarity across patch types were also predominantly (82.0 ± 26.6%) attributed to balanced variation in abundance. Taken together, these results highlight that all three harbour distinct and specific communities with the substitution of taxa being the dominant driver of compositional turnover. Non-metric multidimensional scaling (NMDS) ordination combined with procrustes superimposition revealed an overlap between the CDB and DDP community compositions, while both differed from

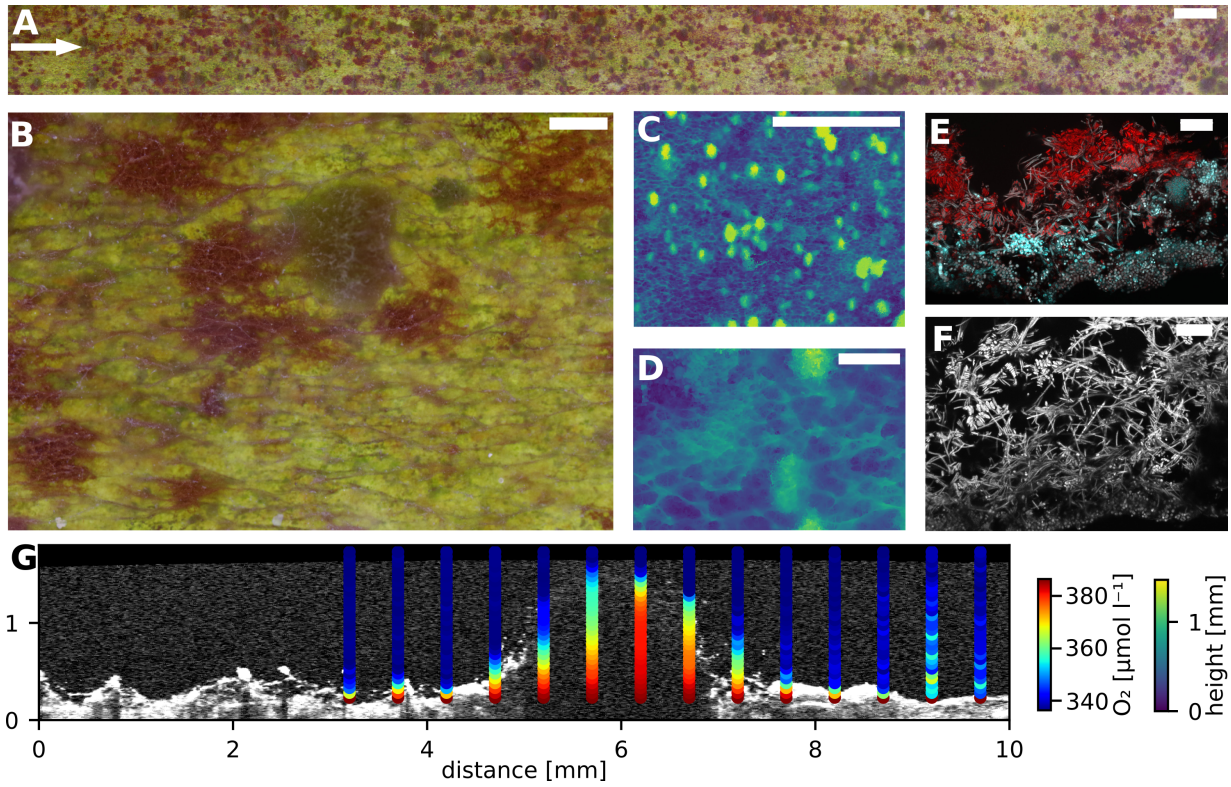

Figure 3.1 – **Characterization of a patchy phototrophic biofilm.** A phototrophic biofilm was grown from a natural inoculum by running raw lake water in an open-channel plexiglass flume. The flume design imparted a turbulent regime and a gradient of hydraulic conditions with flow velocity and turbulent kinetic energy decreasing in the flow direction (mean flow velocity: 0.13 m s^{-1} to 0.06 m s^{-1}; TKE: 7 x 10^{-4} m^2 s^{-2} to 2 x 10^{-4} m^2 s^{-2}). We obtained a mosaic of macro-photographs (A; B) and OCT scans of the patchy biofilm that developed after one month. The OCT scans were processed to obtain a digital elevation model of the biofilm surface topology (C; D, color bar is shown in G). Scale-bars: 20 mm (A; C) and 2 mm (B; D). respectively. A confocal laser scanning micrograph of a diatoms-dominated patch (DDP) and cyanobacteria-dominated base biofilm (CDB) under fast flow are shown (E and F respectively). Red and cyan in E indicate chlorophyll a and phycocyanin autofluorescence, respectively; greys in F indicate chlorophyll a autofluorescence (Methods). Scale-bars: 50 μm. Transects of O_2 concentration profiles were obtained across selected biofilm structures by coupling of O_2 microsensors and OCT (Methods), in both light conditions. A sample OCT B-scan aligned with the corresponding O_2 concentration measurements (illuminated conditions) over a KDP is reported (G, see also Figure 3.13). The arrow indicates the flow direction for panels A, B, C, D, and G.

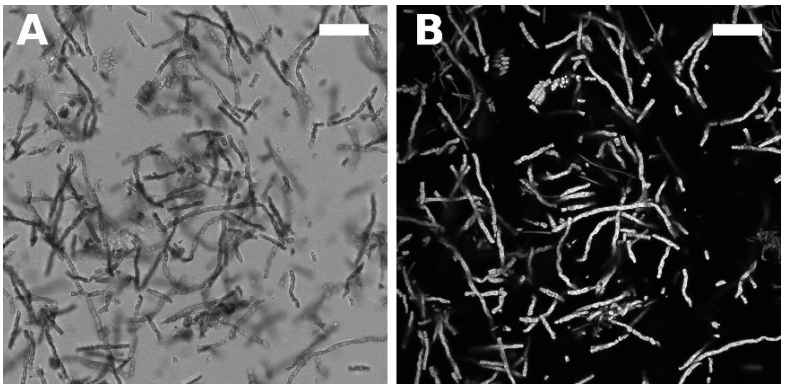

Figure 3.2 – A confocal laser scanning micrograph of the Klebsormidiophyciae that dominated KDP. Bright-field and chlorophyll a autofluorescence are shown in A and B, respectively (Methods). Scale-bars: 50 μm.

the KDP community (Figure 3.3B). This analysis also highlighted the significant coupling between eukaryotic and prokaryotic communities in each patch type (correlation in a symmetric Procrustes rotation: 0.69, $p < 0.01$). Furthermore, using linear discriminant analysis effect sizes (LefSe) [203], we identified taxonomic units that were specifically enriched in the three patch types. Several cyanobacterial taxa were enriched in the DDP, and members of Cytophagia, unclassified Gammaproteobacteria and Sphingomonadales were enriched in CDB (Figure 3.3C). However, the KDP had the largest number of consistently enriched taxa, particularly affiliated with Betaproteobacteria (Burkholderiales) and Alphaproteobacteria (Caulobacterales, Rhodobacterales, Bradyrhizobiaceae and Hyphomicrobiaceae). The specificity of the prokaryotic community was also reflected in terms of diversity (Figure 3.3 D; E; F). While 31.8% of all ASVs were found in all patch types, between 12.3 and 20.7% of ASVs (accounting in total for 45.3% of ASVs) were exclusively detected in either CDB, DDP or KDP (Figure 3.3D). There were no significant differences in terms of ASV richness between the three biofilm components under the two flow regimes, yet, prokaryotic community diversity incorporating evenness (Shannon H) was significantly lower in KDP and DDP as compared to CDB (ANOVA, $F = 11.78$, $p < 0.01$) (Figure 3.3E), reflecting the relative dominance of a few prokaryotic community members in these patches. We found generally small differences between community composition and diversity between the two hydraulic conditions. These results show that diversity across the entire biofilm landscape was composed of a core of abundant and common ASVs, but that nearly half of the ASV diversity was exclusively found in the different patches. Collectively, our results highlight the nested contribution of patch types to overall biofilm diversity. This is analogous to real landscapes and stream ecosystems where biodiversity patterns across scales (*e.g.*, from the stream network to the streambed patch) arise from local communities that assemble from a regional species pool [19;21]. Environmental variation and interactions between hydraulic and microbial processes have been evoked to induce heterogeneity and patchiness of the streambed landscape [155;252] and its biofilms [7]. Strikingly, however, in our experiments, patchiness arosed in the absence of heterogeneity of the substrate. This highlights the coupling between phototrophs and heterotrophs as a potential driver of the patchy biodiversity patterns in biofilms.

Biofilm patches have distinct physical structures that interact with fluid flow. To explore the physical structure of the three patches differing in biodiversity, we inferred thickness, coverage and volume from OCT imaging [55] (Methods). We did not find any significant effect of the hydraulics on the overall thickness, areal coverage and volume of the biofilm, neither at the landscape level, nor at the

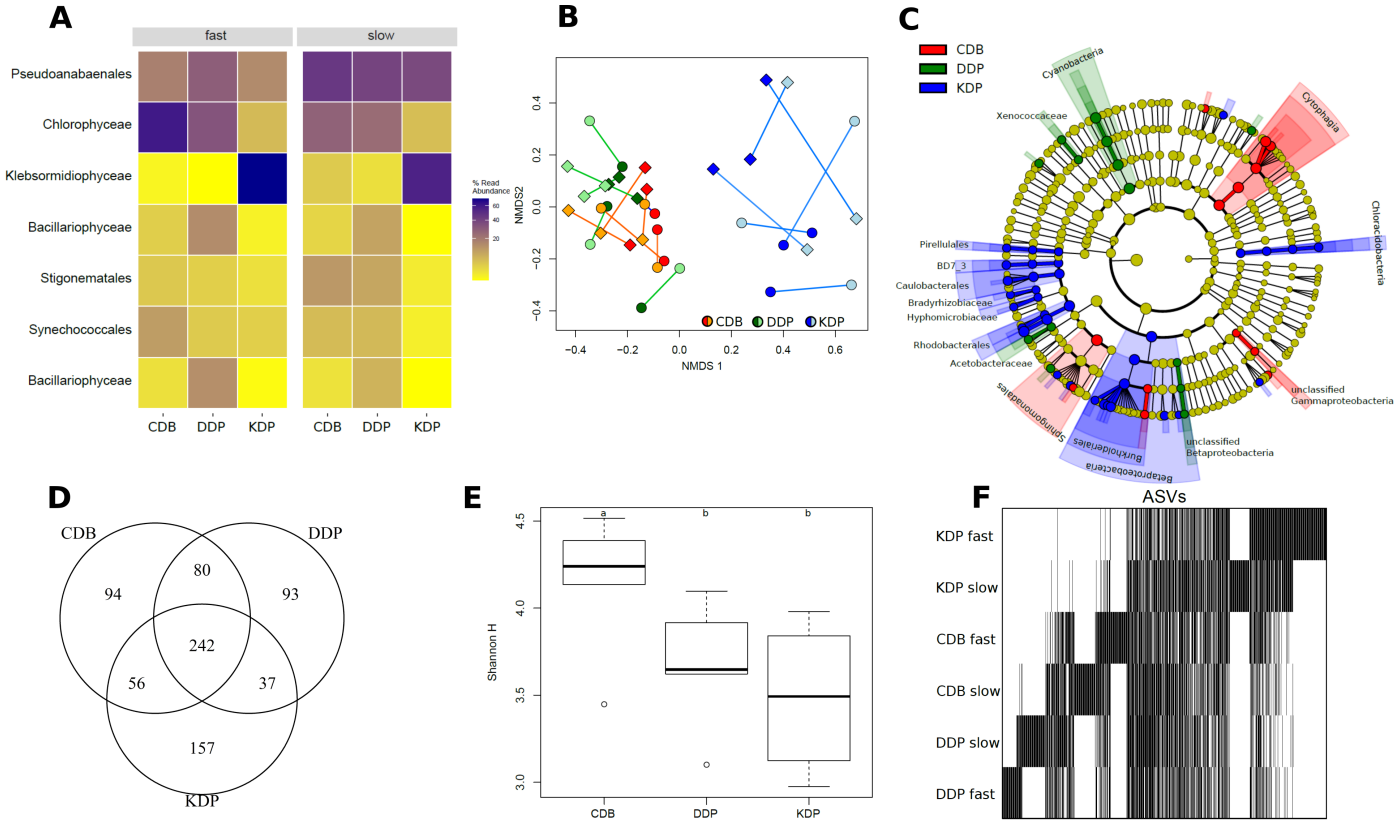

Figure 3.3 – **Patch types differ in composition and their contribution to diversity.** Panel A provides an overview of the distribution of the seven most abundant phototrophic community members, which account for 89.2% of sequence reads. In both flow conditions, Cyanobacteria of the Pseudoanabaenales, Stigonematales and Synechoccales orders dominated the CDB. In addition to these, two Bacillariophyceae ASVs classified as *Achnanthidium saprophilum* were detected in DDP, whereas a single ASV classified as Klebsormidiophyceae (Charophyta) dominated the KDP assemblages (A). Non-metric multidimensional scaling with procrustes superimposition illustrates the compositional similarity of CDB and DDP and the more distinct assemblages in KDP (B). Heterotrophic prokaryotic (lighter color) and phototrophic eukaryotic (darker colors) similarities were significantly linked. Based on relative abundance differences, various prokaryotic community members were found to be specific for the respective patch types (C). Particularly KDP harboured a distinct set of prokaryotic community members. A Venn diagram shows the number of shared and unique prokaryotic ASVs among the three patch types (D). While a similar number of ASVs was detected in each patch type, particularly KDP were dominated by a few abundant prokaryotic ASVs. This is reflected in reduced Shannon H in KDP compared to CDB (E). A patch-by-ASV matrix (F) shows, for each patch type under the two hydraulic conditions, the occurrence of ASVs. Each ASV is represented as a bar and they are ordered by reciprocal averaging to highlight differences in ASV distribution among the different patch types. ASVs common to all patch types form a central band, whereas ASVs specific to each patch type are clustered.

Table 3.1 – Features of the distributions in biofilm thickness across patch types (CDB, DDP, and KDP) and flow conditions, as derived from OCT and macro-photography imaging (Methods).

Community	Median height [mm]	Area [mm^2]	Total area [mm^2]	Coverage [%]	Volume [mm^3]	Total volume [mm^3]	Volume [%]
CDB	0.38	1411	2016	70	591	1033	57
DDP	0.56	408	2016	20	253	1033	25
KDP	0.93	197	2016	10	189	1033	18
CDB	0.36	1145	1601	72	440	766	57
DDP	0.52	314	1601	20	174	766	23
KDP	1.3	142	1601	9	152	766	20

level of CDB, DDP (Table 3.1). However, under high flow velocity, CDB tended to develop into ridges aligned in the flow direction, while KDPs were fewer but larger (Figure 3.4, Table 3.1).

The internal porosity of biofilms is relevant for mass transfer, the chemical heterogeneity and hence for the functioning of the biofilms [98]; however, it is inherently difficult to empirically estimate the porosity within biofilms [132;260]. Using OCT scans (Methods), we estimated the apparent porosity of all three biofilm components ranging from 0.29 ± 0.22 to 0.71 ± 0.15 in CDB and KDP, respectively (Table 3.5). We found that KDP porosity was approximately 1.5 times higher than the CDB and DDP porosity, which is in line with the filamentous and hence porous structure of this patch as revealed by Confocal Laser Scanning Microscopy (Figure 3.2). Our analyses failed to reveal an effect of hydraulics on biofilm porosity. Biofilms not only respond to, but they also influence the adjacent flow environment [80;219;168]. To assess how all three biofilm patches possibly interact with the fluid dynamics, we numerically simulated the flow field within and around each of them (Methods). We found that the three patches differently deflected flow lines both up- and downstream, and this in both flow environments (Figure 3.5). This effect was particularly evident for the protruding KDP, where streamlines also detached to develop a downstream wake. This interaction between the local topography and the flow fields also affected the distribution of the viscous sublayer. Our simulations estimated the latter at 0.13 mm and 0.07 mm under slow and fast flow, respectively. It was generally thinner at the top of KDP (~0.04 mm) protruding into the fluid, and both upstream (0.10 mm) and downstream (0.14) of this patch type. Unexpectedly, our simulations revealed significant fluid flow within the biofilm (Figure 3.5). We consistently observed conspicuous patterns, albeit differently pronounced in the various patch types, of alternating 'downwelling' and upwelling' regions of fluid flow. For instance, in both hydraulic environments, the fluid entered the KDP and traversed it almost parallel to the bulk flow lines, which seems to indicate a high biofilm permeability. Permeability varied from 0.5 x 10^{-10} m^2 to 2 x 10^{-10} m^2, and did not differ between KDP and the other two patches. Despite this, the average flow velocity within the biofilm differed between the three components, which we attribute to their different architectures. Under slow flow, the internal fluid velocity was highest in KDP (0.046 mm s^{-1}), followed by CDB (0.041 mm s^{-1}) and DDP (0.031 mm s^{-1}). Under fast flow, these averages increased to 0.137 mm s^{-1}, 0.061 mm s^{-1}, 0.170 mm s^{-1} for CDB, DDP and KDP, respectively. Our estimates of flow velocity and permeability are significantly higher than those reported from bacterial, mostly monospecies, biofilms [215]. We attribute this to the significant contribution of numerous algal cells that owing to their large size and often filamentous structure increase the porosity of phototrophic biofilms. This is fundamentally different to the densely packed monospecies biofilms typically growing under optimal laboratory conditions. Our findings highlight advection within patches of phototrophic

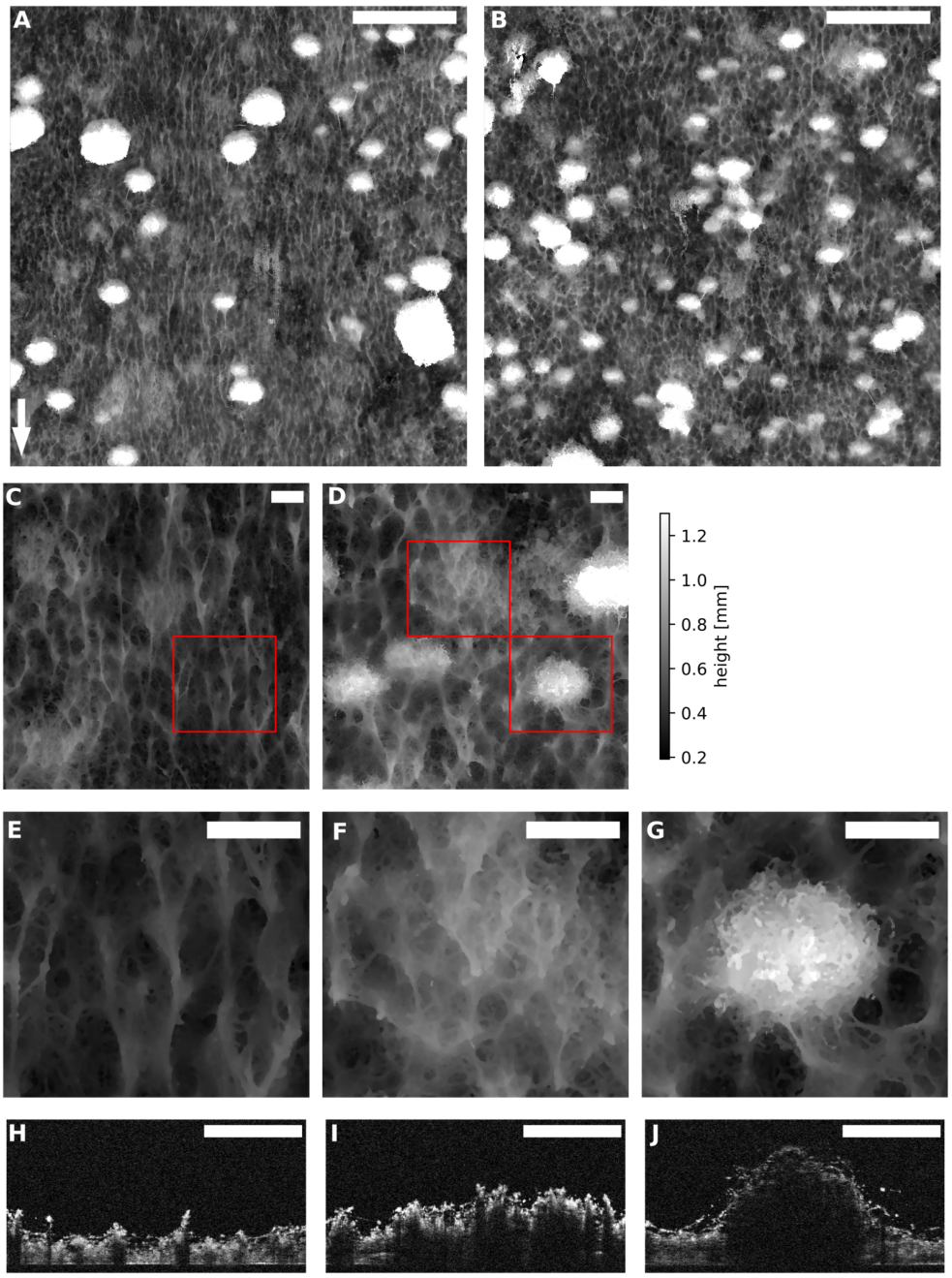

Figure 3.4 – **OCT-derived DEMs of the biofilm topologies.** Optical coherence tomography (OCT) was used to image the tridimensional architecture of biofilm growing under contrasting flow conditions. Several OCT scans acquired in a tiled pattern were processed to obtain digital elevation models (DEMs) in which the biofilm thickness is encoded by the pixel gray level; these were then stitched together. A and B show the final DEM (total area 45 mm x 45 mm) under fast and slow flow conditions, respectively. Scale bars: 10 mm. C and E show an enlarged detail of the CDB topology under fast flow. D and E show an enlarged detail of a DDP under slow flow, and D and F show a KDP under slow flow. Sample OCT B scans for each patch type are also reported in H, I and J (CDB, DDP, KDP, respectively), highlighting their differences in internal porosity. Scale-bars : 1 mm.

biofilms and therefore challenge the current view of diffusion governing mass transport in biofilms [214]. Our results on the upwelling and downwelling patterns are reminiscent of the hydrodynamic exchange of the sediment that that phototrophic biofilms colonize in streams and coastal systems [91;28]. Our findings present first evidence towards an analogy of the structure-function coupling between biofilms and the habitat that they inhabit [7]. Despite their different scales, both the biofilms and sediment beds are porous systems with turbulent mixing that enhances mass transport. We propose that this analogy across scales contributes to the high retention and transformation capacity of small streams dominated by the biofilm mode of life [9].

Patch type and hydraulics affect O_2 dynamics. The spatiotemporal dynamics of O_2 concentration in biofilms results from microbial activity and mass transport [216;215]. To assess the O_2 dynamics across the biofilm, we used OCT-guided, automated microelectrodes and established in total 1,134 depth profiles of O_2 to encompass all three patch types both in light and dark conditions as well as in both hydraulic environments (Methods). We found that the distribution of O_2 concentration within the biofilm, and its variation between light and dark conditions, were different in each patch type (Wilcoxon rank text, p-value < 0.01 for each comparison, Figure 3.6A, Table 3.2); with the exception of KDP compared to CDB under dark conditions (Wilcoxon rank text, p-value = 0.17, Figure 3.6A). In each flow condition, DDP exhibited the largest ranges in O_2 concentration and light/dark fluctuations. Further, within DDP O_2 was more depleted in the dark and accumulated more in the light. Hydraulics also affected the O_2 concentration within the biofilms. In the three patch types and under both light and dark conditions, a faster flow velocity induced a decrease (Wilcoxon rank test, p-value < 0.01) in O_2 concentrations (Figure 3.6A); with the exception of KDP in the dark. Under fast flow, the distributions of O_2 concentration within KDP in both light and dark were narrow and skewed towards the bulk water O_2 content. Light/dark fluctuations in KDP were also strongly diminished under fast flow compared to slow flow.

Table 3.2 – Features of the distributions in O_2 concentration measurements within the different patch types (CDB, DD, and KDP).

Flow	Patch type	Light condition	Median ([0.2 to 0.8] interquantile distance) (max - min) [μmol l^{-1}]
Slow	CDB	dark	307 (31) (332 – 230)
		light	486 (135) (684 – 344)
	DDP	dark	290 (53) (334 – 183)
		light	555 (170) (724 – 341)
	KDP	dark	304 (40) (333 – 226)
		light	525 (127) (698 – 342)
Fast	CDB	dark	277 (41) (329 – 220)
		light	464 (100) (623 – 336)
	DDP	dark	245 (53) (332 – 38)
		light	515 (121) (683 – 338)
	KDP	dark	317 (35) (329 – 213)
		light	363 (80) (604 – 325)

The patch types also affected the overall vertical patterns of O_2 concentration, independent of light/-dark conditions or hydraulic environment (Figure 3.6B). In the dark under fast flow, CDB and DDP presented lower O_2 concentration throughout the biofilm thickness compared to slow flow, while in

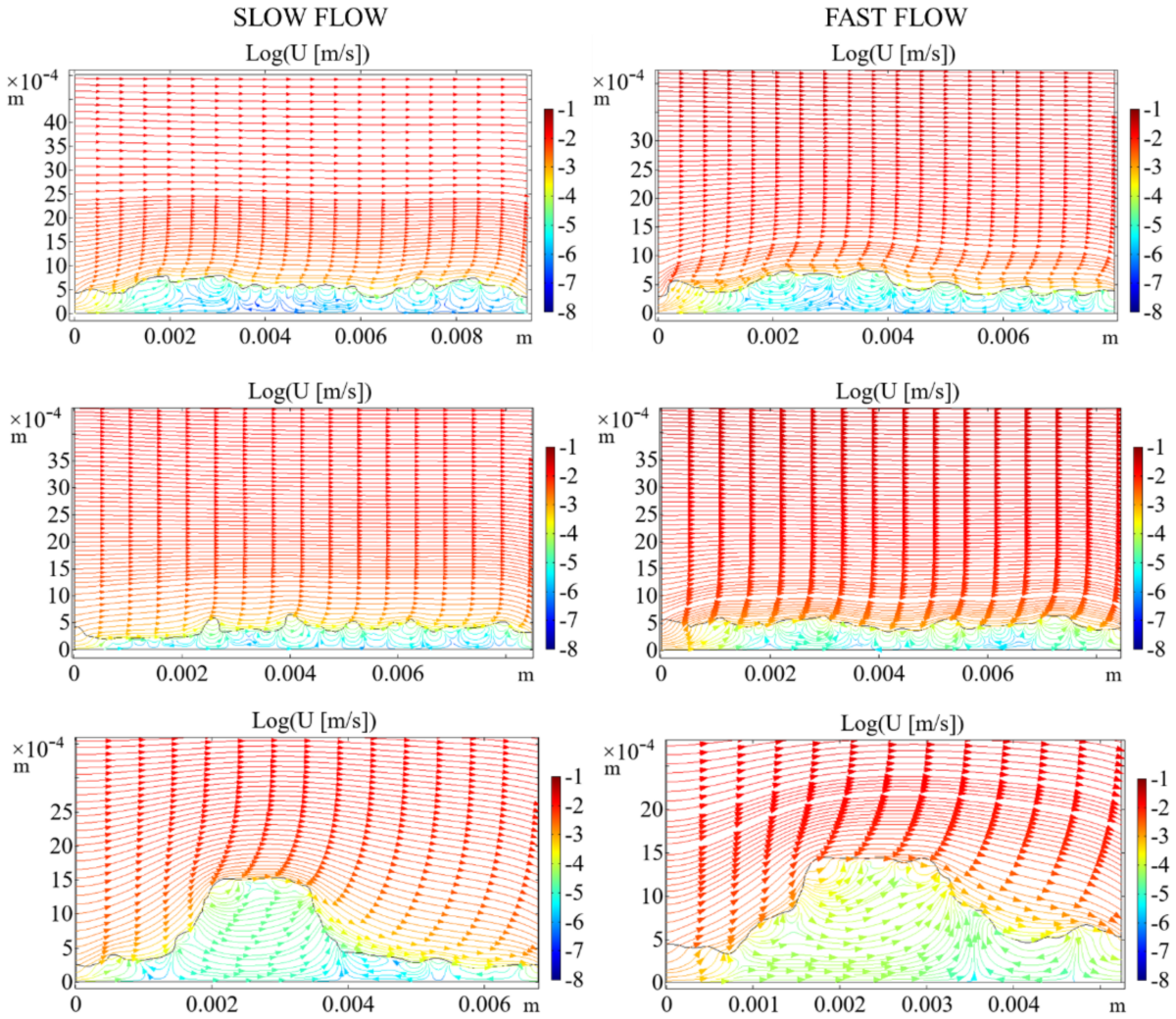

Figure 3.5 – **Fluid motion within and around biofilms.** We used a computational simulation to compare the fluid patterns within and around the biofilm patch-types developed under contrasting hydraulic conditions. Streamlines plots for slow (left) and fast flow (right) conditions for DDP (top), CDB (middle), and KDP (bottom) are shown. The streamlines plots represent the 10^{th} logarithm of the velocity magnitude for the entire computational domain. Streamlines in the water domain follow the biofilm topology, and are especially affected by tall, protruding structures. Further, significant flow patterns within the biofilm domain emerge at the scale of the biofilm topological features and affect transport within the biofilms. Note the streamlines aligned to the main flow direction in KDP, and the upwelling and downwelling patterns in CDB and DDP.

the light slow flow biofilms accumulated more O_2 in deeper layers. We observed that O_2 concentration reached a maximum ~0.5 mm into the DDP patches, while it decreased deeper into the biofilm. In contrast with CDB and DDP, KDP under fast flow exhibited both higher O_2 concentrations in the dark and lower O_2 concentrations in the light. Overall, KDP presented weaker O_2 gradients than the other patch types throughout the thickness of the biofilm, in both light conditions. In CDB and DDP, the gradient of O_2 concentration was higher at the biofilm surface and generally decreased with depth. Therefore, we observed that CDB and DDP presented a strong vertical differentiation of the chemical microenvironment. In contrast, KDP presented weaker internal O_2 gradients and was largely affected by the hydraulic condition.

Patch type affects O_2 transport. In order to explore patterns in O_2 transport within and above biofilm patches, we established transects of O_2 concentration profiles over the different patch types, aligned with the flow direction (Methods). We found that O_2 concentration above the biofilm was relatively homogeneous, which indicates that the diffusive boundary layer was thin and followed the biofilm surface topology (Figure 3.7, Figure 3.1G).
Furthermore, we found that flow had a remarkable effect on the distribution of measured O_2 concentration within KDP. We observed an elevated O_2 concentration upstream and reduced O_2 concentration downstream within the patch (in the dark); an effect that was exacerbated under fast flow (Figure 3.7). This suggests that notable advective transport affected O_2 dynamics within KDP. In contrast, O_2 gradients in CDB and DDP were overall directed towards the substrate, and hence perpendicular to their main flow direction (Figure 3.7).
To gain a better mechanistic understanding of the patterns of O_2 concentration observed within patches, we simulated O_2 production in the light (*i.e.*, net photosynthesis, NP) and consumption in the dark (*i.e.*, respiration, R), and transport within and around the various patch types (Methods). The numerical simulation was parametrized as to best predict the measured transects in O_2 concentration profiles (an example of profiles transect is shown in Figure 3.1G, Table 3.4 reports the optimized parameters for each patch type). We found that the diffusive boundary layer was on average 6 μm and 3 μm thick under slow and fast flow, respectively, and overall followed the patterns of the above mentioned viscous boundary layer. This is in line with our microsensors measurements (Figure 3.1G, Figure 3.13, 3.14), and is likely linked to turbulent mixing (estimated eddy diffusivity reached ~10^{-5} m^2 s^{-1} for both flow environments). In agreement with the simulated patterns of fluid flow, we found that advective transport greatly exceeded diffusive transport of O_2 in the biofilms (Figure 3.8), which was especially evident in KDP, where the ratio between advective and diffusive fluxes reached 86.7, compared to 76.7 and 53.8 in CDB and DDP, respectively. This effect was further exacerbated under high flow velocity, where the average ratio between advective and diffusive transport reached 275.8, 141.7 and 62.1 for KDP, CDB and DDP, respectively. Furthermore, the upwelling and downwelling fluid patterns (Figure 3.8), may have greatly enhanced solute exchange between the biofilm and the bulk fluid. Accordingly, we found that advection accounted for 98.9%of the total O_2 flux across the biofilm surface in KDP, 98.2% and 98.7% of the total flux in DDP and CDB, respectively; a fraction that increased even more under fast flow velocity (KDP: 99.6%; DDP: 98.4%; CDB: 99.3%). Overall, our data highlight that advection allowed for a strong enhancement of mass transport in the three patch types.

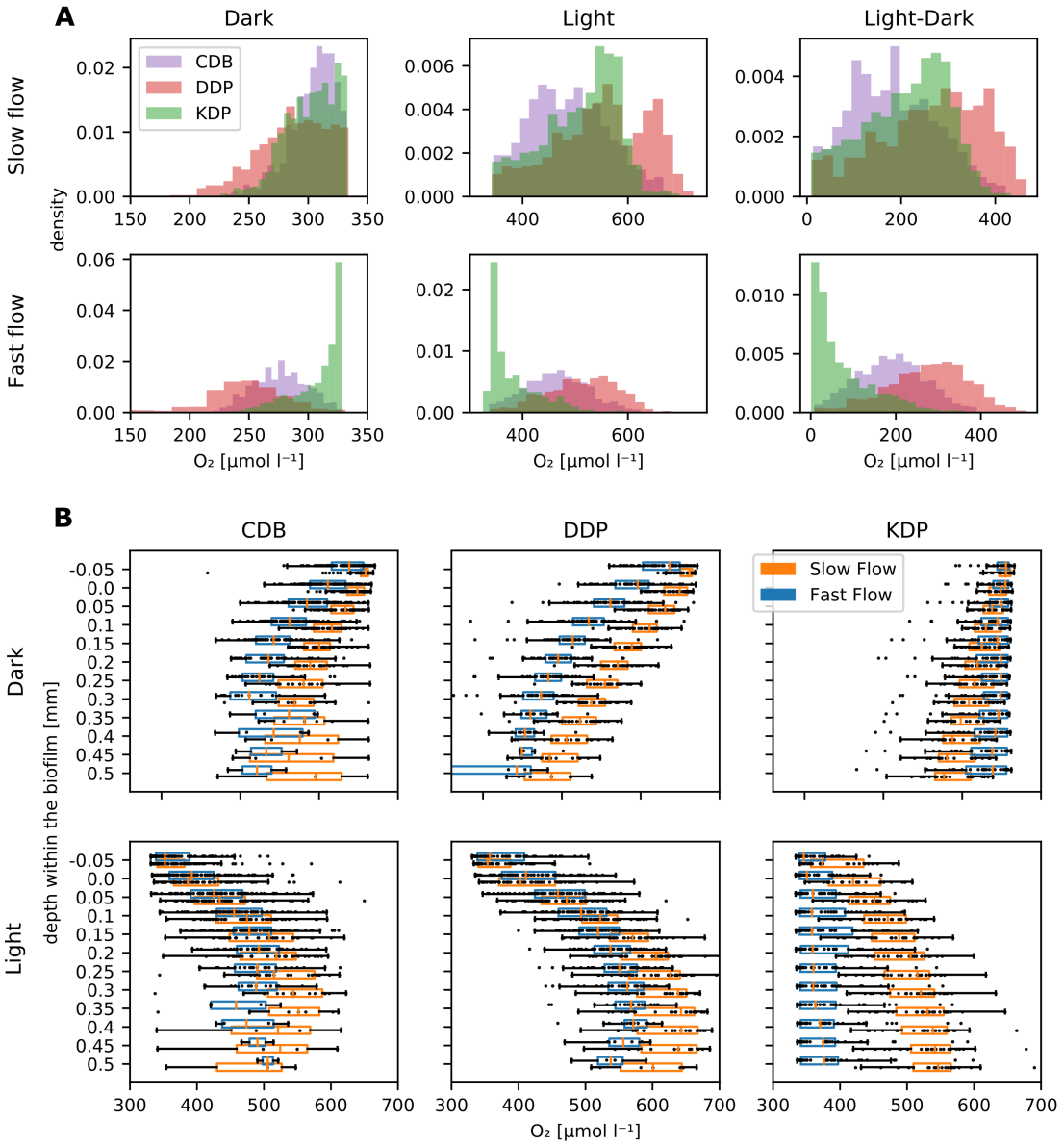

Figure 3.6 – **O_2 dynamics at the landscape scale.** Multiple O_2 concentration micro-profiles were measured over the whole phototrophic biofilm landscape (Methods). Flow, light/dark conditions and patch type (CDB, DDP and KDP, respectively) affected the O_2 concentration within the biofilm, as well as its fluctuations between light/dark conditions. The pooled distributions in O_2 concentration measurements (and light/dark fluctuations) inside the biofilm are shown (A). Flow, light/dark conditions and patch type also affected the vertical variations in O_2 concentration within biofilms, visualized by comparing measurements at the same depth below the biofilm surface (B).

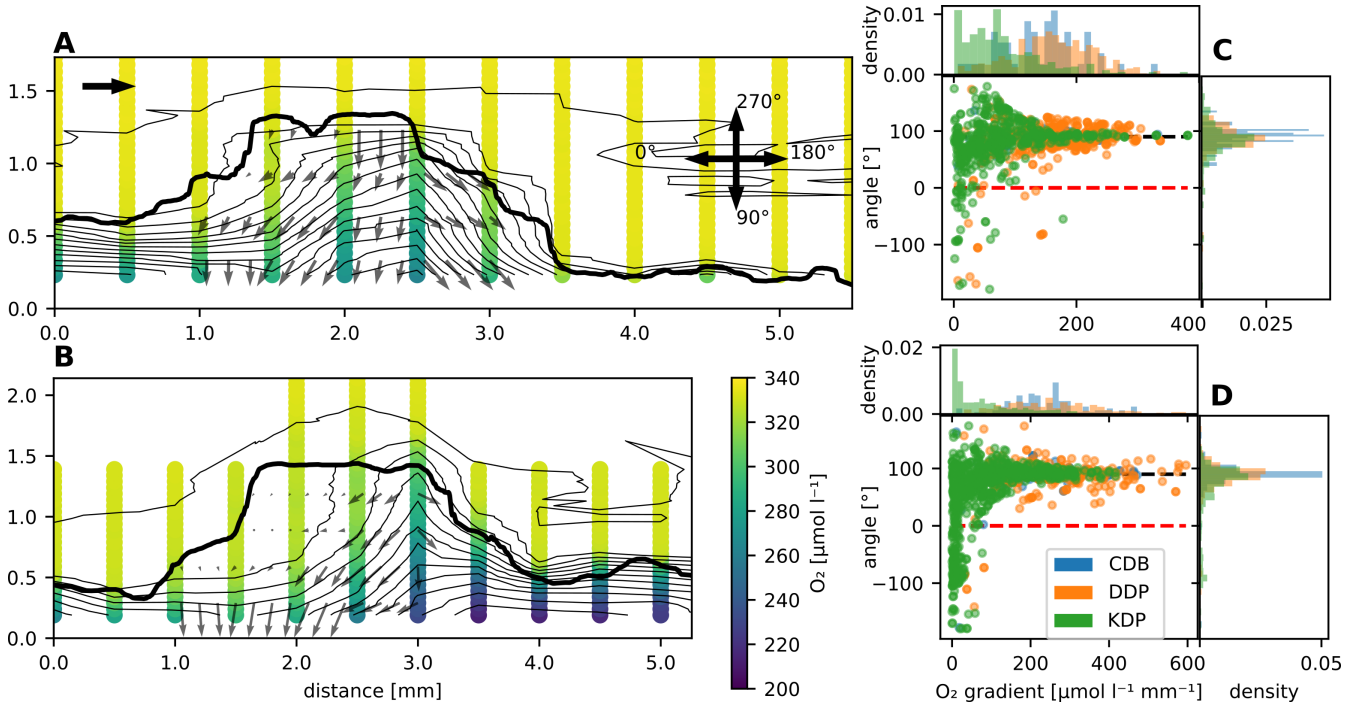

Figure 3.7 – **O_2 dynamics at the patch-scale.** In order to study O_2 dynamics within patches, we measured transects of O_2 concentration profiles across the three different patch types (CDB, DDP, KDP). Examples of profiles transects measured over KDP (in darkness) under slow and fast flow are shown (A and B, respectively). The colored lines indicate the measured O_2 concentration, contour lines show the O_2 concentration field triangulated from the measurements, while the gray arrows indicate intensity and direction of the O_2 concentration gradient. The top-right arrow indicates the direction of the flow. The intensity and direction of the O_2 concentration gradients (in darkness) under slow and fast flow were compared within several replicates per patch type (C and D, respectively). While CDB and DDP gradients were steep and directed towards the substrate (90°, black dashed line), O_2 gradients within KDP were less intense and often bent against the flow direction (0°, dashed red line).

Table 3.3 – Optimized model parameters that best predicted the measured transects of O_2 concentration profiles across different patch types (CDB, DDP and KDP) and flow conditions. Optimized rates of net photosynthesis (NP) and respiration (R) are reported in Table 3.4.

Flow	Patch type	Porosity	O_2 diffusivity (D_{eff}/D_{aq})	Permeability [m^2]	Turbulent Prandtl number	Eddy diffusivity [$m^2\ s^{-1}$]
Slow	**CDB**	0.36	0.7	$1\ 10^{-10}$	0.98	$1\ 10^{-5}$
	DDP	0.47	0.7	$0.6\ 10^{-10}$	0.6	$1.2\ 10^{-5}$
	KDP	0.58	0.8	$1\ 10^{-10}$	0.95	$1.4\ 10^{-5}$
Fast	**CDB**	0.62	0.7	$1\ 10^{-10}$	1	$1.8\ 10^{-5}$
	DDP	0.41	0.5	$0.5\ 10^{-10}$	1	$1.2\ 10^{-5}$
	KDP	0.86	0.9	$2\ 10^{-10}$	0.72	$1.2\ 10^{-5}$

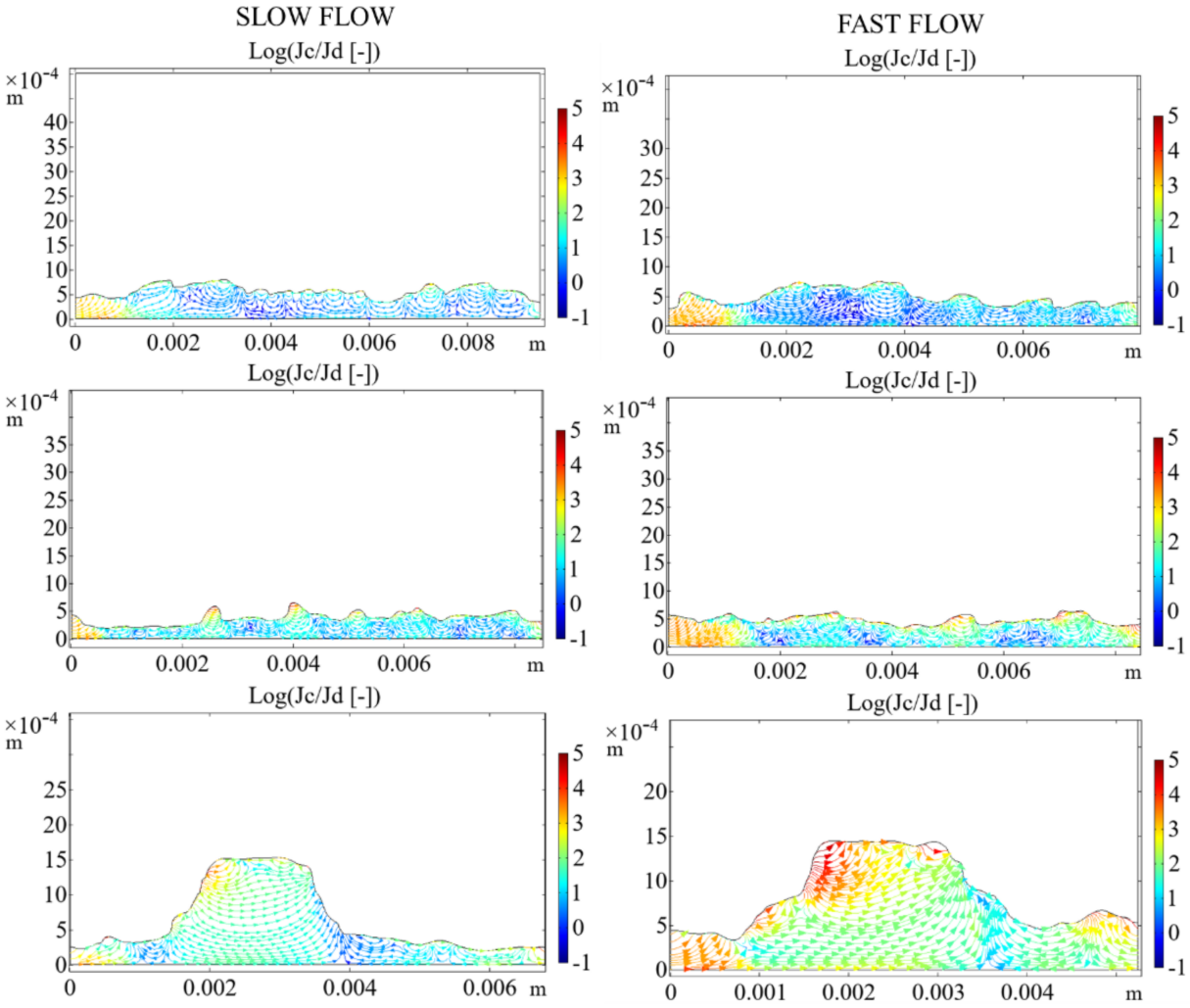

Figure 3.8 – **O_2 transport within and around biofilms.** We used a computational simulation to compare the mass transport patterns within and around the biofilm patch-types developed under contrasting hydraulic conditions. Streamlines plots for slow (left) and fast flow (right) conditions for DDP (top), CDB (middle), and KDP (bottom) are shown. The streamlines plots depict the 10^{th} logarithm of the ratio between advective (Jc) and diffusive (Jd) flux within the biofilm.

Metabolism from the patch scale to the biofilm landscape. Extrapolating fluxes from the patch scale to the landscape is critical to understand the relevance of the various landscape constituents to its overall functioning [136]. To address this, we combined the numerically simulated volumetric rates of NP and R, with OCT-derived estimates of the volume and areal coverage of each biofilm component (Table 3.1, Methods). Overall, patch-level volumetric NP ranged from 1.1 to 5.38 mmol O_2 $m^{-3}s^{-1}$ and R from -0.55 to -1.61 mmol O_2 $m^{-3}s^{-1}$, and R was generally higher under fast than slow flow (Table 3.4). At the landscape-level, R fluxes reached 0.69 mmol O_2 $m^{-2}s^{-1}$ and 0.44 mmol O_2 $m^{-2}s^{-1}$, while NP fluxes reached 1.8 mmol O_2 $m^{-2}s^{-1}$ and 2.11 mmol O_2 $m^{-2}s^{-1}$ (under fast and slow flow, respectively). These volumetric rates and areal fluxes are closely bracketed by those computed from microsensor profiles in microbial mats dominated by cyanobacteria and diatoms from salt marshes [115;87]. We consider this as a confirmation that our combined approach of microelectrode measurements and numerical modelling provided reliable estimates of metabolic fluxes. Furthermore, we found that the contributions from CDB, DDP and KDP to the landscape-level metabolism largely reflected their relative contribution by volume (Table 3.4).

By subtracting R to NP, we calculated the net O_2 balance (as net ecosystem production, NEP) of the biofilm components (Table 3.4). We found that all patches were net producers of O_2, with the notable exception of KDP under fast flow (Table 3.4). The positive NEP is in general agreement with previous findings on cyanobacterial biofilms from hypersaline mats [70;249], for instance. In streams, the ecosystem metabolism is generally net heterotrophic except for certain windows, such as in spring, when copious algal growth can change the metabolism to autotrophy [15]. We argue that our benthic biofilms with their marked positive NEP are representative for the phototrophic biofilms during these windows — potentially even overwhelming the heterotrophy within the deeper sediments of the streams.

Despite limited community turnover and an overall similar porosity across flow regimes, the hydraulic condition affected the metabolic rates of the biofilm. Under fast flow, R increased for the three biofilm components. This was consistent with the shift towards more depleted O_2 concentrations observed by O_2 microprofiling in CDB and DDP. NP decreased under fast flow in KDP and DDP, when compared to slow flow. This effect is possibly linked to an increased respiration during illuminated periods. The opposite response of R and NP to the hydraulic environment indicates that different factors controlled photosynthesis and respiration in the biofilms under study. We suspect that the strong advective flow may have replenished resources limiting respiration. At the landscape-scale, NEP under fast flow was 66% lower than under slow flow, an effect that was linked both to a decreased NP and enhanced R. Hence, our results indicate that higher flow velocity can trigger a shift towards a less autotrophic metabolism in three different phototrophic communities. These patch-level processes then integrate into a landscape-level metabolic response.

Table 3.4 – Modeled volumetric rates [mmol O_2 m^{-3} s^{-1}] of respiration in the dark (R) and net photosynthesis in the light (NP) were used to estimate the net O_2 balance (NEP = NP - R) of each patch type (CDB, DDP and KDP). O_2 fluxes (across the projected, planar area) [mmol O_2 m^{-2} s^{-1}], were calculated based on the areal coverage and volume of each patch type (Methods). These values were used to estimate the overall O_2 balance of the whole microbial landscape, both as volumetric rate and areal flux. The contribution of each patch to the landscape metabolism is also reported (R [%], NP [%])

Flow	Community	R [mmol m^{-3} s^{-1}]	NP [mmol m^{-3} s^{-1}]	NEP [mmol m^{-3} s^{-1}]	R [mmol m^{-2} s^{-1}]	NP [mmol m^{-2} s^{-1}]	NEP [mmol m^{-2} s^{-1}]	R [%]	NP [%]
Fast	CDB	-1.61	5.38	3.77	-0.62	2.06	1.45	64	82
	DDP	-1.11	2.06	0.94	-0.62	1.14	0.52	17	12
	KDP	-1.37	1.1	-0.28	-1.48	1.18	-0.3	19	6
	landscape	-1.45	3.77	2.32	-0.69	1.8	1.11	100	100
Slow	CDB	-0.98	5.09	4.11	-0.41	2.13	1.72	65	71
	DDP	-0.55	3.01	2.46	-0.34	1.87	1.53	16	18
	KDP	-0.88	2.54	1.66	-0.84	2.42	1.58	19	11
	landscape	-0.86	4.11	3.26	-0.44	2.11	1.67	100	100

Conclusion

Combining OCT-imaging with microelectrode profiling, numerical simulations and amplicon sequencing, we highlighted the structural and functional patchiness of a phototrophic biofilm. While patchiness in streams is often related to a heterogeneous environment [252;156], our findings suggest that small-scale patchiness can also exist in a relatively homogeneous environment, potentially emanating from biotic processes or simply randomness. While the spatial patchiness of physical structures in monospecies biofilms has been acknowledged for decades, it has been rarely addressed for complex phototrophic biofilms harboring hundreds if not thousands of microbial taxa. We found that phototrophic biofilms emerge as complex landscapes, in which different communities coexist within spatially segregated patches. The functioning of these patches is linked to their structural features, which, by interacting with fluid dynamics, generate different physicochemical micro-niches within the biofilm landscape. Our findings also highlight the role of hydraulics, that allows for pervasive advective transport around and within the biofilm patches, and that can induce a metabolic shift at the scale of the entire biofilm landscape. Our landscape approach has revealed patchiness as a hitherto unrecognized driver of diversity in natural phototrophic biofilms and the interactions of patches with the fluid dynamics as a driver of their metabolism. The notion of biofilms as microbial landscapes [12;175] is critical to predict and understand their functions that underlie ecosystem processes. In this context, our findings shed new light on the biofilm machinery of stream ecosystem metabolism and its consequences for large-scale biogeochemical fluxes.

Methods

Biofilm cultivation. Water from Lake Geneva was continuously filtered (nominal pore size 50 μm, FA 10 SX 50 ATLAS FILTRI) into a 1 m^3 reservoir and from there pumped into an open-channel flume. A constant flow rate (2.22 10-4 m^3 s^{-1}) was supplied using valves equipped with flow meters. Water was partially recirculated in a large reservoir. Water temperature varied between 14.5 °C and 15.5 °C

throughout the experiment. Total dissolved organic carbon (DOC) was quantified in a filtered sample (pre-ashed GF/F, Whatman) using a TOC carbon analyzer (Sievers M9 TOC Analyser, GE). DOC averaged 824 ± 65 ppb. Phosphate, ammonium, nitrite and nitrate were measured with a Lachat QuikChem 8500 flow injection analyser (QuikChem Methods 10-115-01-1-M (PO_4^{3-}), 10-107-04-1-B (NO_3/NO_2), 10-107-05-1-C (NO_2) and 10-107-06-3-D (NH_3)). Average concentrations were 3.75 ± 0.75 ppb, 36 ± 11 ppb, 386 ± 22 ppb for PO_4-4, NH_4-N and NO_3-N, respectively. Hence, C:N, C:P and N:P ratios were 2.3, 567, and 249, respectively. Light (~13 W m^{-2}, JAZ spectrometer Ocean Optics) was provided for 12 hours a day using a combination of red and blue LEDs. The flumes were constructed from plexiglass with a funnel-like shape, with flume width increasing gradually from 0.05 m to 0.3 m in the flow direction, imposing a gradient in decreasing flow velocity [55]. Average water depth was 0.022 m. Mean flow velocity (u), estimated from the flume geometry, the water depth (0.022 m), and discharge (2.22 10^{-4} m^3 s^{-1}) as:

$u = \frac{Q}{h \times w}$

ranged between 0.06 m s^{-1} and 0.13 m s^{-1}. Flow velocity depth profiles and root-mean-square velocity fluctuations at the extremes of the hydraulic gradients were measured by LDV (on the clean plexiglass without biofilms, Figure 3.9). From these, we calculated flow velocity and turbulent kinetic energy (averaged between 0 mm and 10 mm from the plexiglass surface). Strong turbulence eddies characterized the flow patterns, which was considerably unsteady. Prior to experiments, phototrophic biofilms growing continuously in the reservoir were harvested and disaggregated by shaking. The slurry was filtered using (41 μm nylon filter, Millipore) and diluted into 8 l of lake water. The biofilm slurry was then poured into the flumes and incubated for 12 hours without flow (under light). This seeding step produced a thin layer of base biofilm evenly covering the flume bottom. After seeding, the flow was started and biofilm was allowed to grow without disturbance for 30 days.

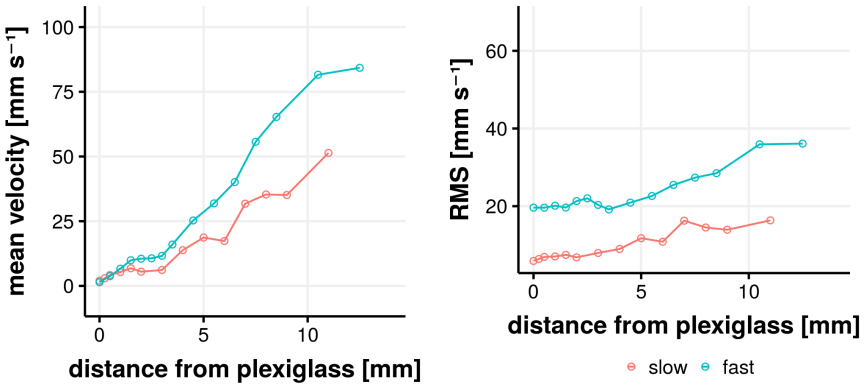

Figure 3.9 – Flow velocity and turbulence (as root-mean-square of the velocity fluctuations, RMS) profiles measured by laser doppler velocimetry (LDV) at the slow- and fast-flow extremes of the velocity gradient.

OCT and macro-photography data acquisition and processing. We used a spectral domain optical coherence tomographer (GANYMEDE, Thorlabs GmbH, Germany) centered at 930 nm and equipped with an immersion adapter. OCT datasets were acquired averaging 3 A-scans and had a resolution of 11 μm in x and y and 2.18 μm in z direction, covering a volume of 10 mm × 10 mm × 2.23 mm. We mounted the OCT probe on a precision positioning device (STEPCRAFT, 30 μm precision in x,y), as described previously [55]. Automatic positioning and OCT scan acquisition allowed us to obtain 6 × 6

OCT scans in a mosaic pattern (overlap was set to 30 % of the field of view), which were processed to obtain a digital elevation model (DEM) of the biofilm surface topology. Then, DEMs were denoised with a median filter (size of 4 pixels) and stitched [55]. The final DEMs covered a total field of ~45 mm x 45 mm at both ends of the velocity gradient. Biovolume was estimated as the volume beneath the biofilm surface, (*i.e.*, the sum of all pixel values in the DEM). This was supported by visual inspection of the OCT images, which did not reveal the presence of voids below the biofilm surface. Median biofilm thickness and interquantile range (calculated between the 0.2 and the 0.8 quantiles) were calculated from the distribution of pixels grey-level in the DEM. Similarly, we mounted a camera (Canon EOS 7D Mark II) equipped with a macro-objective on the precision positioning robot and acquired a large set of pictures in a mosaic pattern, which was assembled using the software Image Composite Editor Version 2.0.3.0 (Microsoft corporation). We used this picture to segment the three patch types (CDB, DDP and KDP) based on their coloration. More specifically, DDP were identified imposing a threshold on the ratio between the red and green channels. Then, KDP were identified by thresholding a combination of the original green channel and a local mean filter on the same channel. Then, small objects and holes were discarded and the final KPD binary mask was dilated of 5 pixels. The parts of the photographs that were neither diatoms or tufts were labeled as CDB. The outcome of this segmentation algorithm was confirmed by visual comparison with the macro-photographs. Macro-photographs and OCT-derived DEMs were aligned manually, which allowed to estimate the thickness distribution of each patch type. An example of the output of this segmentation algorithm is shown in Figure 3.10).

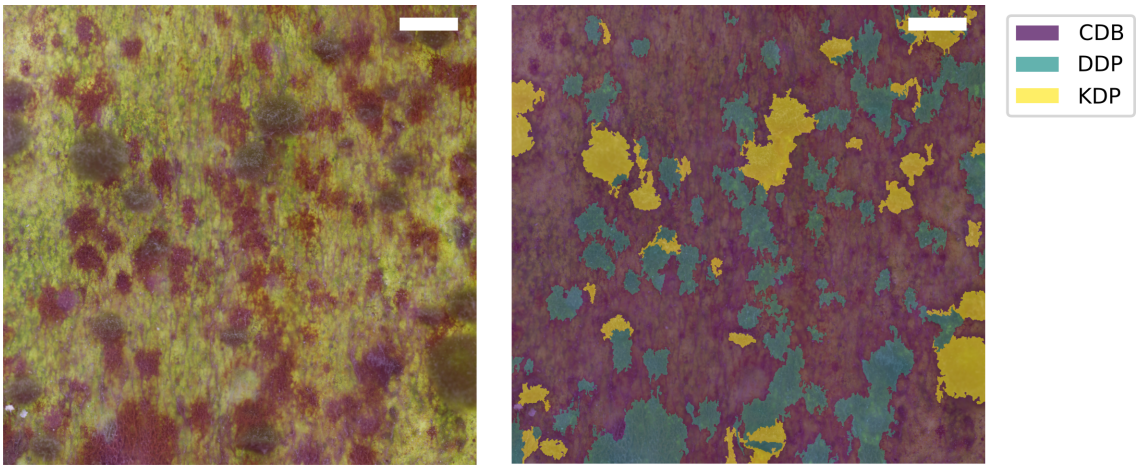

Figure 3.10 – Segmentation of the three patch types from the macro-photographs. Biofilms were imaged by macro-photography (A, Methods). A segmentation algorithm was applied to distinguish the three patch types (CDB, DDP and KDP) based on their color (B). Scale-bars: 5 mm.

Porosity estimate from the OCT scans. The porosity of the three patch types was estimated from the OCT B-scans. Voids spaces and biomass were segmented based on two gray-level thresholds (120, 130). Because of the limited penetration of light within the biofilm, we selected the top layer below the biofilm surface (two thicknesses, 0.1 mm and 0.2 mm). Then, we excluded structures reaching out of the OCT imaging depth in water (~1.2 mm). Porosity was then estimated as the ratio between biomass volume and the total volume (below the biofilm surface) in each x, y position in the OCT scan (Table 3.5, Figure 3.11), and the median porosity was calculated within each patch type based on the macro-photographs, as described above.

Table 3.5 – Estimated porosity (mean ± standard deviation) from the OCT scans of biofilms growing under fast and slow flow, by patch type (CDB, DDP, and KDP). Porosity was estimated considering the surface layer of the biofilm (either 0.1 or 0.2 mm thick) and testing two gray-level thresholds (125 and 130) to separate biomass and voids.

Flow	Parameters	CDB	DDP	KDP
Fast	0.1 μm; gray-level :125	0.29 ± 0.22	0.26 ± 0.25	0.59 ± 0.22
	0.1 μm; gray-level :130	0.38 ± 0.24	0.34 ± 0.28	0.71 ± 0.21
	0.2 μm; gray-level :125	0.35 ± 0.16	0.35 ± 0.18	0.64 ± 0.16
	0.2 μm; gray-level :130	0.47 ± 0.16	0.46 ± 0.19	0.76 ± 0.15
Slow	0.1 μm; gray-level :125	0.29 ± 0.24	0.29 ± 0.25	0.53 ± 0.23
	0.1 μm; gray-level :130	0.39 ± 0.25	0.37 ± 0.26	0.64 ± 0.23
	0.2 μm; gray-level :125	0.36 ± 0.16	0.36 ± 0.17	0.59 ± 0.16
	0.2 μm; gray-level :130	0.47 ± 0.16	0.46 ± 0.17	0.71 ± 0.15

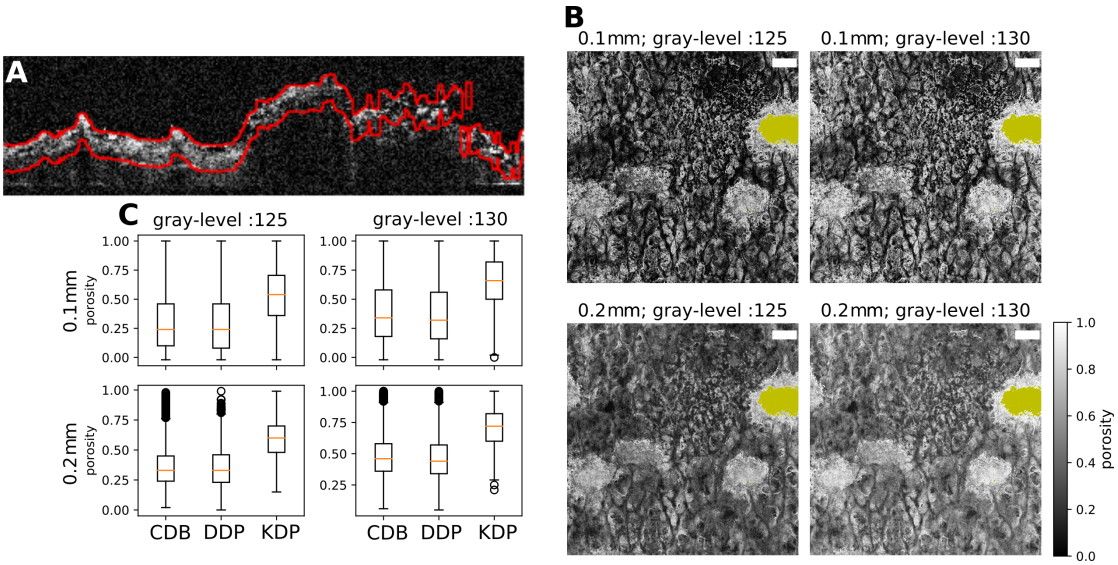

Figure 3.11 – Porosity of the top layer below the biofilm surface was estimated as the ratio of void volume over the total volume for each x, y position in a selected OCT scan. An example of the selected layer is depicted by the red lines overlaid on the respective OCT B scan (A). Two layer thicknesses were tested, 0.1 mm and 0.2 mm. Two gray-level thresholds were also tested to segment biomass and voids (120,130). Lastly, biofilm parts that were too tall to be scanned by OCT were excluded (in yellow) (B). Based on the macro-photographs, the porosity distribution for structures of each patch type was computed (C).

Microsensors measurement and O_2 concentration profiles analysis. O_2 concentration profiles were measured with a fast-response Clark-type O_2 microsensor (tip diameter 50 μm, OX-50, Unisense A/S, Aarhus, Denmark), in depth-steps of 50 μm. The microelectrode was calibrated in air saturated water and anoxic sodium ascorbate solution. The microsensor was vertically mounted on a motorized micromanipulator (Unisense A/S) and connected to a laptop-interfaced microsensor multimeter (Unisense A/S). Data acquisition and micromanipulator positioning were controlled by a dedicated software (Sensor TracePro, Unisense A/S). Profiles were taken in light and dark, with a lag period of 1 hour after changing light condition. The micromanipulator was mounted on a precision positioning robot alongside the OCT probe. In order to calibrate the position of the microsensor with respect to the OCT scans, a parafilm membrane was fixed at 2 mm from the plexiglass surface, and four holes were pierced in it using the microsensor tip. The holes in the membrane were then scanned by OCT in order to calculate the relative shift in x, y directions of the microsensor relative to the OCT scan. Profiles were measured in both fast (n = 301) and slow (n = 293) flow conditions, following an experimental design including both points- and transects- measurements (Figure 3.12A). Profiles were taken in light and dark conditions, allowing for the O_2 gradients to stabilize for at least one hour between light conditions. To account for changes in the O_2 concentration in the water column, we corrected the O_2 concentration measurements by subtracting the average shift in O_2 concentration in the water (far away from the biofilm surface) for each condition. Figures 3.13 and 3.14 report two examples of transects of O_2 concentration profiles aligned with the OCT B-scans and macrophotographs. The position of the biofilm surface was recorded in a few profiles using an endoscope. This estimate was further refined based on the inflection point of profiles in dark and light conditions aligned with the OCT B-scans (Figure 3.12C). To test for differences in the distributions of O_2 concentration measured inside each patch type, we pooled all the measurements below the biofilm surface by patch type, light/dark condition and flow condition. We compared distributions among different patch types within the same flow and light conditions using the Wilcoxon rank test (significance level 0.01). Using the same test, we compared distributions between flow conditions, within the same patch type and light condition. To test for statistical differences in the distributions of O_2 concentration at the same depth below the biofilm surface, we aligned each profile based on the latter. Then, we compared measurements at the same depth below (or above) the biofilm surface using the unpaired Welch two-sample t-test (significance level 0.05). To analyze within- patches O_2 dynamics, we triangulated measurements within transects of O_2 concentration profiles in each patch type and flow condition (in the dark) and measured the intensity and direction of the two-dimensional O_2 concentration gradients for each measurement point.

DNA extraction, sequencing and bioinformatics. We sampled biofilms exposed to two contrasting hydraulic conditions using sterile blades, and we dissected biofilms into patch types under a microscope. Samples were flash frozen at - 80°C and the DNA was isolated using the DNeasy Power Soil kit (QIAGEN). The 16S and 18S rRNA genes were amplified using PCR with the 341f (5'CCTACGGGNGGCWGCAG-3') and 785r (5'-GACTACHVGGGTATCTAAKCC-3'; Klindworth et al., 2012) and TAReuk454FWD1 (5'-TCGTCGGCAGCGTCAGATGTGTATAAGAGACAG-3') and TAReukREV3 (5'-GTCTCGTGGGCTCGGAGATGTGTATAAGAGACA-3';[217]) primer pairs, for prokaryotic and eukaryotic community members, respectively. We prepared sequencing libraries using the Nextera XT kit (Illumina), equimolar pooled and sequenced on a 300 bp paired-end MiSeq (Illumina) run at the Lausanne Genomic Technology Facility (LGTF). We clipped the sequencing adapters from the raw reads, which were subsequently denoised and clustered into Amplicon Sequence Variants (ASV) using dada2 (vers. 1.14)[37] as implemented in qiime2[30]. After taxonomic assignment, autotrophic community members were extracted from the 18S dataset and merged with cyanobacterial reads from the 16S dataset, ac-

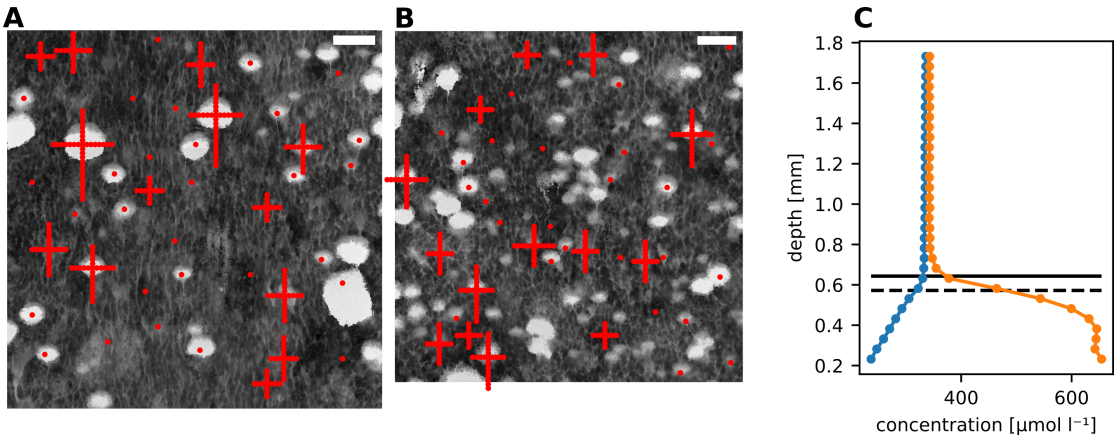

Figure 3.12 – Locations of each measured O_2 concentration profile with respect to the OCT-derived DEMs under fast and slow flow are shown (A and B, respectively).The profiles in transects (flow- and span- directions) are spaced 0.5 mm. Scale bars: 5 mm. For each location, O_2 concentration profiles were measured in both light and dark conditions. An example of a profile taken on in CDB under fast flow is also shown, in dark (blue) and light (orange) (C). The dashed line shows the position of the biofilm surface estimated from the splines inflection points, the full black line indicates the position of the biofilm surface indicated by the OCT scans.

counting for the number of reads in both datasets. Multivariate and diversity analyses were performed in R using the packages vegan, betapart, metacom and VennDiagram.

Confocal laser scanning microscopy. Biofilms samples were embedded in optimal cutting temperature (OCT) compound at the end of the experiment and frozen. Thin sections (50 μm) were cryosectioned and immediately imaged by confocal laser scanning microscopy (Leica SP8 FLIM equipped with a Supercontinuum White Light Laser). Chlorphyll a autofluorescence was collected between 664 nm and 750 nm, and excited at 670 nm. Phycocyanin autofluorescence was excited at 594 nm and collected between 640 and 660 nm.

Numerical model.A computational model was built in COMSOL Multiphysics 5.5 (COMSOL Multiphysics 5.5a, 2019), which is based on the finite element method. It takes into consideration both the surface flow (water) and the biofilm (water saturated porous media) part in a two-dimensional domain. The model solves for both the fluid flow and the O_2 transport. Two different transport conditions are simulated: the consumption and the production of O_2 by the biofilm in dark and light conditions, respectively. The simulations are used to predict the following parameters: production/consumption rate R [mol m^{-3} s^{-1})], biofilm permeability K [m^2] and porosity ϵ [-], effective diffusivity coefficient C = D_{eff}/D_{aq} [-], turbulent Prandtl number $P_{rt} = \nu_t/D_t$ (with ν_t the eddy viscosity [m^2 s^{-1}]), and the eddy diffusivity D_t [m^2 s^{-1}]. To obtain the parameters values an optimization procedure is carried out using COMSOL Multiphysics 5.5. The biofilm geometries represent realistic biofilms types reconstructed from OCT images of experimental transects (Figure 3.15). The domain has a constant height of 0.005 m, while its width varies from ~0.004 m to ~0.01 m, according to the type of biofilm, and is decomposed using an unstructured grid made of triangles and quads elements with a total number of cells of ~$5{\cdot}10^4$. The maximum and minimum element sizes are ~$1{\cdot}10^{-4}$ and ~$1{\cdot}10^{-5}$, respectively. The mesh size is refined at the fluid-biofilm interface and an inflation layer is created at the bottom of the biofilm to

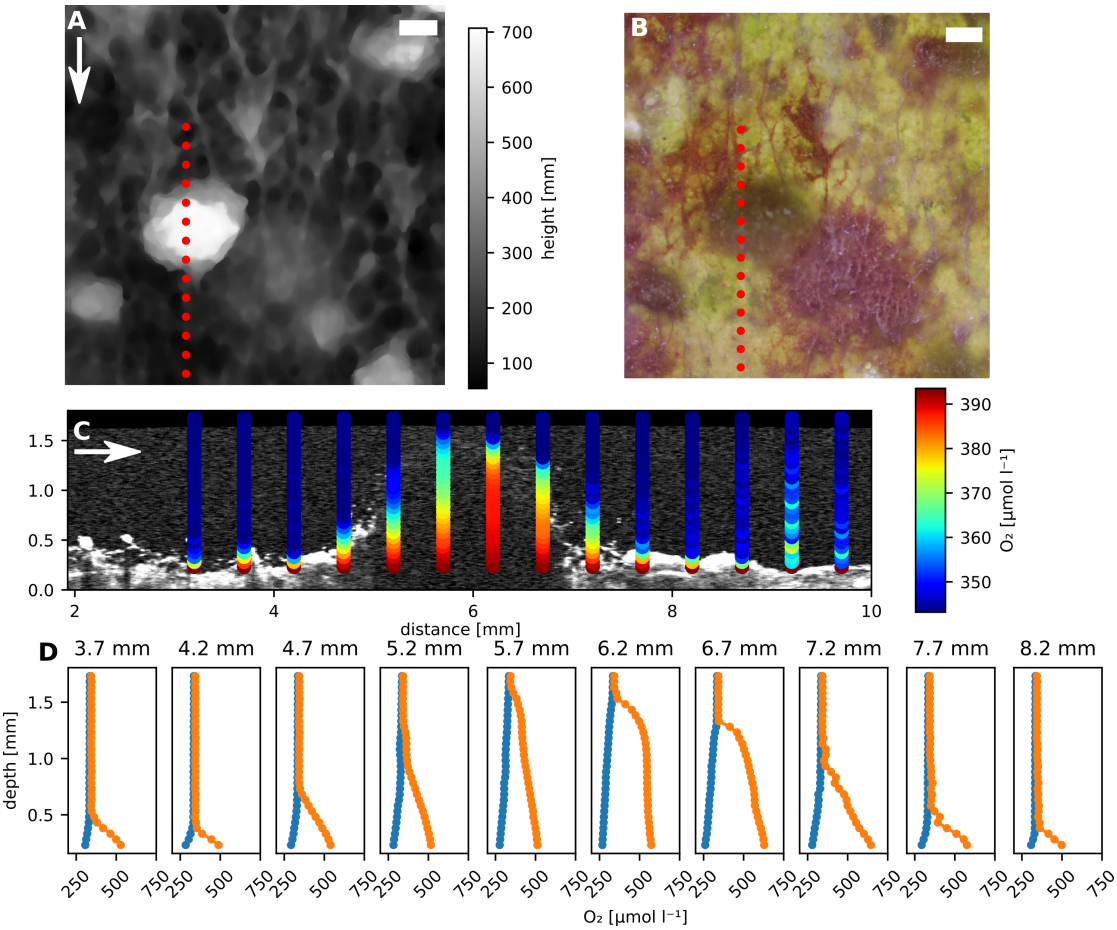

Figure 3.13 – A sample of a transect of O_2 concentration profiles across a KDP is shown. Profiles were measured in both light and dark, in locations spaced 0.5 mm apart, with a z-step of 0.05 mm. A and B show the OCT-derived DEM and macro-photograph of a KDP grown under slow flow, while the red dots indicate the position of the measured profiles. Scale bars: 1 mm. C shows the OCT B-scan overlaid with the O_2 concentration measurement locations, color coded with the relative concentration in illuminated conditions. The flow direction is indicated by the arrows. D reports the same profiles, in light (orange) and dark (blue).

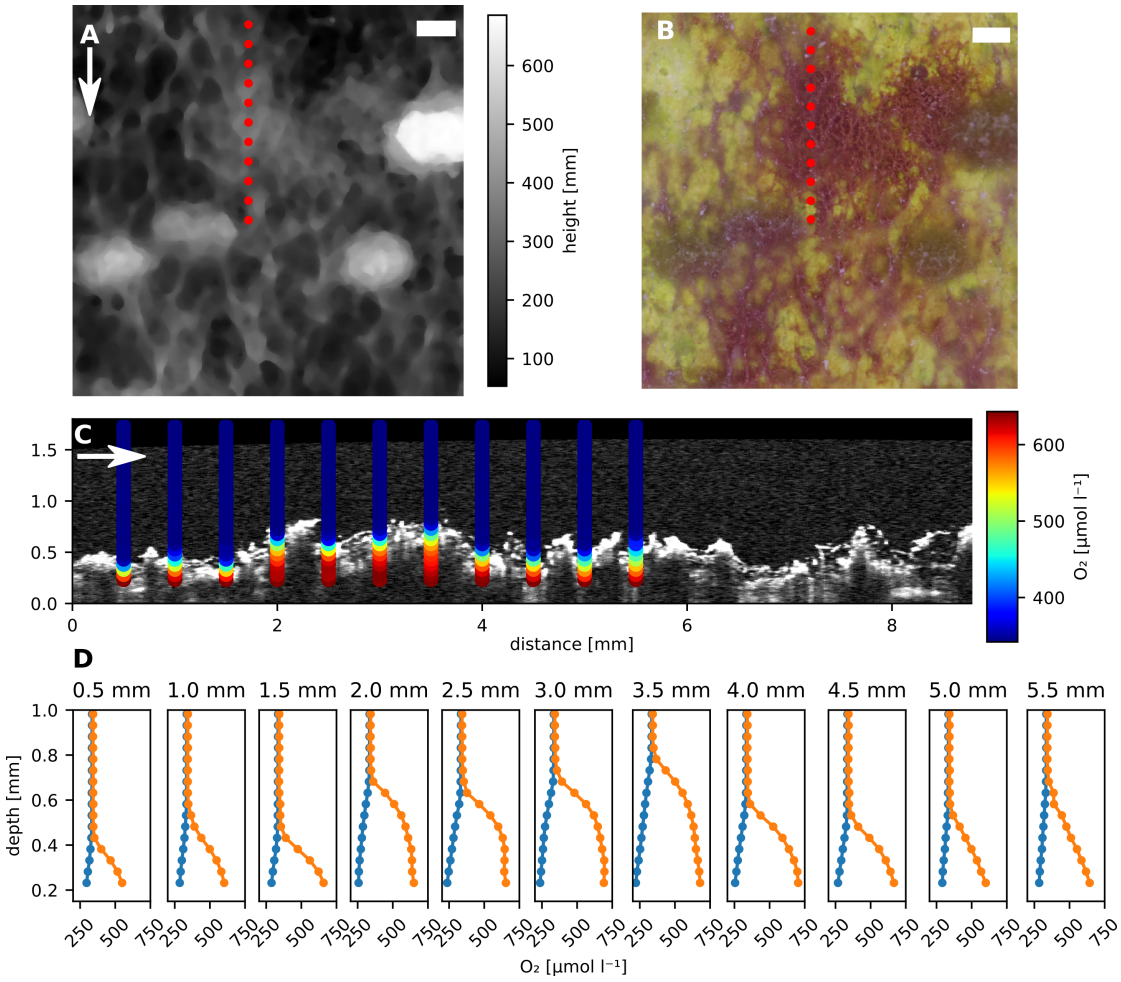

Figure 3.14 – A sample of a transect of O_2 concentration profiles across a DDP is shown. Profiles were measured in both light and dark, in locations spaced 0.5 mm apart, with a z-step of 0.05 mm. A and B show the OCT-derived DEM and macro-photograph of a DDP grown under slow flow, while the red dots indicate the position of the measured profiles. Scale bars: 1 mm. C shows the OCT B-scan overlaid with the O_2 concentration measurement locations, color coded with the relative concentration in illuminated conditions. The flow direction is indicated by the arrows. D reports the same profiles, in light (orange) and dark (blue).

mimic the boundary layer formation. This grid allows a convergence with residuals lower than ~$1{\cdot}10^{-6}$. An example of the mesh features can be seen in Figure 3.16. As far as the boundary conditions of the flow problem are concerned, a velocity profile is set at the inlet. This profile is obtained from the fitting of LDV measurements (Figure 3.9), considering only the points within the domain height (0.005 m - 14 points). Various polynomial fits are tested and a quadratic one is used, given that it best represents the experimental data. At the outlet a zero static pressure is established. A no-slip condition is set at the bottom of the biofilm, and a slip condition is selected for the top of the flow domain to take into account the remaining fluid above the considered domain. Regarding the transport problem, a different concentration profile for each biofilm type is imposed as inlet boundary condition, while at the outlet an outflow condition is imposed. A zero flux is established at the top and bottom of the domain and a constant rate of production (or consumption) is set in the biofilm domain. The entire domain is initialized with zero velocity and zero O_2. To take into account turbulence in the fluid domain, both eddy viscosity and eddy diffusivity are added to the molecular ones as estimated from the experimental data (considering an integral length scale of ~7% of the water depth) and equal to ~$1{\cdot}10^{-5}$. A turbulent Prandtl number of 1 is assumed as initial guess, prior to the optimization process [66]. The result is a constant eddy viscosity model, which is the simplest turbulence model attainable. Even though in reality the eddy viscosity decays toward zero at the fluid-biofilm interface, this simple model is sufficient to reproduce the sharp transition to a flat concentration profile from the biofilm to the outer flow.

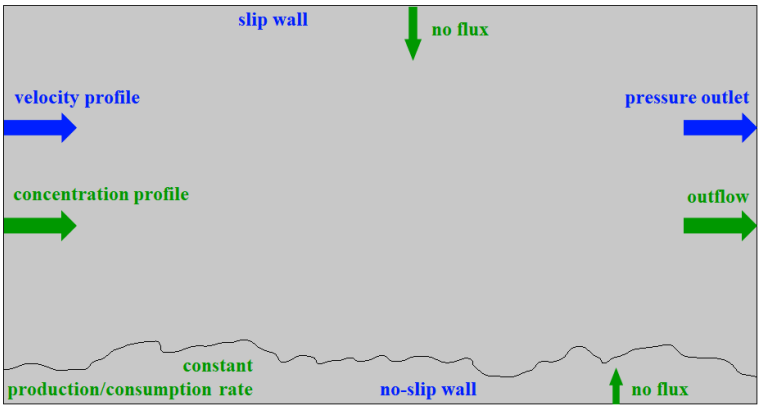

Figure 3.15 – Example of domain geometry (DDP) and boundary conditions of the computational model.

Governing equations The water flow at the top of the biofilm is intended as a steady, turbulent and incompressible. Therefore, we applied the Reynolds-averaged Navier–Stokes (RANS) and continuity equations. The transport of O_2 is also considered steady, since the comparison is done with experimental data collected at steady-state conditions. The equation of transport is:
$-D\nabla c + \overline{u}\nabla c = R$
where $\overline{u}$ is the flow velocity vector, c is the O_2 concentration [mol m^{-3}], D is the O_2 diffusivity in water [m^2 s^{-1}] and R is the production/consumption of O_2 in the biofilm [mol m^{-3} s^{-1}] [66].

Parameters optimization To optimize the parameter listed in Table 3.3, the Optimization Module in COMSOL Multiphysics 5.5 (COMSOL Multiphysics 5.5a, 2019) is employed. For each patch type and

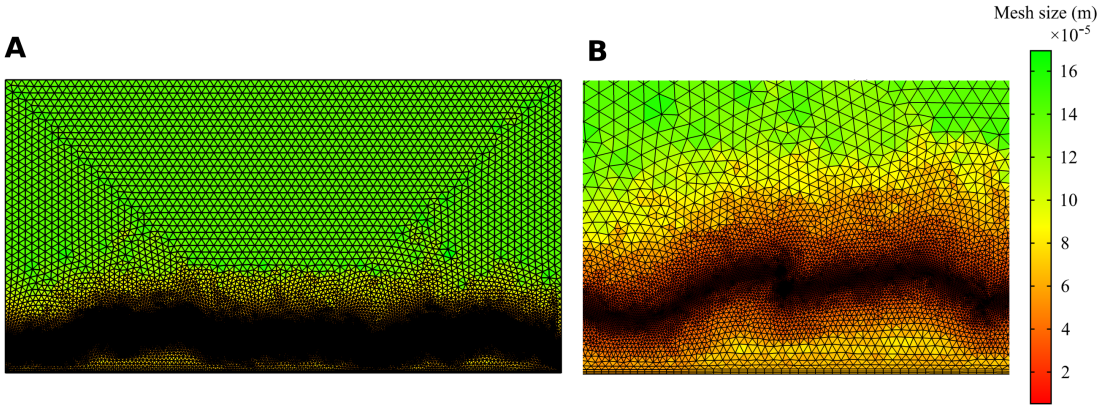

Figure 3.16 – Computational domain grid size in [m] (A), with the detail (B) of the biofilm discretization, in which both the refinement at the fluid-biofilm interface and the inflation layer are visible.

each flow and transport condition, one transect of O_2 concentration profiles is used as Least-Squares Objective features to create an objective function of the sum of squared differences between experimental data, fed into the model as a data file, and a corresponding expression calculated by the model. The model expression is evaluated using interpolation on the feature's selection, at measurement locations specified in the data file. Then the Nelder-Mead algorithm is used to estimate the parameters [148], which is one of the known algorithms for multidimensional unconstrained optimization without derivatives. To solve the classical optimization problem of minimizing a given non-linear function, it relies on a simplex of N+1 points, where N is the number of control variables. The solver does not use derivatives of the objective function, but geometrical reflections, expansions, and contractions to improve the points in the simplex. The optimality tolerance is set to $1{\cdot}10^{-4}$ for each controlled variable. The optimized parameters were validated on other O_2 concentration profiles transects of the same condition. The Pearson correlation between measured and predicted O_2 concentrations ranged between 0.12 and 0.95 under slow flow, and between 0.002 and 0.85 under fast flow. The fit between measured and predicted O_2 concentrations was especially low for transects across the very tall tufts that developed under fast flow. These structures' height exceeded the OCT imaging field, and the geometry used to model O_2 dynamics was therefore inaccurate. In addition, profiles in proximity of the boundary of the modeled domain presented a lower fit as a consequence of the velocity profile at the inflow boundary, which was measured without the biofilm. With downstream distance the velocity profile gradually adjusted to the given roughness conditions of the different biofilm transects and generally the quality of the fits improved accordingly. The values of the optimized parameters for each case are shown in (Table 3.3 and Table 3.4), while Figure 3.17 shows an example comparing the experimental profiles with the predicted ones. Table 3.6 reports the parameters ranges used in the optimization procedure. We calculated the average wall shear stress τ over the biofilm surface. The friction velocity is

$u^* = \sqrt{\tau/\rho}$

where ρ is the fluid density. The viscous length scale δ was estimated as

$\delta = \nu/u^*$

where ν is the kinematic viscosity of water. The DBL scale was estimated using

DBLscale= $\delta/\sqrt{Sc}$

where $Sc = \nu/D_w$ is the Schmidt number and D_w is the diffusion coefficient of oxygen in water.

Table 3.6 – Parameter ranges used in the optimization procedure for each patch type (CDB, DDP, and KDP), where D_{eff}/D_{aq} is the effective diffusivity of O_2 in the biofilm respect with water.

Parameter	DDP	CDB	KDP
Consumption rate [mol m^{-3} s^{-1}]	-2e^{-3} — -4e^{-4}	-2e^{-3} — -4e^{-4}	-2e^{-3} — -4e^{-4}
Production rate [mol m^{-3} s^{-1}]	1e^{-4} — 1e^{-2}	1e^{-4} — 1e^{-2}	1e^{-4} — 1e^{-2}
O_2 diffusivity (D_{eff}/D_{aq}) [-]	0.5 — 0.7	0.5 — 0.7	0.7 (0.8 for fast flow) — 1
Porosity [-]	0.04 — 0.63	0.04 — 0.63	0.04 — 0.63
Permeability [m^2]	1e^{-11} — 1e^{-8}	1e^{-11} — 1e^{-8}	1e^{-11} — 1e^{-8}
Turbulent Prandtl N. [-]	0.5 — 1	0.5 — 1	0.5 — 1
Eddy diffusivity [m^2 s^{-1}]	1e-5 — 1e^{-4}	1e-5 — 1e^{-4}	1e-5 — 1e^{-4}

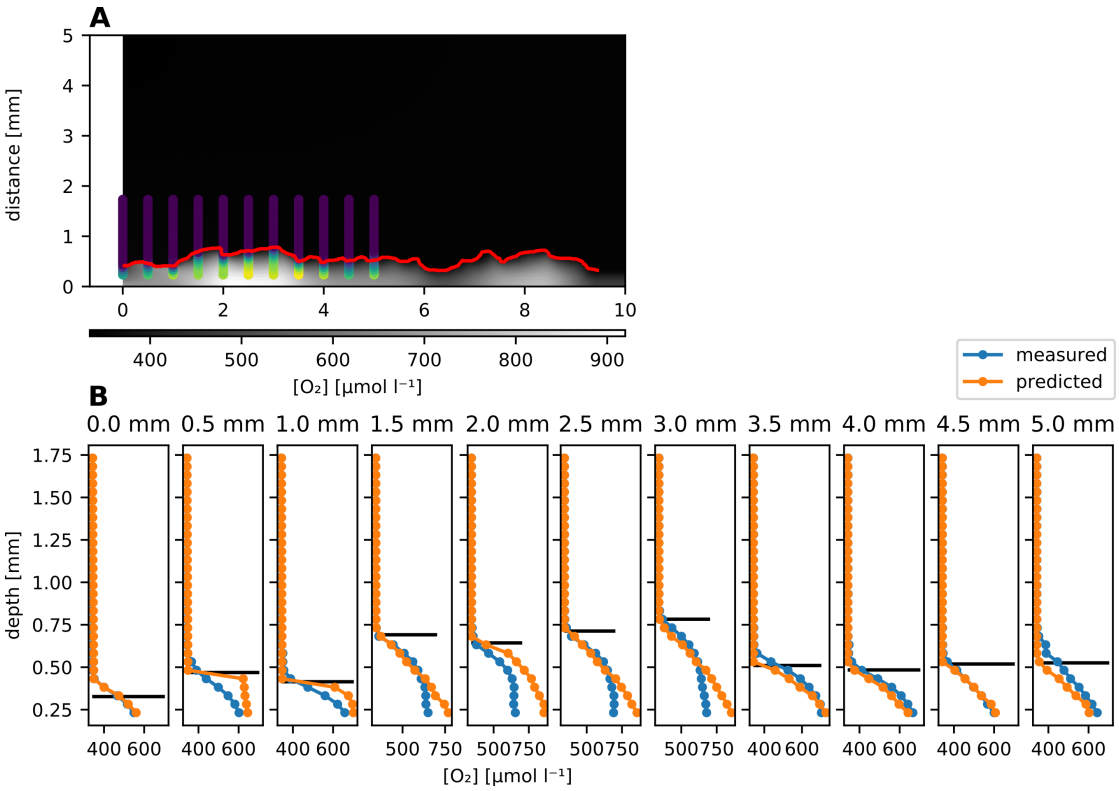

Figure 3.17 – Comparison between a measured and predicted transect of O_2 concentration profiles. The two-dimensional flow velocity and O_2 concentration fields around selected biofilm structures were modeled numerically. The modeled O_2 concentration field around and within a DDP imaged by OCT under slow flow is shown (A). The surface of the biofilm is indicated by the red line. The points indicate the locations in which the O_2 concentration was measured with a microsensor, color-coded based on the respective concentrations. The model was parametrized by optimizing the fit between predicted and measured O_2 concentrations (B).

Conclusions

Biofilms are complex, fascinating and fundamental communities for the Earth biosphere. Although miniaturized, they display an enormous complexity of ecological interactions that intertwine with multi-scale physical processes. Fluid dynamics, mass transfer and the cells metabolism interplay in these "active" physical systems, whose pivotal functions can not be explained neither by physics or microbial physiology independently. The global influences of biofilms emerge from a network of contributing processes that intrinsically link ecology, physics and biology, and are predictable only from their combined understanding. Phototrophic biofilms carpeting the bed of streams and rivers are yet another example of the contribution of biofilms and their physical properties to the global ecosystem. Benthic biofilms drive changes in the water chemistry, nutrient retention, productivity and biodiversity of river networks, which connect inland waters and soils to the oceans. Complex longitudinal gradients and allochthonous inputs result in the often unpredictable temporal and spatial linkage of stream metabolic regimes [15]. As an important link across spatial and temporal scales, the responses of benthic biofilm to abiotic cues could provide a tool to connect environmental drivers and the large-scale functioning of river networks. By expanding the current knowledge of the biofilms functioning to the context of complex phototrophic communities, this dissertation explores the transition between highly controlled laboratory conditions and natural benthic communities. A special focus has been put on the integrated influence of hydraulics and spatial architecture on biofilm functions, which may be instrumental in linking hydrological regime and ecological processes in rivers.

In the first publication from this dissertation, we developed an experimental setup combining several technologies for *in situ* characterization of complex phototrophic biofilms. The installation allowed for the cultivation of phototrophic biofilms in a large (1.5 m long), plexiglass flume and characterization of their meso-scale architecture by OCT. Thanks to a constant inflow of raw lake water, it permitted the investigation of *quasi*-natural dynamics, in which benthic communities are exposed to a constant immigration of diverse cells and propagules, as well as grazers and a complex water chemistry. The flat plexiglass surface enabled for the control of substrate roughness effects on biofilms morphogenesis. Furthermore, the funnel-like design of the flume implemented a continuous gradient in flow velocity and bed shear stress that decreased with the increasing width of the channel. This allowed for the elucidation of morphological trends associated with specific ranges of hydraulic conditions, in contrast with an approach involving discrete treatments. Although not originally conceived in this perspective, the flume could be used both as a hydraulic nozzle and a diffuser, with walls progressively narrowing or widening, respectively. This versatility enabled contrasting levels of turbulence intensity while maintaining the same overall discharge. To image the biofilm meso-scale structure, we combined a precision positioning robot and the automatic acquisition of OCT scans. This permitted the acquisition of OCT scans in a tiled pattern, thereby enlarging the spatial extent of OCT up to the meter scale. Further, this *semi*-automatic system allowed for the tracking of biofilms morphogenesis over time

and the gathering of large amounts of imaging data. To complete the setup, O_2 microsensors or a photographic camera could be mounted on the positioning robot, enabling the collection of integrated datasets to link structure and function in phototrophic biofilms.
The limitations of this experimental setup included seasonal changes in water quality, which limited the reproducibility of long-term experiments, and the absence of tools for the measurement of the near-bed hydraulics, which was instead numerically modeled. The integration of a PIV measuring system in the installation would significantly improve the opportunities offered by this setup.

In a second research paper, we deployed the described laboratory installation to observe the morphogenesis of a large rectangular patch of benthic biofilm (40 x 2.5 cm^2) over 15 days (temporal resolution of 3 days). We characterized by OCT a striking architectural differentiation along a relatively short gradient in hydraulic conditions. Under low shear stress, the biofilm developed into clumps separated by empty, uncolonized areas. Under high shear, a homogeneous carpet-like structure covered most of the available surface area and presented a faster rate in biovolume accrual. Intriguingly, the morphological gradient did not linearly follow the hydraulic gradient. Rather, a sharp shift in architectural features was observed around a break-point bed shear stress, which separated an area of the biofilm in which architecture was not significantly affected and a portion of the biofilm that responded strongly to the changing shear stress. The diverging architectures presented a similar community composition, suggesting that architectural plasticity, rather than diversity patterns, underlies the observed pattern. The OCT time-series also highlighted the dynamic behavior of the biofilm, featuring the displacement of structures in the flow direction, sloughing of entire biofilm clusters as well as the formation of ripples. These observations highlighted that, as observed in other biofilm systems [220;226], these dynamic behaviors may represent a relevant mean of biofilm dissemination in streams. The combination of O_2 micro-profiling and a fluid dynamics simulation evidenced that the biofilm structures modified patterns in flow velocity and mass transfer, driving the chemical patterning around and within the biofilm. Therefore, our work suggests that a tight trade-off between mechanical resistance and efficient mass transfer may determine the structure of complex phototrophic communities in their natural habitat. Further, we showed that a homogeneous benthic community can plastically adapt to changes in local shear stress, producing remarkable differences in their architecture and hence their functions. In a natural benthic environment, characterized by extensive heterogeneity in hydraulic conditions even within a few centimeters, this phenomenon could drive remarkable patchiness in biofilm architectures and responses, which may not necessarily be associated with different communities.
As a future direction, the causal link between hydraulic conditions and architectural differentiation should be further examined. For instance, the role of EPS production and grazing pressure in the architectural responses to shear are important research questions raised by our work. Lastly, further studies with higher temporal resolution would be important to rigorously quantify the temporal dynamics of biomass, such as sloughing and flow-induced displacement.

The last research paper in this dissertation investigates how patches of distinct communities ("patch types") determine the differentiation of the physico-chemical conditions in the phototrophic biofilm they compose. We integrated a dataset of OCT scans, macro-photographs, extensive O_2 micro-profiling, amplicon sequencing, and numerical simulations. We described the contrasting architectures of the patch types, their effect on the local flow and O_2 concentration patterns, and their contribution to the metabolism of the biofilm. Both internal structure and surface topology determined flow patterns around and within the biofilm, and drove substantial variations in the internal chemical gradients. Our results highlighted the pervasive role of advection in solute transport within benthic biofilms under turbulent flow conditions. Further, we found that biofilm metabolic rates differed by patch type, but also by flow condition. The contrasting rates of respiration and net photosynthesis of the contributing

patch types integrated into an overall positive net O_2 budget at the scale of the microbial landscape. Intriguingly, a higher flow velocity induced a decrease in the net production of O_2 of the biofilm. Our results highlight the role of patchiness in determining landscape-scale functions of phototrophic biofilms, with potential consequences for the metabolic regime of stream ecosystems.
This study suggests that microbial communities may modulate their metabolism in response to hydraulics. Biomass quantification, coupled with ezymatic activity assays to test for differences in respiratory and photosynthetic activity between communities and flow conditions would provide important mechanistic insights into the effect of flow on the biofilm metabolism. By numerical simulations, we showed that advection may provide a pivotal contribution to solute transport within benthic biofilms. This theoretical observation would require experimental confirmation, for instance by measuring the permeability of the inactivated biofilms and the flow patterns surrounding the biofilm surface by PIV.

From the integrated interpretation of the results above, we can draw the following conclusions:

1. biofilm meso-scale structure interacts with the surrounding hydrodynamics and drives the diversification of the physico-chemical microenvironment in complex phototrophic biofilms. This shows that mm-scale biofilm architectures reflect many spatial dynamics observed on a smaller scale and under controlled laboratory settings. Our results further highlight that the chemical heterogeneity within phototrophic communities is clearly dependent on light conditions, and hence highly dynamic in time. This should remain an important consideration when comparing ecological processes linked to spatial heterogeneity in photo- and heterotrophic biofilms.

2. hydraulics can influence the ecological features of phototrophic benthic biofilms. First, we showed that increased bed shear stress can determine the development of a more robust biofilm with an increased biovolume accumulation rate. Then, we observed how faster flow velocities could drive a shift towards a more heterotrophic metabolic regime of the benthic community.

3. external mass transfer resistance is a relatively weak driver of benthic biofilm structure and functions in natural streams. Both in a largely laminar and a fully turbulent flow regime, we observed that the thickness of the DBL surrounding the biofilm surface was thinner than ~100 μm. Hence, the hydraulic conditions of most streams and rivers probably homogenize the water chemistry up to very close to the biofilm surface, allowing for an efficient transfer of solutes across it.

4. contrary to what is commonly assumed in biofilm from other settings, our results suggest that significant fluid flow may occur within benthic biofilms. Both the strong hydraulic pressure and a relatively high biofilm permeability may contribute to this distinctive phenomenon, which homogenizes the biofilm chemical micro-environment and effectively alleviates internal mass transfer limitation. Hence, fluid motion within biofilm structures may represent an important and yet poorly explored driver of benthic processes.

5. contrasting communities and hydraulic conditions may determine highly variable architectural responses. Under a laminar-to-transitional flow regime, we observed a drastic architectural diversification of the same microbial community within a relatively short hydraulic gradient. Under a fully turbulent flow regime, we documented the architectural diversification of a benthic community mostly linked to community composition, with little influences from the flow regime. Therefore, our results indicate that within their natural habitat, the structural response of benthic communities to hydraulic conditions may be influenced by threshold effects, architectural plasticity, and community composition.

As mentioned above, these results inspired numerous additional hypotheses that could be tested in the future. Among these, the effect of internal advection should be especially taken into consideration. Given some discrepancies among published results, it would be beneficial to first experimentally test this phenomenon with different biofilm systems and hydraulic conditions. This would represent a necessary prerequisite to be able to investigate the potential role of internal fluid flow as driver of phenotypic heterogeneity and metabolic shifts within benthic biofilms. Furthermore, the effect of the community composition on architectural responses to fluid flow would be an important research topic for future studies. Conspicuous biodiversity patterns characterize river networks. A deeper understanding of the specificities and generalities in the microbial responses to hydraulics would be especially beneficial when attempting to predict metabolic responses to hydrological cues at the scale of river networks.

To conclude, in this dissertation we described the emergence of a variety of meso-scale structures and their complex interplay with biotic and abiotic factors in phototrophic biofilms. Just as ecosystem engineers described in large ecosystems, the formation of biofilms with prominent spatial features allows microorganisms to stably colonize and collectively modify the benthic habitat. Single cells achieve a stronger control on the local physico-chemical conditions, and increase their spatial impact. This permits them to interact with larger-scale phenomena, such as turbulent eddies and the momentum boundary layer. The multi-scale biotic processes that occur within a biofilm reflect to a large extent the nestedness of spatial scales in the convective and diffusive processes they are exposed to. Fluid dynamics emerges as a potent driver of the biofilm ecosystem, in a cascade of biophysical interactions across spatial scales. Water flow imposes a mechanical pressure on the biofilms and affects the rate of solutes exchange. On the other hand, it determines the relative importance of endogenous and exogenous fluxes, thereby affecting the "openness" of the system. Despite their large difference in spatial extent, biofilms and rivers are characterized by a common driver. Pervasive fluid motion set them apart from closer ecosystems, such as forests, in which progressive niche diversification allows for efficient utilization of available resources. The understanding of rivers and biofilms, and their integrated effects, may require consideration of the disproportionate and variable influence of exogenous inputs. Further, the impact of the community composition, the presence of threshold effects, and a fine hierarchy of spatial interactions should be taken into account to upscale local benthic processes to the scale of river networks.

Bibliography

[1] Alpkvist, E. and Klapper, I. (2007). Description of mechanical response including detachment using a novel particle model of biofilm/flow interaction. *Water Science and Technology*, 55(8-9):265–273.

[2] Arnon, S., Gray, K. A., and Packman, A. I. (2007). Biophysicochemical process coupling controls nitrate use by benthic biofilms. *Limnology and Oceanography*, 52(4):1665–1671.

[3] Asally, M., Kittisopikul, M., Rue, P., Du, Y., Hu, Z., Cagatay, T., Robinson, A. B., Lu, H., Garcia-Ojalvo, J., and Suel, G. M. (2012). Localized cell death focuses mechanical forces during 3D patterning in a biofilm. *Proceedings of the National Academy of Sciences*, 109(46):18891–18896.

[4] Atkinson, B. L., Grace, M. R., Hart, B. T., and Vanderkruk, K. E. N. (2008). Sediment instability affects the rate and location of primary production and respiration in a sand-bed stream. *Journal of the North American Benthological Society*, 27(3):581–592.

[5] Banin, E., Vasil, M. L., and Greenberg, E. P. (2005). Iron and Pseudomonas aeruginosa biofilm formation. *Proceedings of the National Academy of Sciences*, 102(31):11076–11081.

[6] Barral-Fraga, L., Martiñá-Prieto, D., Barral, M. T., Morin, S., and Guasch, H. (2018). Mutual interaction between arsenic and biofilm in a mining impacted river. *Science of The Total Environment*, 636:985–998.

[7] Battin, T. J., Besemer, K., Bengtsson, M. M., Romani, A. M., and Packmann, A. I. (2016). The ecology and biogeochemistry of stream biofilms. *Nature Reviews Microbiology*, 14(4):251–263.

[8] Battin, T. J., Kaplan, L. A., Denis Newbold, J., and Hansen, C. M. E. (2003a). Contributions of microbial biofilms to ecosystem processes in stream mesocosms. *Nature*, 426(6965):439–442.

[9] Battin, T. J., Kaplan, L. A., Findlay, S., Hopkinson, C. S., Marti, E., Packman, A. I., Newbold, J. D., and Sabater, F. (2008). Biophysical controls on organic carbon fluxes in fluvial networks. *Nature Geoscience*, 1(2):95–100.

[10] Battin, T. J., Kaplan, L. A., Newbold, J. D., Cheng, X., and Hansen, C. (2003b). Effects of Current Velocity on the Nascent Architecture of Stream Microbial Biofilms. *Applied and Environmental Microbiology*, 69(9):5443–5452.

[11] Battin, T. J., Luyssaert, S., Kaplan, L. A., Aufdenkampe, A. K., Richter, A., and Tranvik, L. J. (2009). The boundless carbon cycle. *Nature Geoscience*, 2(9):598–600.

[12] Battin, T. J., Sloan, W. T., Kjelleberg, S., Daims, H., Head, I. M., Curtis, T. P., and Eberl, L. (2007). Microbial landscapes: new paths to biofilm research. *Nature Reviews Microbiology*, 5(1):76–81.

[13] Beer, D. D. and Kühl, M. (2001). Interfacial microbial mats and biofilms. *The Benthic Boundary Layer*, 70(11):374–394.

[14] Berg, P., Risgaard-Petersen, N., and Rysgaard, S. (1998). Interpretation of measured concentration profiles in sediment pore water. *Limnology and Oceanography*, 43(7):1500–1510.

[15] Bernhardt, E. S., Heffernan, J. B., Grimm, N. B., Stanley, E. H., Harvey, J. W., Arroita, M., Appling, A. P., Cohen, M. J., McDowell, W. H., Hall, R. O., Read, J. S., Roberts, B. J., Stets, E. G., and Yackulic, C. B. (2017). The metabolic regimes of flowing waters. *Limnology and Oceanography*.

[16] Bernhardt, E. S., Likens, G. E., Buso, D. C., and Driscoll, C. T. (2003). In-stream uptake dampens effects of major forest disturbance on watershed nitrogen export. *Proceedings of the National Academy of Sciences*, 100(18):10304–10308.

[17] Besemer, K. (2015). Biodiversity, community structure and function of biofilms in stream ecosystems. *Research in Microbiology*, 166(10):774–781.

[18] Besemer, K., Hö Dl, I., Singer, G., and Battin, T. J. (2009a). Architectural differentiation reflects bacterial community structure in stream biofilms. *The ISME Journal*, 3:1318–1324.

[19] Besemer, K., Singer, G., Hödl, I., and Battin, T. J. (2009b). Bacterial community composition of stream biofilms in spatially variable-flow environments. *Applied and Environmental Microbiology*, 75(22):7189–7195.

[20] Besemer, K., Singer, G., Limberger, R., Chlup, A. K., Hochedlinger, G., Hödl, I., Baranyi, C., and Battin, T. J. (2007). Biophysical controls on community succession in stream biofilms. *Applied and Environmental Microbiology*, 73(15):4966–4974.

[21] Besemer, K., Singer, G., Quince, C., Bertuzzo, E., Sloan, W., and Battin, T. J. (2013). Headwaters are critical reservoirs of microbial diversity for fluvial networks. *Proceedings of the Royal Society of London B: Biological Sciences*, 280(1771).

[22] Beyenal, H. and Lewandowski, Z. (2002). Internal and External Mass Transfer in Biofilms Grown at Various Flow Velocities. *Biotechnology Progress*, 18(1):55–61.

[23] Biggs, B. J. F., Goring, D. G., and Nikora, V. I. (1998). Subsidy and stress responses of stream periphyton to grdients in water velocity as a function of community growth form. *Journal of Phycology*, 34(4):598–607.

[24] Biggs, B. J. F., Nikora, V. I., and Snelder, T. H. (2005). Linking scales of flow variability to lotic ecosystem structure and function. *River Research and Applications*, 21(2-3):283–298.

[25] Billings, N., Birjiniuk, A., Samad, T. S., Doyle, P. S., and Ribbeck, K. (2015). Material properties of biofilms—a review of methods for understanding permeability and mechanics. *Reports on Progress in Physics*, 78(3):036601.

[26] Bjarnsholt, T., Alhede, M., Alhede, M., Eickhardt-Sørensen, S. R., Moser, C., Kühl, M., Jensen, P. Ø., and Høiby, N. (2013). The in vivo biofilm. *Trends in Microbiology*, 21(9):466–474.

[27] Blauert, F., Horn, H., and Wagner, M. (2015). Time-resolved biofilm deformation measurements using optical coherence tomography. *Biotechnology and Bioengineering*, 112(9):1893–1905.

[28] Boano, F., Harvey, J. W., Marion, A., Packman, A. I., Revelli, R., Ridolfi, L., and Wörman, A. (2014). Hyporheic flow and transport processes: Mechanisms, models, and biogeochemical implications. *Reviews of Geophysics*, 52(4):603–679.

[29] Böhme, A., Risse-Buhl, U., and Küsel, K. (2009). Protists with different feeding modes change biofilm morphology. *FEMS Microbiology Ecology*, 69(2):158–169.

[30] Bolyen, E., Rideout, J. R., Dillon, M. R., Bokulich, N. A., Abnet, C. C., Al-Ghalith, G. A., Alexander, H., Alm, E. J., Arumugam, M., Asnicar, F., Bai, Y., Bisanz, J. E., Bittinger, K., Brejnrod, A., Brislawn, C. J., Brown, C. T., Callahan, B. J., Caraballo-Rodríguez, A. M., Chase, J., Cope, E. K., Da Silva, R., Diener, C., Dorrestein, P. C., Douglas, G. M., Durall, D. M., Duvallet, C., Edwardson, C. F., Ernst, M., Estaki, M., Fouquier, J., Gauglitz, J. M., Gibbons, S. M., Gibson, D. L., Gonzalez, A., Gorlick, K., Guo, J., Hillmann, B., Holmes, S., Holste, H., Huttenhower, C., Huttley, G. A., Janssen, S., Jarmusch, A. K., Jiang, L., Kaehler, B. D., Kang, K. B., Keefe, C. R., Keim, P., Kelley, S. T., Knights, D., Koester, I., Kosciolek, T., Kreps, J., Langille, M. G. I., Lee, J., Ley, R., Liu, Y.-X., Loftfield, E., Lozupone, C., Maher, M., Marotz, C., Martin, B. D., McDonald, D., McIver, L. J., Melnik, A. V., Metcalf, J. L., Morgan, S. C., Morton, J. T., Naimey, A. T., Navas-Molina, J. A., Nothias, L. F., Orchanian, S. B., Pearson, T., Peoples, S. L., Petras, D., Preuss, M. L., Pruesse, E., Rasmussen, L. B., Rivers, A., Robeson, M. S., Rosenthal, P., Segata, N., Shaffer, M., Shiffer, A., Sinha, R., Song, S. J., Spear, J. R., Swafford, A. D., Thompson, L. R., Torres, P. J., Trinh, P., Tripathi, A., Turnbaugh, P. J., Ul-Hasan, S., van der Hooft, J. J. J., Vargas, F., Vázquez-Baeza, Y., Vogtmann, E., von Hippel, M., Walters, W., Wan, Y., Wang, M., Warren, J., Weber, K. C., Williamson, C. H. D., Willis, A. D., Xu, Z. Z., Zaneveld, J. R., Zhang, Y., Zhu, Q., Knight, R., and Caporaso, J. G. (2019). Reproducible, interactive, scalable and extensible microbiome data science using QIIME 2. *Nature Biotechnology*, 37(8):852–857.

[31] Branda, S. S., González-Pastor, J. E., Ben-Yehuda, S., Losick, R., and Kolter, R. (2001). Fruiting body formation by Bacillus subtilis. *Proceedings of the National Academy of Sciences of the United States of America*, 98(20):11621–11626.

[32] Brentnall, S. J., Richards, K. J., Brindley, J., and Murphy, E. (2003). Plankton patchiness and its effect on larger-scale productivity. *Journal of Plankton Research*, 25(2):121–140.

[33] Bridier, A., Piard, J.-C., Pandin, C., Labarthe, S., Dubois-Brissonnet, F., and Briandet, R. (2017). Spatial Organization Plasticity as an Adaptive Driver of Surface Microbial Communities. *Frontiers in Microbiology*, 8.

[34] Bruckner, C. G., Rehm, C., Grossart, H. P., and Kroth, P. G. (2011). Growth and release of extracellular organic compounds by benthic diatoms depend on interactions with bacteria. *Environmental Microbiology*, 13(4):1052–1063.

[35] Burliga, A. L. and Kociolek, J. P. (2016). Diatoms (Bacillariophyta) in Rivers. In *River Algae*, pages 93–128. Springer International Publishing, Cham.

[36] Calders, K., Phinn, S., Ferrari, R., Leon, J., Armston, J., Asner, G. P., and Disney, M. (2020). 3D Imaging Insights into Forests and Coral Reefs. *Trends in Ecology & Evolution*, 35(1):6–9.

[37] Callahan, B. J., McMurdie, P. J., Rosen, M. J., Han, A. W., Johnson, A. J. A., and Holmes, S. P. (2016). DADA2: High-resolution sample inference from Illumina amplicon data. *Nature Methods*, 13(7):581–583.

[38] Cardinale, B. J., Hillebrand, H., and Charles, D. F. (2006). Geographic patterns of diversity in streams are predicted by a multivariate model of disturbance and productivity. *Journal of Ecology*, 94(3):609–618.

[39] Cardinale, B. J. and Palmer, M. A. (2002). Disturbance moderates biodiversity-ecosystem function relationships: Experimental evidence from caddisflies in stream mesocosms. *Ecology*, 83(7):1915–1927.

[40] Cardinale, B. J., Palmer, M. A., and Collins, S. L. (2002). Species diversity enhances ecosystem functioning through interspecific facilitation. *Nature*, 415(6870):426–429.

[41] Chambless, J. D. and Stewart, P. S. (2007). A three-dimensional computer model analysis of three hypothetical biofilm detachment mechanisms. *Biotechnology and Bioengineering*, 97(6):1573–1584.

[42] Cogan, N. G., Li, J., Fabbri, S., and Stoodley, P. (2018). Computational Investigation of Ripple Dynamics in Biofilms in Flowing Systems. *Biophysical Journal*, 115(7):1393–1400.

[43] Cole, J. J., Prairie, Y. T., Caraco, N. F., McDowell, W. H., Tranvik, L. J., Striegl, R. G., Duarte, C. M., Kortelainen, P., Downing, J. A., Middelburg, J. J., and Melack, J. (2007). Plumbing the global carbon cycle: Integrating inland waters into the terrestrial carbon budget. *Ecosystems*.

[44] Conlon, B. P., Rowe, S. E., and Lewis, K. (2015). Persister cells in biofilm associated infections. *Advances in Experimental Medicine and Biology*.

[45] Costerton, J. W., Cheng, K. J., Geesey, G. G., Ladd, T. I., Nickel, J. C., Dasgupta, M., and Marrie, T. J. (1987). Bacterial Biofilms in Nature and Disease. *Annual Review of Microbiology*, 41(1):435–464.

[46] Costerton, J. W., Stewart, P. S., and Greenberg, E. P. (1999). Bacterial Biofilms: A Common Cause of Persistent Infections. *Science*, 284(5418):1318–1322.

[47] Cremer, J., Segota, I., Yang, C.-y., Arnoldini, M., Sauls, J. T., Zhang, Z., Gutierrez, E., Groisman, A., and Hwa, T. (2016). Effect of flow and peristaltic mixing on bacterial growth in a gut-like channel. *Proceedings of the National Academy of Sciences*, 113(41):11414–11419.

[48] Davit, Y., Byrne, H., Osborne, J., Pitt-Francis, J., Gavaghan, D., and Quintard, M. (2013). Hydrodynamic dispersion within porous biofilms. *Physical Review E - Statistical, Nonlinear, and Soft Matter Physics*, 87(1):24–29.

[49] De Beer, D., Stoodley, P., and Lewandowski, Z. (1994). Liquid flow in heterogeneous biofilms. *Biotechnology and Bioengineering*.

[50] De Beer, D., Stoodley, P., and Lewandowski, Z. (1996). Liquid flow and mass transport in heterogeneous biofilms. *Water Research*, 30(11):2761–2765.

[51] De Beer, D., Stoodley, P., Roe, F., and Lewandowski, Z. (1994). Effects of biofilm structures on oxygen distribution and mass transport. *Biotechnology and Bioengineering*, 43(11):1131–1138.

[52] De Philippis, R., Colica, G., and Micheletti, E. (2011). Exopolysaccharide-producing cyanobacteria in heavy metal removal from water: molecular basis and practical applicability of the biosorption process. *Applied Microbiology and Biotechnology*, 92(4):697–708.

[53] Deng, W., Cardenas, M. B., Kirk, M. F., Altman, S. J., and Bennett, P. C. (2013). Effect of permeable biofilm on micro-and macro-scale flow and transport in bioclogged pores. *Environmental Science and Technology*, 47(19):11092–11098.

[54] Depetris, A., Peter, H., Bordoloi, A., Bernard, H., Niayifar, A., Kühl, M., de Anna, P., and Battin, T. (2021). Morphogenesis and oxygen dynamics in phototrophic biofilms growing across a gradient of hydraulic conditions. *iScience*.

[55] Depetris, A., Wiedmer, A., Wagner, M., Schäfer, S., Battin, T. J., and Peter, H. (2019). Automated 3D Optical Coherence Tomography to Elucidate Biofilm Morphogenesis Over Large Spatial Scales. *Journal of Visualized Experiments*, (150).

[56] Derlon, N., Grütter, A., Brandenberger, F., Sutter, A., Kuhlicke, U., Neu, T. R., and Morgenroth, E. (2016). The composition and compression of biofilms developed on ultrafiltration membranes determine hydraulic biofilm resistance. *Water Research*, 102:63–72.

[57] Derlon, N., Peter-Varbanets, M., Scheidegger, A., Pronk, W., and Morgenroth, E. (2012). Predation influences the structure of biofilm developed on ultrafiltration membranes. *Water Research*, 46(10):3323–3333.

[58] Dietrich, L. E. P., Okegbe, C., Price-Whelan, A., Sakhtah, H., Hunter, R. C., and Newman, D. K. (2013). Bacterial Community Morphogenesis Is Intimately Linked to the Intracellular Redox State. *Journal of Bacteriology*, 195(7):1371–1380.

[59] Dopheide, A., Lear, G., Stott, R., and Lewis, G. (2008). Molecular Characterization of Ciliate Diversity in Stream Biofilms. *Applied and Environmental Microbiology*, 74(6):1740–1747.

[60] Drescher, K., Dunkel, J., Nadell, C. D., van Teeffelen, S., Grnja, I., Wingreen, N. S., Stone, H. A., and Bassler, B. L. (2016). Architectural transitions in Vibrio cholerae biofilms at single-cell resolution. *Proceedings of the National Academy of Sciences*, 113(14):E2066–E2072.

[61] Dreszer, C., Vrouwenvelder, J., Paulitsch-Fuchs, A., Zwijnenburg, A., Kruithof, J., and Flemming, H.-C. (2013). Hydraulic resistance of biofilms. *Journal of Membrane Science*, 429:436–447.

[62] Dreszer, C., Wexler, A., Drusová, S., Overdijk, T., Zwijnenburg, A., Flemming, H.-C., Kruithof, J., and Vrouwenvelder, J. (2014). In-situ biofilm characterization in membrane systems using Optical Coherence Tomography: Formation, structure, detachment and impact of flux change. *Water Research*, 67:243–254.

[63] Drexler, W. and Fujimoto, J. G. (2008). *Optical Coherence Tomography Technology and Applications*, volume 7156.

[64] Duddu, R., Chopp, D. L., and Moran, B. (2009). A two-dimensional continuum model of biofilm growth incorporating fluid flow and shear stress based detachment. *Biotechnology and Bioengineering*, 103(1):92–104.

[65] Dunsmore, B. C., Jacobsen, A., Hall-Stoodley, L., Bass, C. J., Lappin-Scott, H. M., and Stoodley, P. (2002). The influence of fluid shear on the structure and material properties of sulphate-reducing bacterial biofilms. *Journal of Industrial Microbiology and Biotechnology*, 29(6):347–353.

[66] Durbin, P. A. and Medic, G. (2007). *Fluid Dynamics with a Computational Perspective*. Cambridge University Press, Cambridge.

[67] Dzubakova, K., Peter, H., Bertuzzo, E., Juez, C., Franca, M. J., Rinaldo, A., and Battin, T. J. (2018). Environmental heterogeneity promotes spatial resilience of phototrophic biofilms in streambeds. *Biology Letters*, 14(10):20180432.

[68] Eberl, H., Picioreanu, C., Heijnen, J., and van Loosdrecht, M. (2000). A three-dimensional numerical study on the correlation of spatial structure, hydrodynamic conditions, and mass transfer and conversion in biofilms. *Chemical Engineering Science*, 55(24):6209–6222.

[69] Ensign, S. H. and Doyle, M. W. (2006). Nutrient spiraling in streams and river networks. *Journal of Geophysical Research: Biogeosciences*, 111(4):1–13.

[70] Epping, E. and Kühl, M. (2000). The responses of photosynthesis and oxygen consumption to short-term changes in temperature and irradiance in a cyanobacterial mat (Ebro Delta, Spain). *Environmental Microbiology*, 2(4):465–474.

[71] Espeland, E., Francoeur, S., and Wetzel, R. (2001). Influence of Algal Photosynthesis on Biofilm Bacterial Production and Associated Glucosidase and Xylosidase Activities. *Microbial Ecology*, 42(4):524–530.

[72] Fercher, A. F. (2010). Optical coherence tomography – development, principles, applications. *Zeitschrift für Medizinische Physik*, 20(4):251–276.

[73] Fierer, N., Morse, J. L., Berthrong, S. T., Bernhardt, E. S., and Jackson, R. B. (2007). Environmental controls on the landscape-scale biogeography of stream bacterial communities. *Ecology*.

[74] Findlay, R. H. and Battin, T. J. (2015). The Microbial Ecology of Benthic Environments. In *Manual of Environmental Microbiology*.

[75] Flemming, H.-c. and Wingender, J. (2010). The biofilm matrix. *Nature Reviews Microbiology*, 8(9):623–633.

[76] Flemming, H.-C., Wingender, J., Szewzyk, U., Steinberg, P., Rice, S. A., and Kjelleberg, S. (2016). Biofilms: an emergent form of bacterial life. *Nature Reviews Microbiology*, 14(9):563–575.

[77] Flemming, H.-C. and Wuertz, S. (2019). Bacteria and archaea on Earth and their abundance in biofilms. *Nature Reviews Microbiology*, 17(4):247–260.

[78] Fortunato, L., Jeong, S., Wang, Y., Behzad, A. R., and Leiknes, T. (2016). Integrated approach to characterize fouling on a flat sheet membrane gravity driven submerged membrane bioreactor. *Bioresource Technology*, 222:335–343.

[79] Fortunato, L. and Leiknes, T. (2017). In-situ biofouling assessment in spacer filled channels using optical coherence tomography (OCT): 3D biofilm thickness mapping. *Bioresource Technology*, 229:231–235.

[80] Fortunato, L., Qamar, A., Wang, Y., Jeong, S., and Leiknes, T. (2017). In-situ assessment of biofilm formation in submerged membrane system using optical coherence tomography and computational fluid dynamics. *Journal of Membrane Science*, 521:84–94.

[81] Franklin, G., Mariño-Tapia, I., and Torres-Freyermuth, A. (2013). Effects of reef roughness on wave setup and surf zone currents. *Journal of Coastal Research*.

[82] Fujimoto, J. G., Pitris, C., Boppart, S. A., and Brezinski, M. E. (2000). Optical coherence tomography: an emerging technology for biomedical imaging and optical biopsy. *Neoplasia (New York, N.Y.)*, 2(1-2):9–25.

[83] Fukuda, M., Matsuyama, J., Katano, T., Nakano, S. I., and Dazzo, F. (2006). Assessing primary and bacterial production rates in biofilms on pebbles in Ishite Stream, Japan. *Microbial Ecology*.

[84] Geesey, G. G., Mutch, R., Costerton, J. W., and Green, R. B. (1978). Sessile bacteria: An important component of the microbial population in small mountain streams. *Limnology and Oceanography*.

[85] Gessner, M., Gulis, V., Kuehn, K. A., Chauvet, E., and Suberkropp, K. (2007). *Fungal Decomposers of Plant Litter in Aquatic Ecosystems*, pages 301–324. Springer Berlin Heidelberg, Berlin, Heidelberg.

[86] Glud, R. N., Gundersen, J. K., and Ramsing, N. B. (2000). Electrochemical and optical oxygen microsensors for in situ measurements.

[87] Glud, R. N., Ramsing, N. B., and Revsbech, N. P. (1992). PHOTOSYNTHESIS AND PHOTOSYNTHESIS-COUPLED RESPIRATION IN NATURAL BIOFILMS QUANTIFIED WITH OXYGEN MICROSENSORS. *Journal of Phycology*, 28(1):51–60.

[88] González-Rivero, M., Harborne, A. R., Herrera-Reveles, A., Bozec, Y. M., Rogers, A., Friedman, A., Ganase, A., and Hoegh-Guldberg, O. (2017). Linking fishes to multiple metrics of coral reef structural complexity using three-dimensional technology. *Scientific Reports*.

[89] Gordon, V., Bakhtiari, L., and Kovach, K. (2019). From molecules to multispecies ecosystems: The roles of structure in bacterial biofilms. *Physical Biology*, 16(4).

[90] Graba, M., Sauvage, S., Moulin, F. Y., Urrea, G., Sabater, S., and Sanchez-Pérez, J. M. (2013). Interaction between local hydrodynamics and algal community in epilithic biofilm. *Water Research*, 47(7):2153–2163.

[91] Grant, S. B., Gomez Velez, J. D., Ghisalberti, M., Guymer, I., Boano, F., Roche, K., and Harvey, J. (2020). A One Dimensional Model for Turbulent Mixing in the Benthic Biolayer of Stream and Coastal Sediments. *Water Resources Research*, 56(12).

[92] Green, D. G. and Sadedin, S. (2005). Interactions matter—complexity in landscapes and ecosystems. *Ecological Complexity*, 2(2):117–130.

[93] Grötzschel, S. and De Beer, D. (2002). Effect of oxygen concentration on photosynthesis and respiration in two hypersaline microbial mats. *Microbial Ecology*.

[94] Guilbaud, M., Piveteau, P., Desvaux, M., Brisse, S., and Briandet, R. (2015). Exploring the diversity of Listeria monocytogenes biofilm architecture by high-throughput confocal laser scanning microscopy and the predominance of the honeycomb-like morphotype. *Applied and Environmental Microbiology*, 81(5):1813–1819.

[95] Guimerà, X., Dorado, A. D., Bonsfills, A., Gabriel, G., Gabriel, D., and Gamisans, X. (2016). Dynamic characterization of external and internal mass transport in heterotrophic biofilms from microsensors measurements. *Water Research*, 102:551–560.

[96] Haack, T. and McFeters, G. (1982). Nutritional relationships amoung microorganisms in an epilithic bifilm community. *Microbial ecology*, 8(2):115–126.

[97] Haisch, C. and Niessner, R. (2007). Visualisation of transient processes in biofilms by optical coherence tomography. *Water Research*, 41(11):2467–2472.

[98] Hall-Stoodley, L., Costerton, J. W., and Stoodley, P. (2004). Bacterial biofilms: from the Natural environment to infectious diseases. *Nature Reviews Microbiology*, 2(2):95–108.

[99] Hamed, K. H. and Ramachandra Rao, A. (1998). A modified Mann-Kendall trend test for autocorrelated data. *Journal of Hydrology*, 204(1-4):182–196.

[100] Hao, O. J., Richard, M. G., Jenkins, D., and Blanch, H. W. (1983). The half saturation coefficient for dissolved oxygen: A dynamic method for its determination and its effect on dual species competition. *Biotechnology and Bioengineering*.

[101] Haralick, R. M., Shanmugam, K., and Dinstein, I. (1973). Textural Features for Image Classification. *IEEE Transactions on Systems, Man, and Cybernetics*, SMC-3(6):610–621.

[102] Hart, D. D. and Finelli, C. M. (1999). Physical-Biological Coupling in Streams: The Pervasive Effects of Flow on Benthic Organisms. *Annual Review of Ecology and Systematics*, 30(1):363–395.

[103] Haynes, K., Hofmann, T. A., Smith, C. J., Ball, A. S., Underwood, G. J. C., and Osborn, A. M. (2007). Diatom-derived carbohydrates as factors affecting bacterial community composition in estuarine sediments. *Applied and Environmental Microbiology*, 73(19):6112–6124.

[104] Hintz, W. D. and Wellnitz, T. (2013). Current velocity influences the facilitation and removal of algae by stream grazers. *Aquatic Ecology*, 47(2):235–244.

[105] Hondzo, M. and Wang, H. (2002). Effects of turbulence on growth and metabolism of periphyton in a laboratory flume. *Water Resources Research*, 38(12):13–1–13–9.

[106] Horn, H. and Morgenroth, E. (2006). Transport of oxygen, sodium chloride, and sodium nitrate in biofilms. *Chemical Engineering Science*, 61(5):1347–1356.

[107] Horner, R. R., Welch, E. B., Seeley, M. R., and Jacoby, J. M. (1990). Responses of periphyton to changes in current velocity, suspended sediment and phosphorus concentration. *Freshwater Biology*, 24(2):215–232.

[108] House, W. A. (2003). Geochemical cycling of phosphorus in rivers. *Applied Geochemistry*, 18(5):739–748.

[109] Huang, D., Swanson, E. A., Lin, C. P., Schuman, J. S., Stinson, W. G., Chang, W., Hee, M. R., Flotte, T., Gregory, K., Puliafito, C. A., and Fujimoto, J. G. (1991). Optical coherence tomography. *Science*.

[110] Hunt, S. M., Werner, E. M., Huang, B., Hamilton, M. A., and Stewart, P. S. (2004). Hypothesis for the Role of Nutrient Starvation in Biofilm Detachment. *Applied and Environmental Microbiology*, 70(12):7418–7425.

[111] Jacquet, S., Miki, T., Noble, R., Peduzzi, P., and Wilhelm, S. (2010). Viruses in aquatic ecosystems: important advancements of the last 20 years and prospects for the future in the field of microbial oceanography and limnology. *Advances in Oceanography and Limnology*, 1(1):97–141.

[112] Jafari, M., Desmond, P., van Loosdrecht, M. C., Derlon, N., Morgenroth, E., and Picioreanu, C. (2018). Effect of biofilm structural deformation on hydraulic resistance during ultrafiltration: A numerical and experimental study. *Water Research*, 145:375–387.

[113] Jensen, J. (1989). Photosynthesis and respiration of a diatom biofilm cultured in a new gradient growth chamber. *FEMS Microbiology Letters*, 62(1):29–38.

[114] Johnson, N. K. and Richardson, L. F. (1922). Weather Prediction by Numerical Process. *The Mathematical Gazette*.

[115] Jorgensen, B. B., Revsbech, N. P., and Cohen, Y. (1983). Photosynthesis and structure of benthic microbial mats: Microelectrode and SEM studies of four cyanobacterial communities1. *Limnology and Oceanography*, 28(6):1075–1093.

[116] Kapellos, G. E., Alexiou, T. S., and Payatakes, A. C. (2007). Hierarchical simulator of biofilm growth and dynamics in granular porous materials. *Advances in Water Resources*, 30(6-7):1648–1667.

[117] Kaplan, L. and Newbold, J. (2003). The Role of Monomers in Stream Ecosystem Metabolism. In *Aquatic Ecosystems*.

[118] Katano, I., Mitsuhashi, H., Isobe, Y., Sato, H., and Oishi, T. (2005). Reach-Scale Distribution Dynamics of a Grazing Stream Insect, Micrasema quadriloba Martynov (Brachycentridae, Trichoptera), in Relation to Current Velocity and Periphyton Abundance. *Zoological Science*, 22(8):853–860.

[119] Kearns, D. B. (2007). Division of labour during Bacillus subtilis biofilm formation. *Molecular Microbiology*, 67(2):229–231.

[120] Kirchman, D. L., Dittel, A. I., Findlay, S. E., and Fischer, D. (2004). Changes in bacterial activity and community structure in response to dissolved organic matter in the Hudson River, New York. *Aquatic Microbial Ecology*.

[121] Kohušová, K., Havel, L., Vlasák, P., and Tonika, J. (2011). A long-term survey of heavy metals and specific organic compounds in biofilms, sediments, and surface water in a heavily affected river in the Czech Republic. *Environmental Monitoring and Assessment*, 174(1-4):555–572.

[122] Kolmogorov, A. N. (2010). The local structure of turbulence in incompressible viscous fluid for very large Reynolds numbers. *Proceedings of The Royal Society*.

[123] Kühl, M. and Fenchel, T. (2000). Bio-optical Characteristics and the Vertical Distribution of Photosynthetic Pigments and Photosynthesis in an Artificial Cyanobacterial Mat. *Microbial Ecology*, 40(2):94–103.

[124] Kühl, M., Glud, R. N., Ploug, H., and Ramsing, N. B. (1996). Microenvironmental control of photosyntehsis and photosynthesis-coupled respiration in an epilithic cyanobacterial biofilm. *Journal of Phycology*, 32:799–812.

[125] Kühl, M. and Polerecky, L. (2008). Functional and structural imaging of phototrophic microbial communities and symbioses. *Aquatic Microbial Ecology*, 53(1):99–118.

[126] Kundu, P. K., Cohen, I. M., and Dowling, D. R. (2016). Boundary Layers and Related Topics. In *Fluid Mechanics*, pages 469–532. Elsevier.

[127] Larned, S. T. (2010). A prospectus for periphyton: Recent and future ecological research. *Journal of the North American Benthological Society*.

[128] Larned, S. T., Nikora, V. I., and Biggs, B. J. F. (2004). Mass-transfer-limited nitrogen and phosphorus uptake by stream periphyton: A conceptual model and experimental evidence. *Limnology and Oceanography*, 49(6):1992–2000.

[129] Lawrence, J. R. and Neu, T. R. (2003). Microscale analyses of the formation and nature of microbial biofilm communities in river systems. *Reviews in Environmental Science and Biotechnology*.

[130] Lear, G., Turner, S. J., and Lewis, G. D. (2009). Effect of light regimes on the utilisation of an exogenous carbon source by freshwater biofilm bacterial communities. *Aquatic Ecology*.

[131] Lee, H.-C., Liu, J. J., Sheikine, Y., Aguirre, A. D., Connolly, J. L., and Fujimoto, J. G. (2013). Ultrahigh speed spectral-domain optical coherence microscopy. *Biomedical Optics Express*, 4(8):1236.

[132] Lewandowski, Z. (2000). Notes on biofilm porosity. *Water Research*, 34(9):2620–2624.

[133] Lewandowski, Z. and Beyenal, H. (2013). *Fundamentals of Biofilm Research*. CRC Press.

[134] Li, C., Wagner, M., Lackner, S., and Horn, H. (2016). Assessing the influence of biofilm surface roughness on mass transfer by combining optical coherence tomography and two-dimensional modeling. *Biotechnology and Bioengineering*, 113(5):989–1000.

[135] Lloyd, D. P. and Allen, R. J. (2015). Competition for space during bacterial colonization of a surface. *Journal of The Royal Society Interface*, 12(110):20150608.

[136] Ludwig, J. A., Wiens, J. A., and Tongway, D. J. (2000). A Scaling Rule for Landscape Patches and How It Applies to Conserving Soil Resources in Savannas. *Ecosystems*, 3(1):84–97.

[137] Luo, J., Chen, H., Han, X., Sun, Y., Yuan, Z., and Guo, J. (2017). Microbial community structure and biodiversity of size-fractionated granules in a partial nitritation–anammox process. *FEMS Microbiology Ecology*, 93(6).

[138] Lyon, D. R. and Ziegler, S. E. (2009). Carbon cycling within epilithic biofilm communities across a nutrient gradient of headwater streams. *Limnology and Oceanography*, 54(2):439–449.

[139] Manz, B., Volke, F., Goll, D., and Horn, H. (2005). Investigation of biofilm structure, flow patterns and detachment with magnetic resonance imaging. *Water Science and Technology*, 52(7):1–6.

[140] Manz, W., Wendt-Potthoff, K., Neu, T. R., Szewzyk, U., and Lawrence, J. R. (1999). Phylogenetic composition, spatial structure, and dynamics of lotic bacterial biofilms investigated by fluorescent in situ hybridization and confocal laser scanning microscopy. *Microbial Ecology*.

[141] McDonogh, R., Schaule, G., and Flemming, H.-C. (1994). The permeability of biofouling layers on membranes. *Journal of Membrane Science*, 87(1-2):199–217.

[142] Meleppat, R. K., Shearwood, C., Keey, S. L., and Matham, M. V. (2016). Quantitative optical coherence microscopy for the in situ investigation of the biofilm. *Journal of Biomedical Optics*, 21(12):127002.

[143] Menter, F. R. (1993). *Zonal two equation kappa-omega turbulence models for aerodynamic flows*. Provided by the SAO/NASA Astrophysics Data System.

[144] Milferstedt, K., Pons, M.-N., and Morgenroth, E. (2009). Analyzing characteristic length scales in biofilm structures. *Biotechnology and Bioengineering*, 102(2):368–379.

[145] Morgenroth, E. and Milferstedt, K. (2009). Biofilm engineering: linking biofilm development at different length and time scales. *Reviews in Environmental Science and Bio/Technology*, 8(3):203–208.

[146] Muggeo, V. M. R. (2008). segmented: An R package to Fit Regression Models with Broken-Line Relationships. *R NEWS*, 8/1(1609-3631):20—-25.

[147] Nadell, C. D., Xavier, J. B., and Foster, K. R. (2009). The sociobiology of biofilms. *FEMS Microbiology Reviews*, 33(1):206–224.

[148] Nelder, J. A. and Mead, R. (1965). A Simplex Method for Function Minimization. *The Computer Journal*.

[149] Neu, T. R. and Lawrence, J. R. (2006). Development and structure of microbial biofilms in river water studied by confocal laser scanning microscopy. *FEMS Microbiology Ecology*, 24(1):11–25.

[150] Neu, T. R. and Lawrence, J. R. (2015). Innovative techniques, sensors, and approaches for imaging biofilms at different scales. *Trends in Microbiology*, 23(4):233–242.

[151] Niederdorfer, R., Peter, H., and Battin, T. J. (2016). Attached biofilms and suspended aggregates are distinct microbial lifestyles emanating from differing hydraulics. *Nature Microbiology*, 1(12):16178.

[152] Nikora, V. (2010). Hydrodynamics of aquatic ecosystems : An interface between ecology, biomechanics and environmental fluid mechanics. *River Research and Applications*, 26(4):367–384.

[153] Nøhr Glud, R., Gundersen, J. K., Barker Jørgensen, B., Revsbech, N. P., and Schulz, H. D. (1994). Diffusive and total oxygen uptake of deep-sea sediments in the eastern South Atlantic Ocean: in situ and laboratory measurements. *Deep-Sea Research Part I*.

[154] Oksanen, J., Blanchet, F., Friendly, M., Kindt, R., Legendre, P., McGlinn, D., Minchin, P., O'hara, R., Simpson, G., Solymos, P., and Stevens, M. (2016). vegan: Community Ecology Package.

[155] Palmer, M. A. and Poff, N. L. (1997). The Influence of Environmental Heterogeneity on Patterns and Processes in Streams. *Journal of the North American Benthological Society*, 16(1):169–173.

[156] Palmer, M. A., Swan, C. M., Nelson, K., Silver, P., and Alvestad, R. (2000). Streambed landscapes: Evidence that stream invertebrates respond to the type and spatial arrangement of patches. *Landscape Ecology*.

[157] Park, A., Jeong, H.-H., Lee, J., Kim, K. P., and Lee, C.-S. (2011). Effect of shear stress on the formation of bacterial biofilm in a microfluidic channel. *BioChip Journal*, 5(3):236–241.

[158] Parry, J. D. (2004). Protozoan Grazing of Freshwater Biofilms. pages 167–196.

[159] Passy, S. I. (2001). Spatial paradigms of lotic diatom distribution: a landscape ecology perspective. *Journal of Phycology*, 37(3):370–378.

[160] Passy, S. I. and Larson, C. A. (2011). Succession in Stream Biofilms is an Environmentally Driven Gradient of Stress Tolerance. *Microbial Ecology*, 62(2):414–424.

[161] Patil, J. S. and Anil, A. C. (2005). Quantification of diatoms in biofilms: Standardisation of methods. *Biofouling*.

[162] Persat, A., Nadell, C. D., Kim, M. K., Ingremeau, F., Siryaporn, A., Drescher, K., Wingreen, N. S., Bassler, B. L., Gitai, Z., and Stone, H. A. (2015). The Mechanical World of Bacteria. *Cell*, 161(5):988–997.

[163] Persson, F., Suarez, C., Hermansson, M., Plaza, E., Sultana, R., and Wilén, B.-M. (2017). Community structure of partial nitritation-anammox biofilms at decreasing substrate concentrations and low temperature. *Microbial Biotechnology*, 10(4):761–772.

[164] Petroff, A. P., Sim, M. S., Maslov, A., Krupenin, M., Rothman, D. H., and Bosak, T. (2010). Biophysical basis for the geometry of conical stromatolites. *Proceedings of the National Academy of Sciences of the United States of America*, 107(22):9956–61.

[165] Picard, C., Logette, S., Schrotter, J., Aimar, P., and Remigy, J. (2012). Mass transfer in a membrane aerated biofilm. *Water Research*, 46(15):4761–4769.

[166] Picioreanu, C., Van Loosdrecht, M. C., and Heijnen, J. J. (2001). Two-dimensional model of biofilm detachment caused by internal stress from liquid flow. *Biotechnology and Bioengineering*, 72(2):205–218.

[167] Picioreanu, C., van Loosdrecht, M. C. M., and Heijnen, J. J. (1998). Mathematical modeling of biofilm structure with a hybrid differential-discrete cellular automaton approach. *Biotechnology and Bioengineering*, 58(1):101–116.

[168] Picioreanu, C., van Loosdrecht, M. C. M., and Heijnen, J. J. (2000). A theoretical study on the effect of surface roughness on mass transport and transformation in biofilms. *Biotechnology and Bioengineering*, 68(4):355–369.

[169] Picioreanu, C., Vrouwenvelder, J., and van Loosdrecht, M. (2009). Three-dimensional modeling of biofouling and fluid dynamics in feed spacer channels of membrane devices. *Journal of Membrane Science*, 345(1-2):340–354.

[170] Pickett, S. T. and White, P. S. (2013). *The Ecology of Natural Disturbance and Patch Dynamics*.

[171] Poff, N. L., Voelz, N. J., Ward, J. V., and Lee, R. E. (1990). Algal Colonization under Four Experimentally-Controlled Current Regimes in High Mountain Stream. *Journal of the North American Benthological Society*, 9(4):303–318.

[172] Poff, N. L. R., Allan, J. D., Bain, M. B., Karr, J. R., Prestegaard, K. L., Richter, B. D., Sparks, R. E., and Stromberg, J. C. (1997). The natural flow regime: A paradigm for river conservation and restoration. *BioScience*.

[173] Pohlon, E., Marxsen, J., and Küsel, K. (2010). Pioneering bacterial and algal communities and potential extracellular enzyme activities of stream biofilms. *FEMS Microbiology Ecology*, 71(3):364–373.

[174] Pringle, C. M., Naiman, R. J., Bretschko, G., Karr, J. R., Oswood, M. W., Webster, J. R., Welcomme, R. L., and Winterbourn, M. J. (1988). Patch Dynamics in Lotic Systems: The Stream as a Mosaic. *Journal of the North American Benthological Society*, 7(4):503–524.

[175] Proctor, D. M. and Relman, D. A. (2017). The Landscape Ecology and Microbiota of the Human Nose, Mouth, and Throat. *Cell Host & Microbe*, 21(4):421–432.

[176] Purcell, E. M. (1977). Life at low Reynolds number. *American Journal of Physics*, 45(1):3–11.

[177] Qu, X., Ren, Z., Zhang, H., Zhang, M., Zhang, Y., Liu, X., and Peng, W. (2017). Influences of anthropogenic land use on microbial community structure and functional potentials of stream benthic biofilms. *Scientific Reports*, 7(1):15117.

[178] R Core Team (2020). R: A Language and Environment for Statistical Computing.

[179] Ramsing, N. B., Kuhl, M., and Jorgensen, B. B. (1993). Distribution of sulfate-reducing bacteria, O2, and H2S in photosynthetic biofilms determined by oligonucleotide probes and microelectrodes. *Applied and Environmental Microbiology*, 59(11):3840–3849.

[180] Raymond, P. A., Hartmann, J., Lauerwald, R., Sobek, S., McDonald, C., Hoover, M., Butman, D., Striegl, R., Mayorga, E., Humborg, C., Kortelainen, P., Dürr, H., Meybeck, M., Ciais, P., and Guth, P. (2013). Global carbon dioxide emissions from inland waters. *Nature*, 503(7476):355–359.

[181] Revsbech, N. P. (1989). Diffusion characteristics of microbial communities determined by use of oxygen microsensors. *Journal of Microbiological Methods*, 9(2):111–122.

[182] Revsbech, N. P. (2005). Analysis of microbial communities with electrochemical microsensors and microscale biosensors. *Methods in Enzymology*, 397(2003):147–166.

[183] Revsbech, N. P. and Jorgensen, B. B. (1983). Photosynthesis of benthic microflora measured with high spatial resolution by the oxygen microprofile method: Capabilities and limitations of the method.

[184] Revsbech, N. P., Jorgensen, B. B., and Blackburn, T. H. (1980). Oxygen in the Sea Bottom Measured with a Microelectrode. *Science*.

[185] Revsbech, N. P. and Ward, D. M. (1984). Microelectrode Studies of Interstitial Water Chemistry and Photosynthetic Activity in a Hot Spring Microbial Mat. *Applied and Environmental Microbiology*.

[186] Revsbech, N. P. N. and Jørgensen, B. B. B. (1986). Microelectrodes: their use in microbial ecology.

[187] Richey, J. E., Melack, J. M., Aufdenkampe, A. K., Ballester, V. M., and Hess, L. L. (2002). Outgassing from Amazonian rivers and wetlands as a large tropical source of atmospheric CO2. *Nature*, 416(6881):617–620.

[188] Rier, S. T., Kuehn, K. A., and Francoeur, S. N. (2007). Algal regulation of extracellular enzyme activity in stream microbial communities associated with inert substrata and detritus. *Journal of the North American Benthological Society*, 26(3):439–449.

[189] Rietkerk, M. (2004). Self-Organized Patchiness and Catastrophic Shifts in Ecosystems. *Science*, 305(5692):1926–1929.

[190] Riley, S., Eames, K., Isham, V., Mollison, D., and Trapman, P. (2015). Five challenges for spatial epidemic models. *Epidemics*, 10:68–71.

[191] Risse-Buhl, U., Trefzger, N., Seifert, A.-G., Schönborn, W., Gleixner, G., and Küsel, K. (2012). Tracking the autochthonous carbon transfer in stream biofilm food webs. *FEMS Microbiology Ecology*, 79(1):118–131.

[192] RisseBuhl, U., Anlanger, C., Chatzinotas, A., Noss, C., Lorke, A., and Weitere, M. (2020). Near streambed flow shapes microbial guilds within and across trophic levels in fluvial biofilms. *Limnology and Oceanography*, 65(10):2261–2277.

[193] Roberts, R. D., Damgaard, L. R., and Revsbech, N. P. (2011). Effect of water velocity and benthic diatom morphology on the water chemistry experiences by postlarval abalone. *Journal of Shellfish Research*, 8000(2007):3–6.

[194] Roche, K. R., Drummond, J. D., Boano, F., Packman, A. I., Battin, T. J., and Hunter, W. R. (2017). Benthic biofilm controls on fine particle dynamics in streams. *Water Resources Research*, 53(1):222–236.

[195] Roeselers, G., Van Loosdrecht, M. C., and Muyzer, G. (2007). Heterotrophic pioneers facilitate phototrophic biofilm development. *Microbial Ecology*, 54(3):578–585.

[196] Romaní, A. M., Borrego, C. M., Díaz-Villanueva, V., Freixa, A., Gich, F., and Ylla, I. (2014). Shifts in microbial community structure and function in light- and dark-grown biofilms driven by warming. *Environmental Microbiology*, 16(8):2550–2567.

[197] Romaní, A. M., Guasch, H., Muñoz, I., Ruana, J., Vilalta, E., Schwartz, T., Emtiazi, F., and Sabater, S. (2004). Biofilm Structure and Function and Possible Implications for Riverine DOC Dynamics. *Microbial Ecology*, 47(4).

[198] Rossy, T., Nadell, C. D., and Persat, A. (2019). Cellular advective-diffusion drives the emergence of bacterial surface colonization patterns and heterogeneity. *Nature Communications*, 10(1):2471.

[199] Saikia, S. K. (2011). Review on Periphyton as Mediator of Nutrient Transfer in Aquatic Ecosystems. *Ecologia Balkanica*.

[200] Scheidweiler, D., Peter, H., Pramateftaki, P., de Anna, P., and Battin, T. J. (2019). Unraveling the biophysical underpinnings to the success of multispecies biofilms in porous environments. *The ISME Journal*, 13(7):1700–1710.

[201] Schmitt-Wagner, D. and Brune, A. (1999). Hydrogen profiles and localization of methanogenic activities in the highly compartmentalized hindgut of soil- feeding higher termites (Cubitermes spp.). *Applied and Environmental Microbiology*.

[202] Scott, J. T., Back, J. A., Taylor, J. M., and King, R. S. (2008). Does nutrient enrichment decouple algal–bacterial production in periphyton? *Journal of the North American Benthological Society*, 27(2):332–344.

[203] Segata, N., Izard, J., Waldron, L., Gevers, D., Miropolsky, L., Garrett, W. S., and Huttenhower, C. (2011). Metagenomic biomarker discovery and explanation. *Genome Biology*, 12(6):R60.

[204] Sekar, R., Nair, K. V., Rao, V. N., and Venugopalan, V. P. (2002). Nutrient dynamics and successional changes in a lentic freshwater biofilm. *Freshwater Biology*.

[205] Sekar, R., Venugopalan, V. P., Nandakumar, K., Nair, K. V., and Rao, V. N. (2004). Early stages of biofilm succession in a lentic freshwater environment. In *Hydrobiologia*.

[206] Shen, Y., Monroy, G. L., Derlon, N., Janjaroen, D., Huang, C., Morgenroth, E., Boppart, S. A., Ashbolt, N. J., Liu, W.-T., and Nguyen, T. H. (2015). Role of Biofilm Roughness and Hydrodynamic Conditions in Legionella pneumophila Adhesion to and Detachment from Simulated Drinking Water Biofilms. *Environmental Science & Technology*, 49(7):4274–4282.

[207] Sherwood, A. R. (2016). Green Algae (Chlorophyta and Streptophyta) in Rivers. In *River Algae*, pages 35–63. Springer International Publishing, Cham, orlando ne edition.

[208] Simões, M., Pereira, M. O., Sillankorva, S., Azeredo, J., and Vieira, M. J. (2007). The effect of hydrodynamic conditions on the phenotype of Pseudomonas fluorescens biofilms. *Biofouling*, 23(4):249–258.

[209] Singer, G., Besemer, K., Hochedlinger, G., Chlup, A. K., and Battin, T. J. (2011). Monomeric carbohydrate uptake and structure-function coupling in stream biofilms. *Aquatic Microbial Ecology*.

[210] Singer, G., Besemer, K., Schmitt-Kopplin, P., Hödl, I., and Battin, T. J. (2010). Physical Heterogeneity Increases Biofilm Resource Use and Its Molecular Diversity in Stream Mesocosms. *PLoS ONE*, 5(4):e9988.

[211] Smith, D. J. and Underwood, G. J. C. (2001). The production of extracellular carbohydrates by estuarine benthic diatoms: the effects of growth phase and light and dark treatment. *Journal of Phycology*, 36(2):321–333.

[212] Statzner, B., Gore, J. A., and Resh, V. H. (1988). Hydraulic Stream Ecology: Observed Patterns and Potential Applications. *Journal of the North American Benthological Society*, 7(4):307–360.

[213] Stelzer, R. S. and Lamberti, G. A. (2001). Effects of N : P ratio and total nutrient concentration on stream periphyton community structure, biomass, and elemental composition. *Limnology and Oceanography*, 46(2):356–367.

[214] Stewart, P. S. (2003). Diffusion in Biofilms. *Journal of Bacteriology*, 185(5):1485–1491.

[215] Stewart, P. S. (2012). Mini-review: Convection around biofilms. *Biofouling*, 28(2):187–198.

[216] Stewart, P. S. and Franklin, M. J. (2008). Physiological heterogeneity in biofilms. *Nature Reviews Microbiology*, 6(3):199–210.

[217] Stoeck, T., Bass, D., Nebel, M., Christen, R., Jones, M. D. M., Breiner, H.-W., and Richards, T. A. (2010). Multiple marker parallel tag environmental DNA sequencing reveals a highly complex eukaryotic community in marine anoxic water. *Molecular Ecology*, 19:21–31.

[218] Stoodley, P., Cargo, R., Rupp, C. J., Wilson, S., and Klapper, I. (2002). Biofilm material properties as related to shear-induced deformation and detachment phenomena. *Journal of Industrial Microbiology and Biotechnology*, 29(6):361–367.

[219] Stoodley, P., DeBeer, D., and Lewandowski, Z. (1994). Liquid flow in biofilm systems. *Applied and Environmental Microbiology*.

[220] Stoodley, P., Dodds, I., De Beer, D., Scott, H. L., and Boyle, J. D. (2005). Flowing biofilms as a transport mechanism for biomass through porous media under laminar and turbulent conditions in a laboratory reactor system. *Biofouling*, 21(3-4):161–168.

[221] Stoodley, P., Hall-Stoodley, L., and Lappin-Scott, H. M. (2001a). Detachment, surface migration, and other dynamic behavior in bacterial biofilms revealed by digital time-lapse imaging. In *Methods in Enzymology*, volume 337, pages 306–319.

[222] Stoodley, P., Lewandowski, Z., Boyle, J. D., and Lappin-Scott, H. M. (1998a). Oscillation characteristics of biofilm streamers in turbulent flowing water as related to drag and pressure drop. *Biotechnology and Bioengineering*, 57(5):536–544.

[223] Stoodley, P., Lewandowski, Z., Boyle, J. D., and Lappin-Scott, H. M. (1998b). Oscillation characteristics of biofilm streamers in turbulent flowing water as related to drag and pressure drop. *Biotechnology and Bioengineering*, 57(5):536–544.

[224] Stoodley, P., Lewandowski, Z., Boyle, J. D., and Lappin-Scott, H. M. (1999a). Structural deformation of bacterial biofilms caused by short-term fluctuations in fluid shear: An in situ investigation of biofilm rheology. *Biotechnology and Bioengineering*, 65(1):83–92.

[225] Stoodley, P., Lewandowski, Z., Boyle, J. D., and Lappin-Scott, H. M. (1999b). The formation of migratory ripples in a mixed species bacterial biofilm growing in turbulent flow. *Environmental Microbiology*, 1(5):447–455.

[226] Stoodley, P., Wilson, S., Hall-Stoodley, L., Boyle, J. D., Lappin-Scott, H. M., and Costerton, J. W. (2001b). Growth and Detachment of Cell Clusters from Mature Mixed-Species Biofilms. *Applied and Environmental Microbiology*, 67(12):5608–5613.

[227] Stoodley, P., Yang, S., Lappin-Scott, H., and Lewandowski, Z. (1997). Relationship between mass transfer coefficient and liquid flow velocity in heterogenous biofilms using microelectrodes and confocal microscopy. *Biotechnology and Bioengineering*, 56(6):681–688.

[228] Strayer, D. L. and Dudgeon, D. (2010). Freshwater biodiversity conservation: Recent progress and future challenges. *Journal of the North American Benthological Society*.

[229] Sudarsan, R., Ghosh, S., Stockie, J. M., and Eberl, H. J. (2016). Simulating Biofilm Deformation and Detachment with the Immersed Boundary Method. *Communications in Computational Physics*, 19(3):682–732.

[230] Taherzadeh, D., Picioreanu, C., and Horn, H. (2012). Mass Transfer Enhancement in Moving Biofilm Structures. *Biophysical Journal*, 102(7):1483–1492.

[231] Taylor, B. W., Keep, C. F., Hall, R. O., Koch, B. J., Tronstad, L. M., Flecker, A. S., and Ulseth, A. J. (2007). Improving the fluorometric ammonium method: Matrix effects, background fluorescence, and standard additions. *Journal of the North American Benthological Society*.

[232] Tennekes, H. (1973). The Logarithmic Wind Profile. *Journal of the Atmospheric Sciences*.

[233] Thar, R. and Kühl, M. (2005). Complex pattern formation of marine gradient bacteria explained by a simple computer model. *FEMS Microbiology Letters*, 246(1):75–79.

[234] Thomen, P., Robert, J., Monmeyran, A., Bitbol, A. F., Douarche, C., and Henry, N. (2017). Bacterial biofilm under flow: First a physical struggle to stay, then a matter of breathing. *PLoS ONE*, 12(4):1–24.

[235] Tsai, Y. P. (2005). Impact of flow velocity on the dynamic behaviour of biofilm bacteria. *Biofouling*.

[236] Turner, M. G., editor (1987). *Landscape Heterogeneity and Disturbance*, volume 64 of *Ecological Studies*. Springer New York, New York, NY.

[237] Turner, M. G. (2010). Disturbance and landscape dynamics in a changing world. *Ecology*, 91(10):2833–2849.

[238] Van Loosdrecht, M. C., Heijnen, J. J., Eberl, H., Kreft, J., and Picioreanu, C. (2002). Mathematical modelling of biofilm structures. *Antonie van Leeuwenhoek, International Journal of General and Molecular Microbiology*.

[239] Vandecar, K. L., Lawrence, D., Wood, T., Oberbauer, S. F., Das, R., Tully, K., and Schwendenmann, L. (2009). Biotic and abiotic controls on diurnal fluctuations in labile soil phosphorus of a wet tropical forest. *Ecology*, 90(9):2547–2555.

[240] Vlamakis, H., Aguilar, C., Losick, R., and Kolter, R. (2008). Control of cell fate by the formation of an architecturally complex bacterial community. *Genes and Development*, 22(7):945–953.

[241] Wagner, K., Bengtsson, M. M., Findlay, R. H., Battin, T. J., and Ulseth, A. J. (2017). High light intensity mediates a shift from allochthonous to autochthonous carbon use in phototrophic stream biofilms. *Journal of Geophysical Research: Biogeosciences*, 122(7):1806–1820.

[242] Wagner, M. and Horn, H. (2017). Optical coherence tomography in biofilm research: A comprehensive review. *Biotechnology and Bioengineering*, 114(7):1386–1402.

[243] Wagner, M., Taherzadeh, D., Haisch, C., and Horn, H. (2010). Investigation of the mesoscale structure and volumetric features of biofilms using optical coherence tomography. *Biotechnology and Bioengineering*, 107(5):844–853.

[244] Wang, J., Yang, H., and Wang, F. (2014). Mixotrophic Cultivation of Microalgae for Biodiesel Production: Status and Prospects. *Applied Biochemistry and Biotechnology*, 172(7):3307–3329.

[245] Wang, L., Keatch, R., Zhao, Q., Wright, J. A., Bryant, C. E., Redmann, A. L., and Terentjev, E. M. (2018). Influence of Type I Fimbriae and Fluid Shear Stress on Bacterial Behavior and Multicellular Architecture of Early Escherichia coli Biofilms at Single-Cell Resolution. *Applied and Environmental Microbiology*, 84(6):1–13.

[246] Wäsche, S., Horn, H., and Hempel, D. C. (2002). Influence of growth conditions on biofilm development and mass transfer at the bulk/biofilm interface. *Water Research*, 36(19):4775–4784.

[247] Webster, J. R. (2000). Streams and ground waters. *Journal of the North American Benthological Society*.

[248] Weitere, M., Erken, M., Majdi, N., Arndt, H., Norf, H., Reinshagen, M., Traunspurger, W., Walterscheid, A., and Wey, J. K. (2018). The food web perspective on aquatic biofilms. *Ecological Monographs*, 88(4):543–559.

[249] Wieland, A. and KÃ¼hl, M. (2006). Regulation of photosynthesis and oxygen consumption in a hypersaline cyanobacterial mat (Camargue, France) by irradiance, temperature and salinity. *FEMS Microbiology Ecology*, 55(2):195–210.

[250] Wiens, J. A. (2002). Central Concepts and Issues of Landscape Ecology. In *Applying Landscape Ecology in Biological Conservation*, pages 3–21. Springer New York, New York, NY.

[251] Wilking, J. N., Zaburdaev, V., De Volder, M., Losick, R., Brenner, M. P., and Weitz, D. A. (2013). Liquid transport facilitated by channels in Bacillus subtilis biofilms. *Proceedings of the National Academy of Sciences of the United States of America*, 110(3):848–52.

[252] Winemiller, K. O., Flecker, A. S., and Hoeinghaus, D. J. (2010). Patch dynamics and environmental heterogeneity in lotic ecosystems. *Journal of the North American Benthological Society*, 29(1):84–99.

[253] Wu, Y. (2017). Periphytic Biofilm and Its Functions in Aquatic Nutrient Cycling. *Periphyton*, (1):137–153.

[254] Xavier, J. B., Martinez Garcia, E., and Foster, K. R. (2009). Social Evolution of Spatial Patterns in Bacterial Biofilms: When Conflict Drives Disorder. *The American Naturalist*, 174(1):1–12.

[255] Xavier, J. d. B., Picioreanu, C., and van Loosdrecht, M. C. (2005). A general description of detachment for multidimensional modelling of biofilms. *Biotechnology and Bioengineering*, 91(6):651–669.

[256] Xi, C., Marks, D., Schlachter, S., Luo, W., and Boppart, S. A. (2006). High-resolution three-dimensional imaging of biofilm development using optical coherence tomography. *Journal of Biomedical Optics*.

[257] Yan, J., Fei, C., Mao, S., Moreau, A., Wingreen, N. S., Košmrlj, A., Stone, H. A., and Bassler, B. L. (2019). Mechanical instability and interfacial energy drive biofilm morphogenesis. *eLife*, 8:1–28.

[258] Zeiringer, B., Seliger, C., Greimel, F., and Schmutz, S. (2018). *River Hydrology, Flow Alteration, and Environmental Flow*, pages 67–89. Springer International Publishing, Cham.

[259] Zexing, X., Chenling, Z., Qiang, Y., Xiekang, W., and Xufeng, Y. (2020). Hydrodynamics and bed morphological characteristics around a boulder in a gravel stream. *Water Supply*, 20(2):395–407.

[260] Zhang, T. C. and Bishop, P. L. (1994). Density, porosity, and pore structure of biofilms. *Water Research*, 28(11):2267–2277.

[261] Zippel, B., Rijstenbil, J., and Neu, T. R. (2007). A flow-lane incubator for studying freshwater and marine phototrophic biofilms. *Journal of Microbiological Methods*.

Glossary

aerobic an organism or a chemical or biochemical reaction that requires the presence of oxygen. 6

allochthonous originating outside the ecosystem under study, for instance the organic carbon that reaches the river with rain water percolating through the catchment soil. 20

anaerobic an organism or a chemical or biochemical reaction that requires the absence of oxygen. 7

autochthonous originating within the ecosystem under study, for instance the organic carbon fixed by benthic photosynthesis. 4

confocal laser scanning micrograph is an image acquired with a special microscope, in which a pinhole is used to exclude the light that comes from the parts of a sample that are not in focus. This allows for enhancement of the optical resolution and contrast. This technique is typically used for fluorescent samples or fluorescently labeled samples, that are illuminated with a so-called excitation beam, which has a specific wavelength depending on the target fluorophore. The light is absorbed by the sample and re-emitted with a different wavelength. The emitted light passes through the pinhole and a filter, which allows to select the desired wavelength, and finally it is photographed by a detector. 6

denitrification is a form of microbial respiration that uses nitrate as oxidative agent, while it produces reduced nitrogen species as a side product which usually escape the system as molecular nitrogen. This process is heavily inhibited by oxygen. 8

electron acceptor the oxidant that is required for respiration. This molecule accepts the electron falling into the electron transport chain, which is the last step in the biochemical process for the utilization of the energy within the chemical bonds of organic compounds (such as sugars). 6

extracellular enzymes enzymes that are secreted outside of the cell that produced them, where they carry out extracellular reactions. Many complex polymers, such as chitin, are first partially digested outside of cells into simpler components, and afterwards taken into the cells and assimilated. 4

heterotrophic adjective for organisms or processes that utilize organic materials as carbon source. Humans are heterotrophic, as they depend on the organic matter of animals and plants for their carbon requirements. 4

inertia in fluid dynamics, inertial forces are the forces acting on a fluid parcel that derive from the pressure of the surrounding flow. 10

interference is the combination of two or multiple waves. Depending on their relative wavelength and phase, the two waves can result in a greater or smaller waves, in the so called constructive or destructive interference. When two light beams with the same wavelength but a shift in phase meet, they produce a characteristic pattern of light and dark areas known as the interference fringe. 15

lotic ecosystems streams and rivers. 4

no-slip boundary in fluid dynamics, this is a boundary (typically between a solid and a fluid) in which the velocity of the fluid becomes zero at the interface. In other words, the fluid does not slip on the solid surface. 11

photoautotrophic organisms or processes that produce organic carbon starting from inorganic sources, such as CO_2, using light as an energy source. Plants are photoautotrophic, as they can fix the atmospheric CO_2 into energy rich sugars. 4

photosynthesis the biochemical process that stores the energy of light into energy-rich, reduced organic compounds, and produces oxygen as a side product. 4

respiration the biochemical process that uses organic compounds and an oxidant (oxygen been a very common one) to release energy, while producing CO_2 as a side product. 6

solute a dissolved chemical species (typically in water). 1

viscous forces the set of forces acting on a fluid parcel that derive from the friction with the surrounding fluid. 10

EPFL ENAC IIE SBER
GR B0 422 (Bâtiment GR) Station 2
Lausanne, Switzerland 1015
☎ +41 21 69 33804
✉ anna.depetris@epfl.ch

Anna Depetris

Education

Jul2017– present **PhD in Environmental Engineering**,
École Polytechnique Fédérale de Lausanne (EPFL) – Lausanne, Switzerland.

Sep2014– Sep2016 **Erasmus Mundus Master Programme in Evolutionary Biology - MEME**,
University of Groningen (RUG) – Groningen, The Netherlands
Ludwig Maximillian University (LMU) – Munich, Germany.

Sep2010– Sep2013 **Bachelor's degree in Biomolecular Sciences**,
University of Trento (UNITN)– Trento, Italy,
Grade: 110/110 with honors (Cumulative GPA: 4).

Jan– May2013 **International Semester in Life Sciences**,
Turku University of Applied Sciences (TUAS) – Turku, Finland.

Experience and Courses

Jul2017– present **Structural patterns in stream biofilms, EPFL**,
Supervisor: Tom Battin, PhD,
Lausanne, Switzerland.
My PhD project aims at the investigation of the effect of hydraulics on the functions of freshwater benthic biofilms. We namely investigate structural patterns of the biomass distribution, as well as spatial arrangement of biodiversity and metabolic activities.

May2020 **Scientific Programming with Python**,
University of Zürich,
online.
This course teaches a selection of important Python programming techniques and incorporates theoretical lectures followed by practical exercises where the discussed techniques can be applied and tried out.

Jul–Aug2019 **Microbial Diversity Course (MD)**,
Marine Biological Laboratory (MBL), University of Chicago,
Woods Hole, Massachusetts, USA.
This course is an intensive six-and-a-half-week research and training experience for graduate or postdoctoral students, as well as established investigators, who want to become competent in microbiological techniques for working with a broad range of microbes, and in approaches for recognizing the metabolic, phylogenetic, and genomic diversity of cultivated and as yet uncultivated bacteria.

Oct2018 **Advanced Biofilm Course (ABC)**,
Helmholtz Centre for Environmental Research GmbH – UFZ,
Magdeburg, Germany.
The aim of the course is to explore given biofilms with different methods to gain information about their structure and function. The course aims to teach major tools used in biofilm research: biofilm imaging, microsensor techniques and mathematical modelling.

Jun2018 **Microsensor analysis in the environmental sciences**,
University of Copenhagen and Aarhus University,
Rønbjerg field laboratory, Denmark.
This course introduce me to state-of-art microenvironmental analysis and to the application of electrochemical and optical microsensor techniques in the environmental sciences.

Apr–Jun2015, Apr–Oct2016 **Phenotypic heterogeneity in a siderophore-producing *Pseudomonas putida* population, LMU**,
Supervisor: Heinrich Jung, PhD,
Munich, GERMANY.
My Master's thesis project aimed at the characterization of the heterogeneity in the production and storage of siderophores in *P. putida*. I generated strains carrying a genomically integrated fluorescent reporters and analysed their expression by single-cell based techniques.

Mar–Apr2017, Mar–Apr2016 **Tutor for the course in Mathematical Modelling in Ecology and Evolution, LMU**,
Lecturer: Ferdinand Pfab,
Munich, GERMANY.

Apr–Aug2014 **Dynamics of extracellular matrix producers and non-producers in *Bacillus subtilis* biofilms, HMS**,
Supervisors: Roberto Kolter PhD, Franjo Weissing PhD,
Harvard Medical School, Boston, USA.
For my first research project in the MEME program, I investigated the cooperative dynamics of extracellular matrix production in *B. subtilis* biofilms.

Apr–Aug2014 **Project for the Conservation of the Burrowing Parrot - Plant Ecophysiology Lab, ULS**,
Supervisors: Renzo Vargas Rodriguez PhD, Franscisco Squeo PhD,
La Serena, CHILE.
Laboratory technician.

Jan–Mar2014 **Coral Reef Ecology - Coral Biogeochemistry Lab, HKU**,
Supervisors: David M. Baker PhD, Nicolas Duprey PhD,
Hong Kong, CHINA.
Laboratory technician.

Feb–May2013 **SUSBIO project: Metagenomics of a bacterial-archeal community – Molecular Diagnostics Laboratory (MDL), TUAS**,
Supervisor: Annika Brandt PhD,
Turku, FINLAND.
Lab technician.

May–Nov2012 **iGEM (international Genetically Engineered Machine competition) - 2012 Trento iGEM team, UNITN**,
Supervisors: Cristina Del Bianco PhD, Sheref Mansy PhD, Olivier Jousson PhD,
Trento, ITALY.
For my Bachelor's thesis I took part in the international synthetic biology competition as part of the 2012 Trento iGEM team.

Laboratory techniques

Optical coherence tomography of biofilms

Oxygen microprofiling

Transmitted light and fluorescence microscopy

Time-lapse fluorescence microscopy of dividing micro-colonies

Confocal laser scanning microscopy

Flow cytometry of microbial cells
Culture and transformation of bacteria
PCR optimization, primers design, gel electrophoresis, cloning
Isolation and quantification of nucleic acids

Software and programming

Basics in Python programming and images analysis
R (statistical analysis)
Fiji-ImageJ (microscopy data analysis)
Basics in Wolfram Mathematica and MatLab
LaTex

Languages

Italian	mother tongue
English	TOEFL IBT: 111/120, obtained on 9^{th} November 2013
Spanish	Fluent
French	Intermediate